6-28-2012 12:00 AM

Phase Field Crystal Approach to the Solidification of Ferromagnetic Materials

Niloufar Faghihi, *The University of Western Ontario*

Supervisor: Mikko Karttunen, *The University of Western Ontario*

A thesis submitted in partial fulfillment of the requirements for the Doctor of Philosophy degree in Applied Mathematics

PHASE FIELD CRYSTAL APPROACH TO THE SOLIDIFICATION OF FERROMAGNETIC MATERIALS

(Thesis format: Monograph)

by

Niloufar Faghihi

Graduate Program in Applied Mathematics

A thesis submitted in partial fulfillment
of the requirements for the degree of
Doctor of Philosophy

The School of Graduate and Postdoctoral Studies
The University of Western Ontario
London, Ontario, Canada

THE UNIVERSITY OF WESTERN ONTARIO
School of Graduate and Postdoctoral Studies

CERTIFICATE OF EXAMINATION

Supervisor:

.....
Professor Mikko Karttunen

Co-Supervisor:

.....
Professor Nikolas Provatas

Supervisory Committee:

.....
Professor Robert M. Corless

Examiners:

.....
Professor Alex Buchel

.....
Professor John R. de Bruyn

.....
Professor Zhi-Feng Huang

.....
Professor Geoff Wild

The thesis by

Niloufar Faghihi

entitled:

Phase Field Crystal Approach to the Solidification of Ferromagnetic Materials

is accepted in partial fulfillment of the
requirements for the degree of
Doctor of Philosophy

.....
Date

.....
Chair of the Thesis Examination Board

Acknowlegements

This work was made possible by many friends and collaborators. First and foremost, I sincerely thank my supervisor, Professor Mikko Karttunen, for his continuous support, encouragement and patience.

I would also like to express my gratitude towards my co-supervisor, Professor Nikolas Provatas, who provided me with the opportunity to visit his research group at McMaster University where I learned a lot from the several discussions that I had with him and his research group. I acknowledge his valuable advice and guidance which enabled me to solve this problem.

I am indebted to Professor Ken Elder whose truly scientific intuition leaded me to higher levels of understanding of physical phenomena. During my visits to his research group at Oakland University, I had the opportunity to discuss my project with him which enabled me to overcome the challenges of the problem. Working with him was very inspiring and enriched my growth as a student and a researcher, from which I will benefit for the rest of my academic work.

I was very fortunate to start in the soft matter group in UWO when Cristiano Dias was a postdoc there. His questions regarding the project helped me to clarify the ambiguities and to challenge the deeper aspects of my project. His curious character and wisdom was inspiring and provided a lively and active atmosphere in the group. I would like to thank him for his continuous help and support.

I would also like to thank Markus Miettinen for his encouragement, help and guidance as a senior graduate student of the group. It was fun to chat with him and to share the same office during his time at UWO.

I am grateful to Nana Ofori-Opoku for always being there for discussions and for being so kind to edit my thesis. Also I would like to thank Matthew Hoopes and Jari Jalkanen for spending time to edit my thesis and for their useful comments.

It is a pleasure to recall my friends Susanna, Jirasak, John, Shadi and Sarah and the great time we had together gathering, biking and chatting during my time in London, ON.

Finally, I would like to express my deepest gratitude towards my parents, Pari and Mohsen, for their unconditional support and love, and dedicate this work to them.

Abstract

The dependence of the magnetic hardness on the microstructure of magnetic solids is investigated, using a field theoretical approach, called the Magnetic Phase Field Crystal model. We constructed the free energy by extending the Phase Field Crystal (PFC) formalism and including terms to incorporate the ferromagnetic phase transition and the anisotropic magneto-elastic effects, *i.e.,* the magnetostriction effect.

Using this model we performed both analytical calculations and numerical simulations to study the coupling between the magnetic and elastic properties in ferromagnetic solids. By analytically minimizing the free energy, we calculated the equilibrium phases of the system to be liquid, non-magnetic solid and magnetic solid. We also studied the anisotropic manegostriction effect using the infinitesimal strain theory. Finally we calculated the hysteresis loop of a single crystal by minimizing the material's magnetic free energy. These analytical calculations gave us an insight into the properties of the model.

We then used numerical simulations to solve the dynamical equations of motion and to track the evolution of the density and magnetization fields. Using simulations we confirmed the analytically calculated phase diagram and the hysteresis loop of a single crystal. We also performed simulations to address the effect of the grain size on the magnetic hardness. In these simulations we computed the coercivity of the system for different grain sizes and showed that the results are in agreement with the experimental data on magnetic nanocrystalline alloys. This is a quite interesting result which enables us to comprehend the mechanism of the formation and growth of the domains in the presence of the grains and the mutual effects of the elastic and magnetic properties. Finally we studied the effect of the coercivity on the grain boundary angle and showed that the coercivity decreases with increasing the grain boundary angle. The importance of such studies lies in today's need for more efficient electronic devices such as transformers and magnetic recording devices.

The PFC formalism used in this research, although being a coarse-grained free energy, can resolve the atomic structure and symmetries of the solid and therefore many natural properties of the solid that are associated with the symmetry and periodicity, spontaneously emerge in this formalism. This includes elastic and plastic deformations, differently oriented grains and grain boundaries in polycrystals and formation and diffusion of the defects. These features makes this method ideal for the subject of this research.

Keywords: ferromagnetic materials, phase field crystal method, grain, hysteresis curve, coercivity

Contents

List of Figures

List of Appendices

Chapter 1

Introduction

In this work, I have been working towards understanding the inter-relation between morphological structure and magnetic properties of ferromagnetic solids, specifically the dependence of the magnetic hardness (coercivity) on the grain size in ferromagnetic solids. Analytical considerations and finite difference simulations were used to analyze the anisotropic magnetic effects in crystalline solids and to investigate the microstructural dependence of the coercivity in ferromagnetic materials.

One of the important quantities that characterize the hysteresis curve of a ferromagnetic material is the coercivity. It is the reversed field required to reduce the magnetization of a saturated magnetic sample to zero. Ferromagnetic materials are classified to hard and soft. Soft magnetic materials have a small magnetic hardness (low coercivity) while hard magnetic materials have a high coercivity [60].

Magnetic materials are the essential components in many devices and are at the root of progress in electrical engineering, electronics and many areas of material science. Soft magnetic materials are used in devices that need a quick change of magnetization with the minimum energy loss per cycle such as transformers and play a key role in power generation and conversion devices [22]. Increasing the capability of these devices which results in increased production of energy and reduction of losses can be accomplished by improving soft magnetic properties.

Magnetic materials also play an important role in magnetic data storage devices. In recent years focus has been moved from microcrystalline to nanocrystalline materials and the need for producing materials with higher areal density[1] and smaller sizes have been significantly increased.

A typical magnetic recording data system, such as a computer hard disk, consists of three main components: 1) Storage medium which is composed of a magnetic layer and several other layers, each of which has its own specific role in the production of high performance magnetic recording media [46]. The data is stored in the form of small magnetized areas in the magnetic layer [60]. 2) The write head which consists of a wire coil wound around a magnetic material which generates a magnetic field by electromagnetic induction, when current passes through the coil. This magnetic field is used to write data in the magnetic layer by magnetizing the data bits. 3) The read head which reads the the recorded magnetized areas, either by a reverse

[1]The areal density is the number of bits per unit area of the disk surface [60].

process of magnetic induction or by magnetoresistance[2]. A photograph of the inside of a hard disk drive is shown in Fig.1.1.

Figure 1.1: The inside of a hard disk drive. It is a device for storing and retrieving digital information. It consists of one or more rapidly rotating discs (storage medium) which is coated with the magnetic layer, read and write heads. This picture is reproduces from [20] under the terms of GNU Free Documentation License.

Designing an efficient recording device is challenging. By using higher coercivity materials in the magnetic layer we can stabilize smaller bits and increase the areal density. To enable writing in higher coercivity media, we need higher magnetization in the write head and to allow detecting field lines from smaller bits we need lower read head to disk spacing and more sensitive read heads. It is important to develop processing methods to produce alloys that are more efficient to be used in magnetic recording devices.

We learn from material science and engineering is that the macroscopic properties of materials depend on their microstructures which in turn depend on the method the materials was produced [46]. The magnetic anisotropy produces a barrier to magnetize and demagnetize the material. For soft magnetic materials, a small magnetic anisotropy is favourable to minimize the hysteresis losses and maximize the permeability. Structure-dependent magnetic properties are determined by defects concentration, atomic order, impurities, grain size, thermal history, etc. In materials consisting of multi-domains, the domain wall energy spatially varies as a result of local variations in chemical variation, defects, etc. This is the key concept that makes

[2]The magnetoresistance is the change in the resistance of a material when a magnetic field is applied.

the control of soft magnetic properties possible by controlling the microstructures.

The relation between the the magnetic hardness (coercivity H_c) and the grain size D has been examined through several experiments [46]. It has been observed that H_c is inversely proportional to the grain size for the materials with grain sizes above $D \sim 150nm$. Here the grain boundary acts as an obstruction to domain wall motion and thus materials with smaller grain size are magnetically harder. Progress in understanding the magnetic properties has led to the discovery of nanocrystalline Fe-based alloys that exhibit prominent soft magnetic properties [27], [28]. Experimental work on nanocrystalline materials implied that for very small grain sizes $D < 50nm$, H_c steeply decreases with decreasing grain size following D^6 law in three dimensions. This is explained using the fact that for such grain sizes the domain wall's thickness increases the grain size and several magnetic grains lie within one magnetic domain which causes averaging over the anisotropies of the grains with different orientations. This is the main idea of the Random Anisotropy Model [28] and suggests that nanocrystalline and amorphous alloys are potentially ideal as soft magnetic materials. By processing the nanocrystalline grains to be exchange-coupled, we can produce ideal soft magnetic materials [29].

In this dissertation we constructed a novel free energy functional (Magnetic PFC Model) to incorporate the elastic and magnetic properties of ferromagnetic crystalline phases. The free energy is an extension of the traditional Phase Field Crystal (PFC) free energy with additional terms to include the ferromagnetic phase transition and anisotropy effects in ferromagnetic solids.

The advantage of a free energy based on the PFC model to study the microstructure evolution in ferromagnetic solids is its atomistic spatial resolution. The PFC free energy, is minimized by periodic structures (in 2D by liquid, stripe and hexagonal phases), and naturally incorporates the elastic properties of a material [16]. Furthermore the amplitude expansion method allows us to derive the Magnetic PFC free energy in terms of the strain tensor elements. This gives us a clear interpretation of the free energy terms that incorporate the magneto-elastic effects.

Using other field theoretical models such as the Phase Field method to study dependence of the magnetic properties on the microstructure is tedious due to the fact that the phase field free energy functional does not resolve the atomistic structure of the solid and therefore one needs to include the effects that emerge from the periodic atomistic structure by adding several terms to cover all of the effects [38].

Chapters 2 to 6 are the review chapters and provide the basis necessary to understand the original work done in this study, *i.e.,* the Magnetic PFC model (Chapter 7). The main results of the calculations are presented in Chapters 8, 9. A detailed description on how to derive the model and the phase diagram, as well as an explanation of the numerical methods are given in the Appendices A to C.

It should be mentioned that the Magnetic PFC model is a novel model, with terms that couple the elastic effects to the magnetic effects. Coupling terms that give rise to elastic effects and the terms that give rise to the magnetic effects is the key here, to have a correct description of the inter-relation between the magnetic and the elastic effects. A notable time in this research has been devoted to figure out the correct form of the Magnetic PFC free energy and to include appropriate terms to model ferromagnetic solids, correctly.

This thesis is organized as follows. In Chapter 2, I provided an overview of magnetic materials, definitions of the basic magnetic quantities, the origin of ferromagnetism and the domain

theory. This section contains different energy terms that are associated with the formation of the domains and anisotropy effects in magnetic solids.

In Chapter 3, the traditional approach to study the solidification process, namely the Stefan problem is explained. The procedure to calculate the phase diagram of a binary mixture, using the common tangent construction is covered. This method is used in Chapter 7 to calculate the equilibrium states of the Magnetic PFC method. Then the kinetics of the phase transition and the two different mechanisms of phase transition (spinodal decomposition and nucleation) are explaind. This provides the background to understand the origins of the differently oriented grains and to discuss the experimental works done to discover the dependence f the magnetic hardness on the grain size.

Then I consider the basic concepts to understand the Phase Field Crystal method. Starting with the necessary background, the Langadu-Ginzburg theory of phase transition the concept of coarse-graining is explained in Chapter 4. Then in Chapter 5, I explain the dissipative dynamics to study non-equilibrium interface phenomena and coarsening processes. Eventually in Chapter 6, I discuss the PFC formalism, the derivation of its free energy functional, calculation of its phase diagram and the amplitude expansion method.

In Chapter 7, the Magnetic PFC free energy is presented. The connection between the phenomenological parameters of the free energy and the measurable physical quantities is explained and derivation of the free energy of the magnetic field inside the ferromagnetic material is provided. The dynamical equations of motion, used to do simulations are also considered in this chapter.

Chapter 8 is devoted to understand the properties of the model using analytical calculations. These calculations consist of calculation of the free energy in terms of the amplitudes, η_j, of the density field in the Fourier space. Then we incorporated elastic deformations by assuming that the amplitudes vary over long length scales and evaluated the free energy in terms of the strain tensor elements. Writing the free energy in this form is instructive since it indicates the physical essence of the different terms of the free energy more clearly. Using this form of the free energy we calculate the equilibrium states of the model by minimizing the free energy and evaluating the phase diagram. The anisotropic effect in magneto-elastic coupling, *i.e.,* the magnetostriction effect is examined by considering the deformation of a ferromagnetic sample under the influence of an external magnetic field. In the last section of Chapter 8, I discussed the analytical procedure we used to calculate the hysteresis loop of a singe crystal and the coercivity.

In Chapter 9, the results of the dissipative dynamics simulations and the numerical calculation of the coercivity, using the Magnetic PFC free energy is presented. We used finite difference simulations to confirm the phase diagram that was calculated in Chapter 7 and to confirm the coercivity that we calculated analytically. Simulations were also used to examine the experimental results by Herzer, *i.e.* the coercivity-grain size relation. Finally we checked the dependence of the coercivity on the grain boundary angle.

In Chapter 10, I concluded the the results and presented a brief discussion of the limitations and applications of our formalism and the possible future projects.

Chapter 2

Magnetic Materials

If an external magnetic field **H** is applied to a material, the magnetic field inside the material is different from **H**. This is due to the interaction of the atomic currents with the external magnetic field. In the classical picture atomic currents result from electron motion around the atomic nucleus [33]. The magnetic field inside the material is called the *magnetic induction*, **B**. The relationship between **B** (measured in *Teslas* in SI units and *Gauss* units in the cgs system) and **H** (measured in *Amperes per Meter* in SI system and *Oersted* in cgs) is a property of the material.

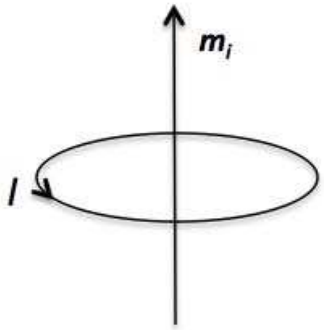

Figure 2.1: Magnetic dipole moment $\mathbf{m}_i$ resulting from atomic current, I.

Each atomic current is a tiny closed circuit and therefore, a magnetic dipole $\mathbf{m}_i$ could be assigned to each atom i, as schematically shown in Fig. 2.1. The magnetic properties of matter are characterized by the macroscopic quantity, called *magnetization*, as

$$\mathbf{M} = \lim_{\Delta v \to 0} \frac{1}{\Delta v} \sum_i \mathbf{m}_i \tag{2.1}$$

where Δv is the volume element, in which the magnetic dipole moments are vectorially summed up. It depends on both the individual magnetic moments of the atoms and how they interact with each other and is measured in *Amperes per Meter* in SI and emu/cm^3 in cgs. It should

be mentioned that for the purposes of this work we do not specifically use any microscopic description of the magnetic moments. We only use the macroscopic magnetization defined in Eq. 2.1.

The equation relating the applied magnetic field **H** and the magnetic induction, **B** is (in SI unites)

$$\mathbf{B} = \mu_0(\mathbf{H} + \mathbf{M}) \tag{2.2}$$

where μ_0 is the permeability of free space and is a measure of the amount of resistance encountered when forming a magnetic field in vacuum. It has an exact (defined) value of $\mu_0 = 4\pi\times10^{-7}$ *Newtons per Ampere squared* in the SI systems.

Depending on the configuration of the electrons in the outermost shell of the atomic orbitals, the reaction of the material to the external magnetic field, can change. If the valence shell of the atom is filled, then the atom does not have any net magnetization since the magnetic fields from two paired electrons cancel each other and the net magnetization of the atom sums up to zero and *diamagnetic* effect is observed in such materials. If an electron in the valence shell does not pair up with another electron, then each atom will have a net magnetization and this changes the magnetic properties of the material and how it reacts to an external magnetic field. In such materials, either *paramagnetism* or *ferromagnetism* is observed depending on the strength of the interaction among neighbouring magnetic moments.

2.1 Susceptibility, Permeability and Hysteresis

Knowing **M** is not enough to understand the magnetic properties of the material [60]. It is essential to have a relationship between **B** and **H** or, equivalently between **M** and one of the magnetic field vectors. This relationship depends on the nature of the magnetic material and is usually obtained from experiments. The ratio of the magnetization to the applied magnetic field is called the susceptibility, and it is not necessarily a scalar quantity. This means that the the magnetization produced in the material by applying the magnetic field, **H**, might not be in the direction of **H**. In general the susceptibility, χ_{ij}, is defined as a second rank tensor

$$M_i = \sum_j \chi_{ij} H_j \tag{2.3}$$

It shows how responsive a material is to an applied magnetic field. The ratio of the magnetic induction to the applied magnetic field is called permeability. To describe permeability in anisotropic media, a permeability tensor, μ_{ij}, is needed, which is defined as

$$B_i = \sum_j \mu_{ij} H_j, \tag{2.4}$$

It indicates how permeable (penetrable) the material is to the magnetic field. A material which has higher amount of magnetic flux in it, has a higher permeability.

The graphs of **M** or **B** versus **H** are characteristic of the type of material. For diamagnetic and paramagnetic materials, the **M**-**H** curves are linear. For diamagnets, the slope of this curve

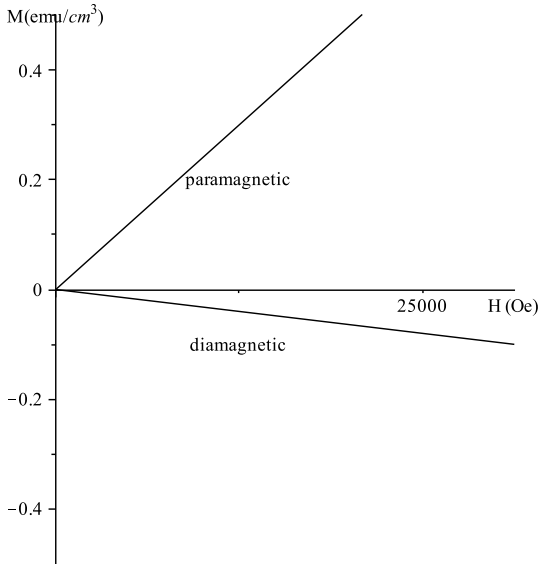

Figure 2.2: Magnetization curve for typical paramagnetic and diamagnetic materials.

is negative and permeability is slightly less than one. For paramagnetic material the slope is positive and permeability is slightly greater than unity, as illustrated in Fig. 2.2.

Figure 2.3 shows the magnetization curve for ferromagnets. First of all, in ferromagnets permeability and susceptibility are much larger than dia- and paramagnets. A much larger magnetization is obtained by applying a much smaller external field. This is apparent from the rough values [60] denoted on the M and H axes in Figs. 2.2 and 2.3. Second, above a certain applied field, the magnetization converges to a constant value, the saturation magnetization. Finally, decreasing the field to zero does not reduce the magnetization to zero. It takes a magnetic field in the opposite direction to remove the magnetization. This phenomenon is called *hysteresis*.

In fact, ferromagnets continue to show interesting behaviour when the field H is reduced to zero and then reversed in direction. The graph of **B** or **M** versus **H** which shows the behaviour of ferromagnets in such a process is called a *hysteresis loop*. Considering the process shown in figure 2.4, the material starts in an unmagnetized state, at the origin. The magnetic induction follows the curve from 0 to $\mathbf{B}_s$, as the field is increased in the positive direction. **B** continues to increase even after the magnetization saturates, because $\mathbf{B} = \mu_0(\mathbf{H} + \mathbf{M})$. When **H** is reduced to zero after saturation, the induction decreases from $\mathbf{B}_s$ to $\mathbf{B}_r$.

The magnetization left behind after an external magnetic field is removed, is called *remanence*. The reversed field required to reduce the induction to zero is called *coercivity*, $\mathbf{H}_c$. When the reversed **H** is increased further, saturation is achieved in the reverse direction. Both tips represent magnetic saturation and there is inversion symmetry about the origin.

The coercivity is an important parameter which determines the magnetic properties of the material and its applications. If the coercivity is small, then it takes a small magnetic field to magnetize and demagnetize the magnetic material. This results in less energy loss when the direction of an *AC* magnetic field is inverted in an electronic devices such as transformers

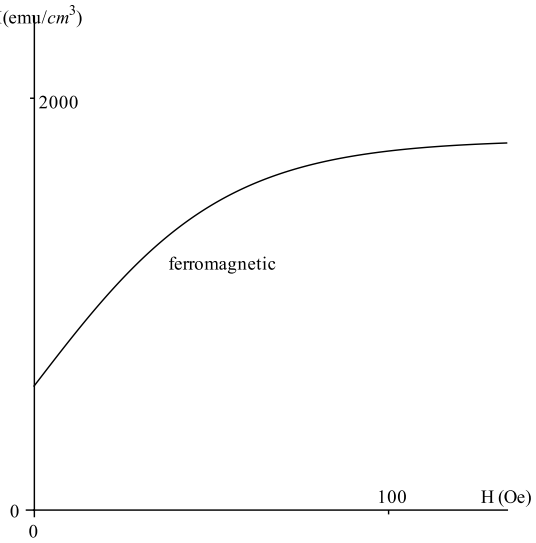

Figure 2.3: Magnetization curve for typical ferromagnetic materials.

and inductors that need to operate at high *AC* frequencies. On the other hand if the coercivity is high, then a large magnetic field is required to demagnetize the magnetic material. Such materials are ideal as permanent magnets.

2.2 Diamagnetism

Diamagnetism is the result of Lenz's law in atomic scale[1]. When a magnetic field is applied, the atomic currents are modified in such a way that they tend to weaken the effect of this field, so the induced magnetic moments are directed opposite to the applied field. That is the reason why the slope of the curve for diamagnets in Fig. 2.2 is negative.

Diamagnetic effect occurs in all atoms even those in which all electron shells are filled and so have a zero net magnetic moment. In fact, it is such a weak phenomenon that only those atoms that have no net magnetic moment are classified as diamagnetic. In other materials, the net magnetic moment introduces much stronger interactions and the diamagnetic effect is negligible comparing to those interactions.

If a container of a diamagnetic material, such as bismuth, is suspended in a non-uniform magnetic field, it will swing away from the high field region, to decrease the induced magnetization energy inside it.

[1]Lenz's law states that the induced current is in such a direction as to oppose the change of flux through the circuit [33].

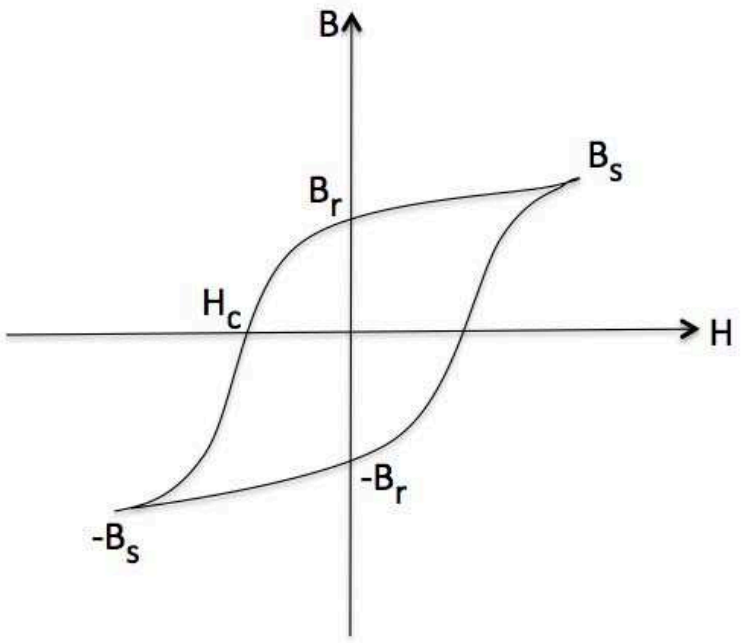

Figure 2.4: Hysteresis loop for a ferromagnetic material

2.3 Paramagnetism

Paramagnetic effect can be observed in materials that have a net magnetic moment. First, the orbital motion of each electron in an atom or molecule can be described in terms of a magnetic moment. Second, it is known that the electron has an intrinsic property called *s*pin, and an intrinsic magnetic moment associated with this spinning charge. Each molecule then, has a magnetic moment which is the vector sum of orbital and spin moments from various electrons in the molecule.

Langevin theory of paramagnetism explains the paramagnetic effect and the temperature dependence of susceptibility [60]. In paramagnetic materials, magnetic moments are only weakly coupled to each other and so thermal energy causes random alignment of the magnetic moments. When an external magnetic field is applied, the moments start to align with the field. Suppose that a magnetic moment has an angle θ with the applied field $\mathbf{H}$. In equilibrium at temperature T, the probability that the magnetic moment has an energy E, is given by the Boltzmann distribution:

$$e^{-E/k_BT} = e^{\mathbf{m}\cdot\mathbf{H}/k_BT} = e^{mH\cos\theta/k_BT} \tag{2.5}$$

Here, k_B is the Boltzmann's constant and m and H are the magnitudes of the respective fields. The number of moments having an angle between θ and $\theta+d\theta$ with respect to $\mathbf{H}$ is proportional to the fractional surface area of a surrounding sphere, $dA = 2\pi r^2 \sin\theta d\theta$, depicted in Fig. 2.5.

The probability of a moment to make an angle between θ and $\theta + d\theta$ would be:

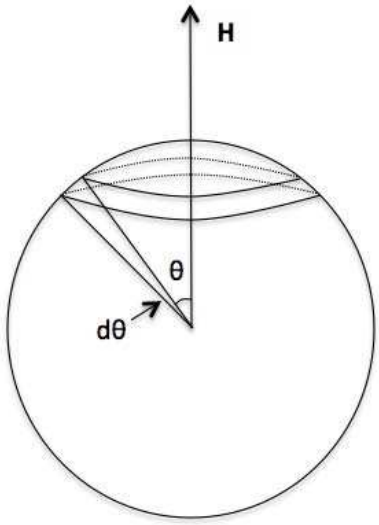

Figure 2.5: Fractional area, dA, confined by the angle $d\theta$

$$p(\theta) = \frac{e^{mH\cos\theta/k_BT}\sin\theta d\theta}{\int_0^\pi e^{mH\cos\theta/k_BT}\sin\theta d\theta} \tag{2.6}$$

where the factors of $2\pi r^2$ cancel out. Each moment contributes an amount $\mathbf{m}\cos\theta$ to the total magnetization parallel to the magnetic field $\mathbf{M}$

$$\begin{aligned}\mathbf{M} &= N\mathbf{m} < \cos\theta >= N\mathbf{m}\int_0^\pi \cos\theta p(\theta)d\theta \\ &= N\mathbf{m}\frac{\int_0^\pi e^{mH\cos\theta/k_BT}\cos\theta\sin\theta d\theta}{\int_0^\pi e^{mH\cos\theta/k_BT}\sin\theta d\theta}\end{aligned} \tag{2.7}$$

Evaluating the integrals gives:

$$\mathbf{M} = N\mathbf{m}\Big[\coth\Big(\frac{m\mu_0 H}{k_BT}\Big) - \frac{k_BT}{m\mu_0 H}\Big] = N\mathbf{m}L(\alpha) \tag{2.8}$$

where $\alpha = mH/k_BT$ and $L(\alpha) = \coth(\alpha) - 1/\alpha$ is called the Langevin function. $L(\alpha)$ is plotted in Fig. 2.6. As α increases, $L(\alpha)$ approaches its maximum, and $\mathbf{M}$ approaches $N\mathbf{m}$. Increasing α corresponds to increasing $\mathbf{H}$ or decreasing the temperature which results in alignment of the spins with the applied magnetic field.

To find the susceptibility, we first Taylor expand the Langevin function around zero [60]:

$$L(\alpha) = \frac{\alpha}{3} - \frac{\alpha^3}{45} + ... \tag{2.9}$$

Then assuming α is small (which is the case at all practical fields and temperatures), and looking only at the first term,

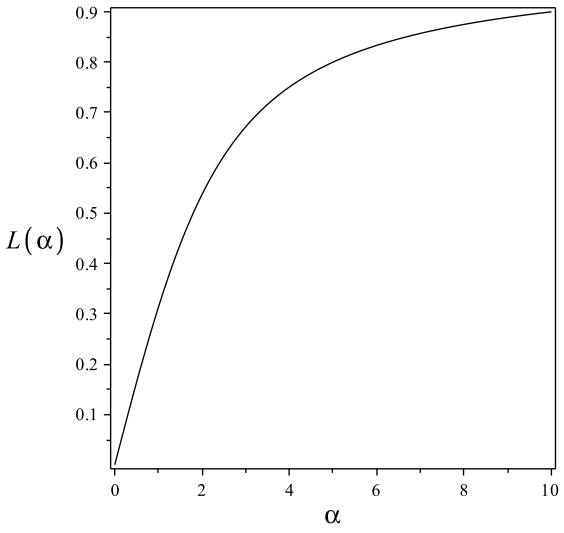

Figure 2.6: Langevin function, $L(\alpha)$, used to describe the dependence of the susceptibility on temperature in paramagnetic materials

$$\mathbf{M} = \frac{N\mathbf{m}\alpha}{3} = \frac{N\mu_0 m^2}{3k_B}\frac{\mathbf{H}}{T} \tag{2.10}$$

This gives the susceptibility:

$$\chi = \frac{\mathbf{M}}{\mathbf{H}} = \frac{N\mu_0 m^2}{3k_B T} = \frac{C}{T} \tag{2.11}$$

where $C = Nm^2/3k_B$. This is *Curie's law*, which states that the susceptibility of a paramagnet is inversely proportional to the temperature.

2.4 Ferromagnetism

There are some paramagnetic materials that do not follow Curie's law, but instead follow the *Curie-Weiss* law:

$$\chi = \frac{C}{T - \theta} \tag{2.12}$$

where θ is a constant, with the dimensions of temperature. Paramagnetic materials which follow the Curie-Weiss law undergo a *spontaneous ordering* and become ferromagnetic below some critical temperature, T_C, which for all practical purposes is equal to θ. When $T = \theta$ the susceptibility diverges and a phase transition to the spontaneously ordered phase occurs.

Weiss explained [14] the spontaneous magnetization in ferromagnetic materials by postulating that unlike paramagnets, there is an internal interaction between the moments, the

molecular field, which does not vanish in the absence of an external magnetic field and results in the alignment of the magnetic moments in the absence of an applied field.

Weiss was able to explain the Curie-Weiss law i.e., Eq. 2.12, by assuming that the intensity of the molecular field is directly proportional to the magnetization

$$\mathbf{H}_w = \gamma \mathbf{M} \tag{2.13}$$

where γ is called the *molecular field constant*. Therefore, the total field would be:

$$\mathbf{H}_{tot} = \mathbf{H} + \mathbf{H}_w \tag{2.14}$$

Replacing $\mathbf{H}_{tot}$ in the Curie susceptibility, Eq. 2.11, results in,

$$\frac{\mathbf{M}}{\mathbf{H} + \gamma \mathbf{M}} = \frac{C}{T} \tag{2.15}$$

which gives,

$$\chi = \frac{\mathbf{M}}{\mathbf{H}} = \frac{C}{T - C\gamma} = \frac{C}{T - \theta} \tag{2.16}$$

which is the Curie-Weiss Law. $\theta = C\gamma$ is a measure of the strength of the interaction and is a property of the material.

2.4.1 Spontaneous magnetization

Using Weiss' theory, we could see how spontaneous magnetization occurs. As discussed in section 2.3, the Langevin theory of paramagnetism tells us that the magnetization is given by Eq. 2.8.

Let us consider a sample in which each atom has a net magnetic moment. Based on the Langevin theory of paramagnetism, the magnetization of the material increases with increasing the applied magnetic field at constant temperature. The solid line in Fig. 2.7, is a plot of magnetization as a function of α. Next, we assume that the only field acting on the material is the Weiss molecular field $\mathbf{H}_w$. Inserting $\mathbf{H} = \mathbf{H}_w$ in the relation for α gives:

$$\alpha = \frac{mH_w}{k_B T} = \frac{m\gamma M}{k_B T} \tag{2.17}$$

which gives [60]:

$$M = \Big(\frac{k_B T}{m\gamma}\Big)\alpha \tag{2.18}$$

Thus, the magnetization is a linear function of α, with the slope proportional to temperature. The dotted and dashed lines in Fig. 2.7 are plots of this equation for $T = T_C$ and $T < T_C$, respectively.

The magnetization that the molecular field will produce in the material is given by the intersection of the two curves. This occurs at the origin (which represents an unstable state) and at the point $\mathbf{M}_{spont}$, where the material is spontaneously magnetized. When the temperature

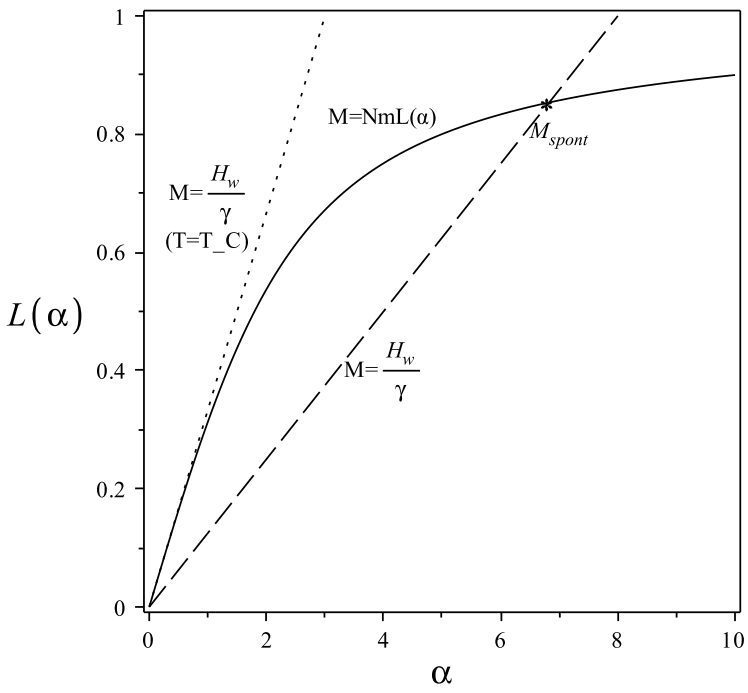

Figure 2.7: Spontaneous magnetization in ferromagnetic materials.

increases, the slope of the line also increases and it intersects with the Langevin function at a smaller spontaneous magnetization.

At $T = T_C$, the only solution is at the origin, meaning that there is no spontaneous magnetization. As the temperature is decreased, the spontaneous magnetization increases smoothly, which is in agreement with the fact that paramagnetic to ferromagnetic transition is a continuous phase transition, as will be discussed in Chapter 4.

The essential aspects of ferromagnetism are illustrated by the implications of the following experimental facts [36]:

It is possible to change the overall magnetization of a suitably prepared ferromagnetic specimen from an initial value of zero (in the absence of an applied magnetic field) to a saturation value of the order of 1000 gauss, by the application of a field whose strength may be of the order of 0.01 oersteds.

The statement above contains two significant observations:

(a) It is possible in some cases to attain saturation magnetization by the application of a very weak magnetic field.

(b) It is possible for the magnetization of the same specimen to be zero in zero (or nearly zero) applied field.

In paramagnets the application of a field of 0.01 oersteds has an entirely negligible effect on the magnetization of a system. For example at room temperature a field of 0.01 oersted will

increase the magnetization of a paramagnetic salt such as ferrous sulfate, by about 10^{-6} gauss, as compared with 10^3 gauss in the ferromagnetic specimen. The small effect in the case of the paramagnetic salt is known to be caused by thermal fluctuations of magnetic moments. In the paramagnetic salt effectively only one magnetic field in 10^9 is oriented by the field of 0.01 oersted, so the distribution of the magnetic moment directions remains random. This high degree of randomness is a result of thermal fluctuations in a system where the magnetic moments are independent, without important mutual interaction.

Weiss pointed out that the randomness caused by thermal agitation could be largely circumvented if one postulated in ferromagnetic materials the existence of a powerful internal molecular field, which is a mutual interaction between electrons which would tend to line up the magnetic moments parallel to one another.

The required magnitude for the Weiss molecular field may be estimated. At the Curie temperature, T_c, the thermal energy $k_B T_c$ of an electron spin is of the same order of magnitude as the interaction energy μH_w of the magnetic moment μ of an electron acted on by the effective molecular field H_w:

$$k_B T_c \approx \mu H_w \tag{2.19}$$

so that

$$H_w \approx \frac{k_B T_c}{\mu} \approx \frac{10^{-16} 10^3}{10^{-20}} \approx 10^7 oersteds \tag{2.20}$$

This is a very powerful effective field. It is about twenty times more intense than any actual magnetic field produced in a laboratory. At temperatures below T_c, the effect of the molecular field outweighs the thermal fluctuation energy and the specimen is accordingly ferromagnetic.

It is known that the origin of the molecular field lies in the quantum mechanical exchange force [36] and the ordinary magnetic moment interaction between electrons is much too weak to account for the molecular field. The magnetic field at a lattice point, arising from the magnetic moment of a neighbouring electron is of the order of:

$$H \approx \frac{\mu}{r^3} \approx \frac{10^{-20}}{(2 \times 10^{-8})^3} \approx 10^3 oersteds \tag{2.21}$$

which is smaller than the effective molecular field H_w by a factor of the order of 10^{-4}.

2.5 Domain Theory

In the previous section we saw how the existence of the powerful Weiss molecular field enables saturation magnetization to be obtained. How do then we explain statement (b) above, that it is possible for the magnetization to be zero in zero applied field? It seems at first sight contradictory, in view of the 10^7 oersted molecular field, to suppose that a 10^{-2} oersted applied field can alter the magnetic moment of the specimen by an appreciable amount [36].

Weiss assumed [14] that the actual specimens are composed of a number of small regions called *domains*, within each of which the local magnetization is saturated; the directions of magnetization of different domains need not necessarily be parallel, however. The increase

in the value of the resultant magnetic moment of the specimen under the action of an applied field may be imagined to take place by an increase in the volume of the domains which are favourably oriented with respect to the field at the expense of unfavourably oriented domains; or by rotation of the direction of magnetization towards the direction of the field, Fig. 2.8.

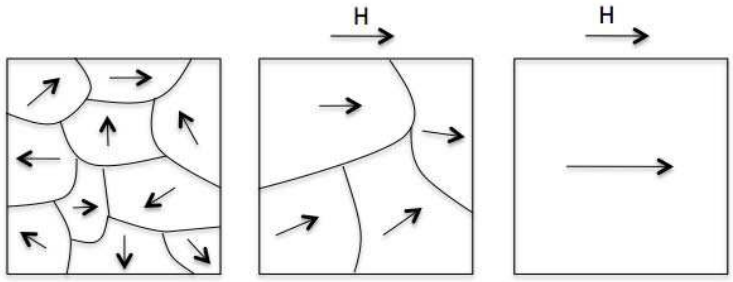

Figure 2.8: Schematic domain arrangement in a ferromagnetic material and magnetization of the sample by domain growth and domain rotation.

In weak fields the magnetization changes usually proceed by means of domain boundary displacements so that the domains change in size. In strong fields the magnetization changes by means of rotation of the direction of magnetization.

2.6 The origin of Domains

There are a number of different contributions to the total magnetic energy of the ferromagnetic material. The formation of domains allows the minimization of the *total free energy* which consists of: exchange energy, magneto-static energy, magnetocrystalline (anisotropy) and magnetostriction (magnetoelestic) energies.

2.6.1 Exchange Energy

Heisenberg showed that the Weiss molecular field could be explained using a quantum mechanical treatment of the many-body problem [60].

Looking at the quantum mechanical calculation for the energy of the helium atom, which has two electrons and provides a simple example of the many-body Hamiltonian shows that there is a term of *electrostatic origin* in the energy of interaction between neighbouring atoms that tends to orient the electron spins parallel to each other. This term is called the *exchange integral* and does not have a classical analog [60].

The exchange interaction is a result of the *Pauli exclusion principle*, which states that no two identical fermions (particles with half-integer spins) may occupy the same quantum state simultaneously [58]. For example, no two electrons in a single atom can have the same four quantum numbers. If n, l, m_l are the same, then m_s must be different such that the electrons have opposite spins. So two antiparallel spins are allowed to share the same quantum mechanical

state. But this results in a spatial overlap of the two electrons which increases the electrostatic Coulomb repulsion. On the other hand, if they have parallel spins, they must occupy different states and will minimize any unfavourable repulsion interaction.

If two atoms i and j have spins of $\mathbf{S}_i$ and $\mathbf{S}_j$, then the exchange energy between them is given by [36]

$$E_{ex} = -J_{ex}\mathbf{S}_i \cdot \mathbf{S}_j = -j_{ex}S_iS_j\cos\phi \tag{2.22}$$

where J_{ex} is a particular integral, called the *exchange integral*, which occurs in calculation of the exchange effect and ϕ is the angle between the spins. If J_{ex} is positive, E_{ex} is a minimum when the spins are parallel and a maximum when they are anti-parallel, which is the case for ferromagnetic materials.

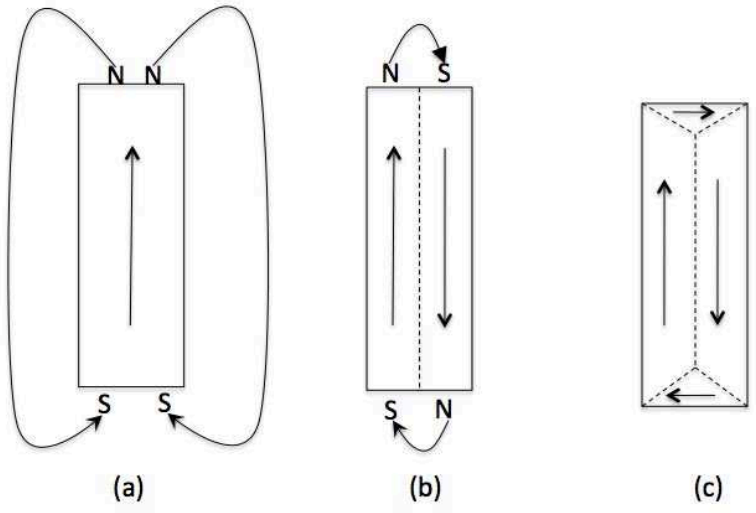

Figure 2.9: Reduction of magnetostatic energy by domain formation. In (a) the external demagnetizing field is big. In (b) the block is divided into domains to decrease the demagnetizing field and therefore the magnetostatic energy. In (c) the triangular domains at the top and bottom of the sample allow the magnetostatic energy to be completely zero, as they are paths by which the flux can close on itself.

2.6.2 Magnetostatic Energy

Magnetostatic energy is a self-energy [36]. A magnetized rod of a ferromagnetic material has a macroscopic magnetization and therefore has a magnetic field around it, called the *demagnetizing field*, which as figure 2.9 shows, acts in the opposite direction from the sample's magnetization and tends to decrease it. The magnetostatic energy is caused by the demagnetizing field. It could be reduced by breaking a single domain in Fig.2.9-b to two domains to decrease the demagnetizing field although this increases the exchange energy. The triangular domains at the top and bottom of the crystal in Fig. 2.9-c are called *domains of closure*. This domain

configuration does not have any magnetic poles at the surface of the sample, and accordingly the demagnetizing field is zero in this configuration.

2.6.3 Magnetocrystalline Energy

The anisotropy energy or the magnetocrystalline energy is minimized when the magnetization aligns in certain definite crystallographic axes, which are called *directions of easy magnetization*. Measurements show that in iron, for example, the saturation magnetization can be achieved with quite low fields, of order of a few tens of oersteds in the direction of easy magnetization <100>[2], while it takes high fields, of the order of several hundred oersteds to saturate iron in <111> direction which is accordingly called the *hard direction of magnetization*.

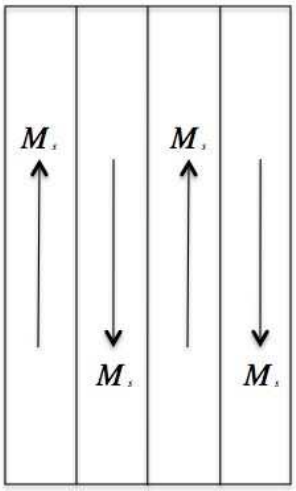

Figure 2.10: Domain configuration that minimizes the magnetocrystalline energy in a uniaxial crystal.

To minimize the magnetocrystalline energy, the domains will form so that their magnetization is along the easy direction. For a uniaxial crystal (like hexagonal crystals of cobalt) the domain structure is particularly simple, as seen in Fig. 2.10. The domains of closure form when the material has easy axes that are perpendicular to each other. In such materials, this configuration is favourable because it eliminates the magnetostatic energy, without increasing the magnetocrystalline anisotropy energy [60].

[2]The orientation of a plane is given by a vector normal to the plane. There are reciprocal lattice vectors normal to any family of lattice planes. It is customary in solid states physics to use the shortest such reciprocal lattice vector to describe a plane. These are called the *Miller indices* of the plane [4]. Lattice planes are denoted by their Miller indices in parentheses. Suppose that a single crystal is cut, in such a way that it has faces with the following Miller indices: (100), (010), (001), $(\bar{1}00)$, $(0\bar{1}0)$ and $(00\bar{1})$. Then to specify a direction, the indices of a particular direction are denoted by square brackets [100], [010], [001], $[\bar{1}00]$, $[0\bar{1}0]$ and $[00\bar{1}]$. These are directions of a form, and the whole set is designated by the indices of anyone, enclosed in angular brackets <100>.

The origin of the magnetocrystalline anisotropy is the *spin-orbit coupling* [58]. Because of this coupling, the orbit of the electrons needs to be reoriented when the spin aligns along an applied magnetic field. However, the orbit is strongly coupled to the lattice. This explains the resistance against the rotation of spin, due to the magnetocrystalline anisotropy.

2.6.4 Magnetostriction Energy

The change in the dimensions of a ferromagnetic material in the presence of an external magnetic field is called magnetostriction effect [14]. The fractional change in length $\Delta l/l$ is simply a strain, which is different from the strain caused by an applied stress. The magnetically induced strain, which can be negative or positive, is given by:

$$\lambda = \frac{\Delta l}{l} \tag{2.23}$$

Magnetoscriction is described using a quantity called the *magnetistrictive coefficient*, L, and is defined as the fractional change in length of the sample as the magnetization of the material increases from zero to the saturation value. It is a very small quantity, of order of $L \sim 10^{-5}$ for magnetic materials such as Iron, Nickel and Cobalt [9].

In iron, the magnetostriction causes the domains of closure in Fig. 2.9-c to try to elongate horizontally, and the long vertical domains try to elongate vertically. Since both elongations can not happen at the same time, a change in the length of the substance happens [60]. An elastic strain energy term is added to the total free energy, to explain this effect. This elastic energy is proportional to the volume of the domains of closure and can be lowered by reducing the size of closure domains, which results in smaller domains. This increases the exchange energy. The *total free energy* is minimized by a compromised domain arrangement such as that shown in Fig.2.11

Magnetostriction effect is also due to *spin-orbit coupling*. The mechanism of magnetostriction is schematically shown in figure 2.12. The picture shows a section through a row of atoms in a crystal. Below the Curie temperature, they orient about the easy axis (horizontal axis in this picture) due to the spin-orbit coupling [14].The change in length of the specimen occurs when the specimen is exposed to strong fields. Then the spins and electron orbitals would rotate to be parallel to the direction of the field and the domain of which theses atoms are a part would experience a strain $\Delta l/l$.

2.7 Coercive Force

When a magnetic field is applied to a specimen at an angle which is different from the easy axis, the domain with the magnetization direction that is the closest to the field direction starts to grow by domain wall motion. At first, this motion is reversible, which means that if the field is removed, the demagnetized state of the specimen is regained. If we continue applying external magnetic field, the domain walls continue moving and they might encounter imperfections such as defects. These defects possess a magnetostatic energy, because of the poles on their surface.

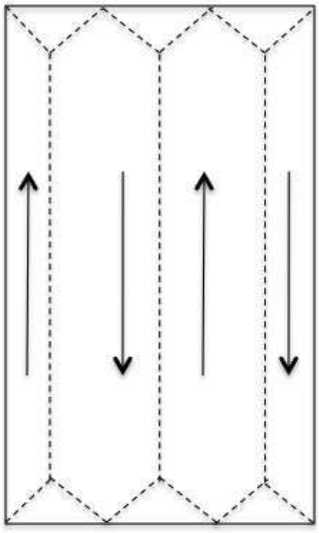

Figure 2.11: A domain arrangement that reduces the total energy which is the sum of of exchange, magnetostatic, magnetocrystalline and domain wall energy.

When a magnetic domain boundary crosses the imperfection, the poles will be removed by formation of closure domains and therefore the magnetostatic energy could be eliminated. A local energy minimum occurs in the intersection of the magnetic domain boundary and the crystal imperfection. This is a local minimum, and energy is needed to move the domain boundary and pass it over the imperfection. This energy is provided by the applied magnetic field. Eventually the applied field will remove all domain walls and produce a single domain.

When the magnetic field is removed, the dipoles rotate back to their easy axis. Now the domain walls should move back to their initial state. However, the demagnetizing field is much weaker than the applied external magnetic field and is not strong enough to overcome the energy barriers and pass the magnetic domains across the imperfections. Therefore, the sample remains partially magnetized when the external magnetic field becomes zero. The *coercive force* is the field required to move the domain boundary, to completely demagnetize the sample, shown by H_c in Fig. 2.4.

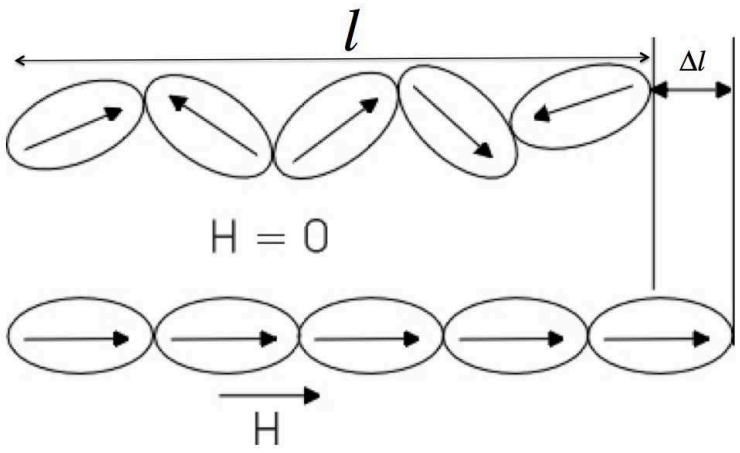

Figure 2.12: Magnetostriction effect.

Chapter 3

Solidification and the Origin of Grain Structure

In this chapter, the classical approach to the solidification of a pure liquid (the Stefan problem), the equilibrium phase behaviour of binary mixture and different kinetics observed in the phase transition process (nucleation and spinodal decomposition) are considered. The discussion about the solidification is provided, as a background to understand the physics behind the crystallization from an undercooled melt in the PFC simulations (Chapter 6). Discussions regarding the equilibrium phase diagram of the binary mixture provide the basis to understand the common tangent construction used in Chapter 8 to calculate the phase diagram of the Magnetic PFC model. Finally, the differently oriented grains resulting from nucleation at different sites of the system are considered and the experiments on the dependence of magnetic hardness on grain size are explained in Section 3.3. The results of the simulations, using the Magnetic PFC model to reproduce these experimental data are reported in Chapter 9.

The process of crystal growth from a liquid phase is referred to as solidification [43]. In general, complex patterns can be produced in a solidification process, which are controlled by the external conditions at which a crystal is growing. A natural example of crystal growth is the formation of snowflakes, which have dendritic (tree like) microstructure. These structures are controlled by the temperature and humidity and the concentrations of various air pollutants. A typical dendritic microstructure, developed by immersing a crystalline seed in its undercooled melt, is shown in Fig. 3.1.

Dendritic structure also occurs in solidification of alloys. The patterns are very sensitive to growth conditions and material parameters. In these microstructures, defects and chemical inhomogeneities, which have been formed during the solidification process, determine the mechanical, thermal, electric and magnetic properties of solids. For example yield strength of a polycrystal varies as the inverse square of the average grain size [19]. Accordingly, understanding the solidification process is very important since it forms the basis for controlling the microstructure and therefore the macroscopic properties and behaviour of alloys.

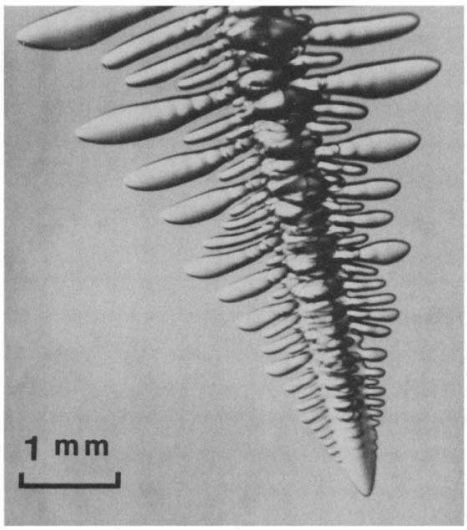

Figure 3.1: Primary dendrite of succinonitrile (a transparent crystal with cubic symmetry) growing in its undercooled melt. Note the smooth paraboloidal tip, the secondary sidebranching oscillations emerging behind the tip and the beginning of tertiary structure on the well-developed secondaries [44] .

3.1 Solidification of a pure liquid

The simplest solidification process is the solidification of a pure substance from its melt, for example, the freezing of ice from water. For a pure substance, solidification is completely governed by *heat flow*. The rate of solidification at any point is controlled by how fast the latent heat released, can be transferred into the bulk or removed at the boundaries [43]. Solidification of a material with a melting point above the ambient temperature will take place once some of the solid has formed.

Considering the solidification in a container or mould, the heat effectively is being transferred to the ambient environment via the mould. The heat flux from the hot melt to the surrounding material allows the liquid to cool and to transform to solid and the solid to cool to reach the temperature of the surrounding medium.

In the case of a pure material, the basic element in the mathematical problem of predicting the motion of the solidification interface is a diffusion field, i.e., the temperature T which satisfies the diffusion equation

$$\frac{\partial T}{\partial t} = D_T \nabla^2 T \tag{3.1}$$

where D_T is the thermal diffusion constant. We need to write Eq. 3.1 for the liquid and solid phases, with different values of diffusion constants (D_T and D'_T). We also need the condition of heat conservation at each point on the moving interface:

$$L v_n = \left[D'_T c'_p \left(\nabla T\right)_{solid} - D_T c_p \left(\nabla T\right)_{liquid} \right] \cdot \hat{n} \tag{3.2}$$

where L is the latent heat per unit volume of the solid, c_p and c'_p are the specific heats per unit volume of the liquid and solid, respectively; v_n is the normal velocity of the interface and $\hat{n}$ is the normal vector of the interface. Thus, the left-hand side is the rate at which heat is generated at the boundary and the right-hand side is the rate at which this heat flows into the bulk phases on either side.

To describe the motion of the solidification front, this model also needs a thermodynamic boundary condition at the interface. The simplest choice would be that the temperature along the surface of the interface must be equal to the bulk melting temperature. With this condition we reach to a relatively tractable mathematical problem, the *Stefan problem* [43]. However this simple condition omits the effect of surface tension which is a crucial force in pattern formation problems.

In fact, for any solid/liquid bulk of volume V which is enclosed by an interface of area A, there is an excess interface energy which is required for its creation. So in inhomogeneous systems, part of the system which has a higher A/V ratio, has a higher energy and therefore less stable relative to a part which has a lower A/V ratio. The relative stability can be related to the equilibrium temperature of the two phases (melting point).

The correct form of the thermodynamic boundary condition is:

$$T_{interface} = T_M \left[1 - (\gamma K/L)\right] - \beta(v_n) \tag{3.3}$$

where γ is the liquid-solid surface tension, K is the curvature of the interface, defined to be positive for a convex solid and T_M is the melting temperature of the bulk. The term $\beta(v_n)$ is a function of the normal interface velocity to correct for kinetic effects. A linear function $\beta = \beta_0 v_n$ would be accurate for a rough interface. Equation (3.3) is called the *Gibbs-Thomson* relation [43], which describes the change in melting point ($T_{interface} - T_M$) due to the curvature effect. Equations (3.1), (3.2) and (3.3) completely specify the model of solidification of a pure substance.

A useful analysis to study the stability of a particular pattern in the process of solidification is the *Mullins-Sekerka Instability* [43]. The basic idea in this method is to introduce a perturbation in the original interface shape and to determine whether this perturbation will grow or decay [49].

Using the linear stability analysis [43], it is observed that simple shapes such as planes, spheres, cylinders, etc., are unstable under certain commonly encountered conditions and more complicated patterns are formed. This instability occurs because on the one hand, diffusion kinetics favours as large a surface area as possible so that latent heat can be dissipated more rapidly; on the other hand the surface tension increases when the ratio A/V increases. It is the interplay between these two effects which produces the complex growth patterns observed in nature.

3.2 Kinetics

The Ginzburg-Landau theory of phase transition discussed in Chapter 4 gives us information about which equilibrium phase has the lowest free energy. This description, however, is not enough to explain different structures observed in material physics. To have a better under-

standing of the process, we need to look at the *kinetics* of the process by which the phase transition happens.

A change in temperature of a liquid that is so rapid that the state of the system immediately after the change is still liquid, is called a *quench*. After the system is quenched, the undercooling, i.e., the difference between the temperature of the undercooled liquid and the melting temperature will drive the system to solid phase, to minimize the free energy.

3.2.1 Phase diagram

In this section a brief description on the phase diagram of a binary liquid mixture is provided. The discussions of this section are based on [34] and help us to understand the phase behaviour of a system with two phases that are different in concentration or density, in the temperature-concentration plane. This produces the basic framework of phase diagram calculation of the Magnetic PFC model in Section 8.2.

In order to understand the kinetics of phase transitions, we look at a simple example: The situation in which two liquids of types A and B in a *closed* container are miscible in all proportions at high temperature, but separate into two distinct phases (A-rich zones and B-rich zones) when the temperature is lowered. To calculate the equilibrium states of the system as a function of the temperature and composition, i.e., the *phase diagram*, the free energy of mixing is estimated using the mean field theory. The mean field assumption here is that a given site of the system has $z\phi_A$ (A) neighbours and $z\phi_B$ (B) neighbours whether the site is occupied by A or B molecules.

The order parameter is taken to be the volume fraction of A molecules, η_A, which is defined to be the volume of A molecules divided by the total volume of the system. If the system is incompressible, $\eta_B = 1 - \eta_A$. If we know the volume fraction of A, then the volume fraction of B can be calculated; therefore, from here on we assume all volume fractions refer to A. The details of the calculation can be found in [34]. Here, we only consider the main results of the calculation which enables us to understand the phase diagram.

The free energy of mixing F_{mix} is

$$F_{mix} = F_{A+B} - (F_A + F_B) \tag{3.4}$$

where F_{A+B} is the free energy of the system if A and B are mixed in a single container, F_A is the free energy of the system containing A molecules only and F_B is the free energy of the system containing B molecules only.

It is shown in [34] that the free energy of mixing is equal to

$$\frac{F_{mix}}{k_B T} = \eta \ln \eta + (1-\eta)\ln(1-\eta) + \chi\eta(1-\eta) \tag{3.5}$$

where χ is the energy change in units of $k_B T$ when a molecule A is taken from an environment of pure A and put into an environment of pure B. It expresses the strength of the energetic interaction between the A and B components. It is temperature dependent and varies as $1/T$ with the temperature. The first two terms in Eq. 3.5 are the entropic contributions to the free energy.

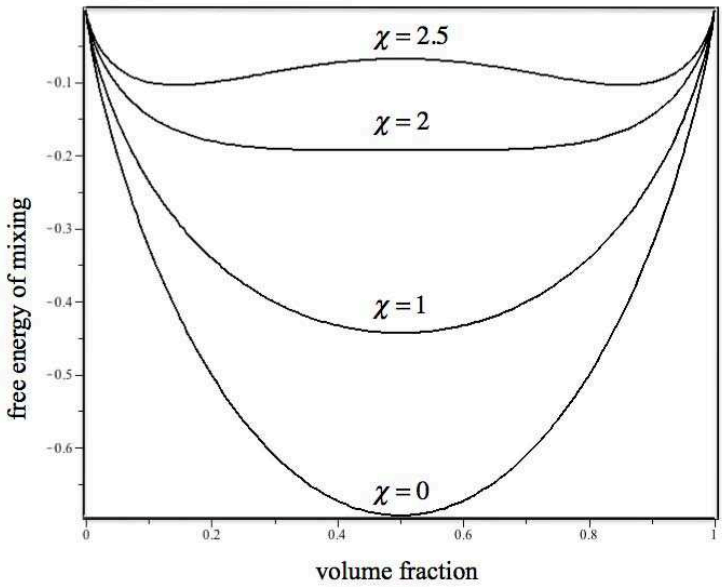

Figure 3.2: Plots of the free energy of mixing, Eq. 3.5 for different values of χ. The system has one minimum for the interaction parameters $\chi < 2$, at a volume fraction of $\eta = 0.5$. This means that the mixture is miscible, regardless of the initial proportions of A and B. For $\chi \geq 2$ the free energy has two minima and a maximum at $\eta = 0.5$.

If we plot the free energy curve as a function of the volume fraction η, for different values of χ (Fig. 3.2), we see that for $\chi < 2$ the curve has a global minimum at $\eta_A = \eta_B = 0.5$. For $\chi \geq 2$ the curve has two minima, and a maximum at $\eta_A = \eta_B = 0.5$.

To understand whether a phase-separated phase is stable or the mixture, we need to calculate the free energy of the phase-separated system, F_{sep}, and compare it with that of the mixed system, F_{mix}. We consider a volume, V_0, of mixture whose starting volume fraction is η_0. If the mixture separates into a region of volume, V_1, with volume fraction, η_1, and a region of volume, V_2, with volume fraction, η_2, then we have $\eta_0 V_0 = V_1\eta_1 + V_2\eta_2$. This is due to the fact that the system is closed and the total number of A and B is conserved. Thus we can write

$$\eta_0 = \alpha_1\eta_1 + \alpha_2\eta_2 \tag{3.6}$$

where α_1 and α_2 are the relative proportions of the two phases and

$$\alpha_1 + \alpha_2 = 1 \tag{3.7}$$

The free energy of the phase-separated system, $F_{sep} = \alpha_1 F_{mix}(\eta_1) + \alpha_2 F_{mix}(\eta_2)$, can be written as

$$F_{sep} = \frac{\eta_0 - \eta_2}{\eta_1 - \eta_2} F_{mix}(\eta_1) + \frac{\eta_1 - \eta_0}{\eta_1 - \eta_2} F_{mix}(\eta_2) \tag{3.8}$$

To derive this equation, we used Eqs. 3.6 and 3.7. This is the equation of a straight line passing through $F_{mix}(\eta_1)$ and $F_{mix}(\eta_2)$. The free energy of the phase-separated system is therefore equal

to the value of this straight line at the volume fraction η_0. For a concave curve this free energy is higher than the free energy, $F_{mix}(\eta_0)$, for all values of η_1 and η_2. This situation is shown in Fig. 3.3-a. This means that for all $\chi < 2$ values or equivalently for all temperatures greater than a critical temperature, the mixture is miscible, regardless of the initial proportions of A and B.

If there is any region of compositions for which the free energy curve is convex, then there are some initial compositions that can lower the free energy by phase separation. Such regions can be found in the free energy curve shown in Fig. 3.3-b. The free energy of the phase-separated system, is evaluated by calculating the value of the straight line "1", joining two compositions η_1 and η_2, at η_0. It can be observed in the figure that it is less than the free energy of the mixed system at η_0. Thus, at this temperature there exist initial compositions that are unstable with respect to phase separation.

The limiting compositions, η_1, and η_2, that separate the regions of concavity of the free energy from the regions of its convexity are the compositions that are joined by a *common tangent*, line "2", and are known as the *coexisting* compositions. If we increase χ or decrease the temperature,the composition range enclosing the unstable phase increases. Thus in the phase diagram the region enclosed by the coexistence line should become wider as the temperature is decreased.

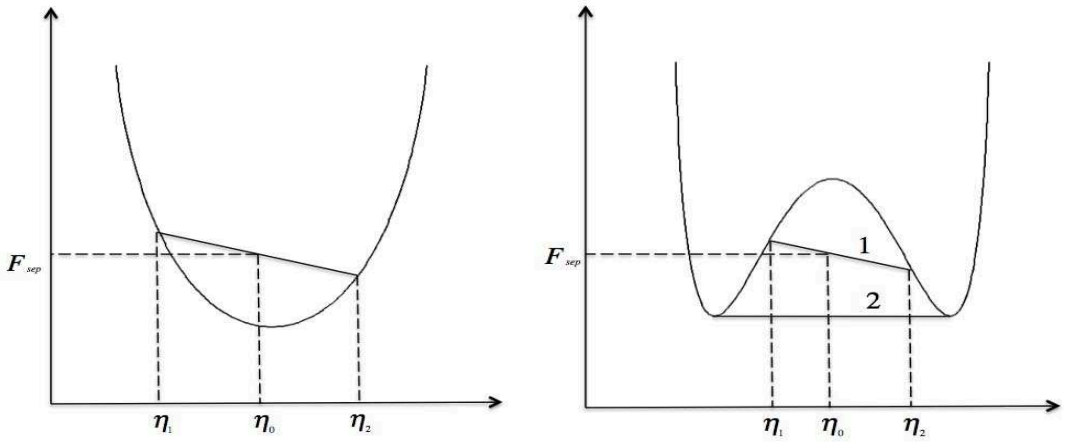

(a) The plot of F_{mix} for $\chi = 1$ (b) The plot of F_{mix} for $\chi = 2.6$

Figure 3.3: The free energy of mixing for different values of the interaction parameter, χ or equivalently at different temperatures. In (a), the free energy of mixing is concave and has one global minimum. Thus the value of $F_{sep}(\eta_0)$ is greater than $F_{mix}(\eta_0)$ for all compositions η_1 and η_2 and the mixture is stable at all proportions. In (b), χ is increased or correspondingly the temperature is decreased. F_{mix} has both regions of convexity and concavity. Line "1" in this plot, joining the compositions η_1 and η_2, represents a situation in which $F_{sep}(\eta_0)$ if less than $F_{mix}(\eta_0)$ and therefore the system is unstable with respect to phase separation. Line "2" in this plot joins the limiting compositions that separate the regions of convexity (unstable) and concavity (stable) of the free energy. These compositions define the coexistence line in the phase diagram.

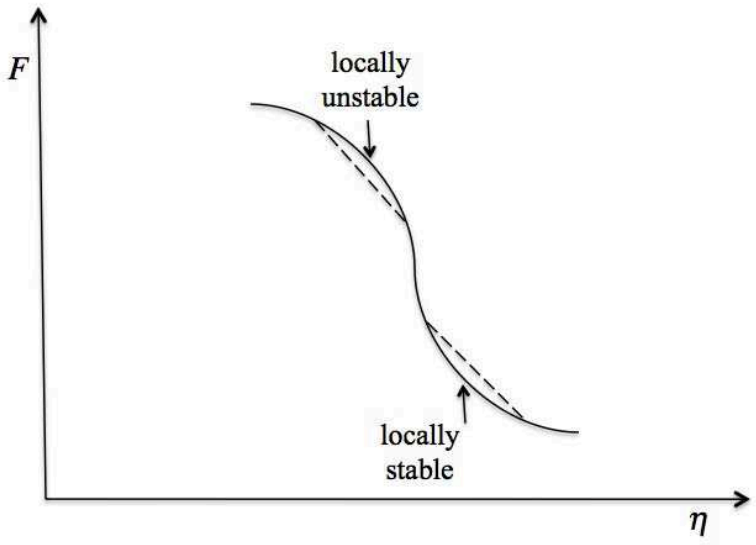

Figure 3.4: The free energy of mixing as a function of the composition. This figure schematically shows a composition in which the system is locally stable (metastable) and a composition in which the system is unstable.

For the compositions that are within the coexistence curve there is another distinction: the curvature of the free energy in this region might be either positive or negative. As shown in Fig. 3.4 the system might be either locally stable or locally unstable although it is globally unstable. This means that there exist some compositions in this region that are unstable with respect to small fluctuations in composition (locally and globally unstable). Any small fluctuation in composition will cause a phase separation. On the other hand there exist compositions where the system is locally stable with respect to separation into two coexisting phases although it is globally unstable. These are the compositions at which the system is in the state of *metastability*. In this case, if the fluctuation is big enough to overcome the free energy barrier, the system will phase separate. But if the fluctuation is small the system will not "see" that it is in the globally unstable phase and will not phase separate. The limit of local stability is determined by the condition that $d^2F/d\eta^2 = 0$ and defines the *spinodal line*.

With this information about the free energy, we can determine the equilibrium phase of a liquid-liquid mixture at a particular temperature and density, i.e., we can calculate the *phase diagram*. Figure 3.5 shows the phase diagram of such systems. It can be observed in the figure that at a certain point on top of the coexistence line, the stable phase and unstable phase are indistinguishable. This point is the the *critical point* of the phase diagram. Above this point, it is possible to pass to different volume fractions without going through a coexistence region.

As shown in Fig. 3.5, if a mixture having a particular initial value of composition, η_0, is quenched down below the coexistence line or equivalently if χ is increased, it will phase separate to regions with composition η_1 (B-rich regions) and regions with composition η_2 (A-rich regions).

In general to calculate the coexistence lines in a phase diagram the free energy of the system, Eq. 3.5, should be minimized with the constraints that the total number of the particles

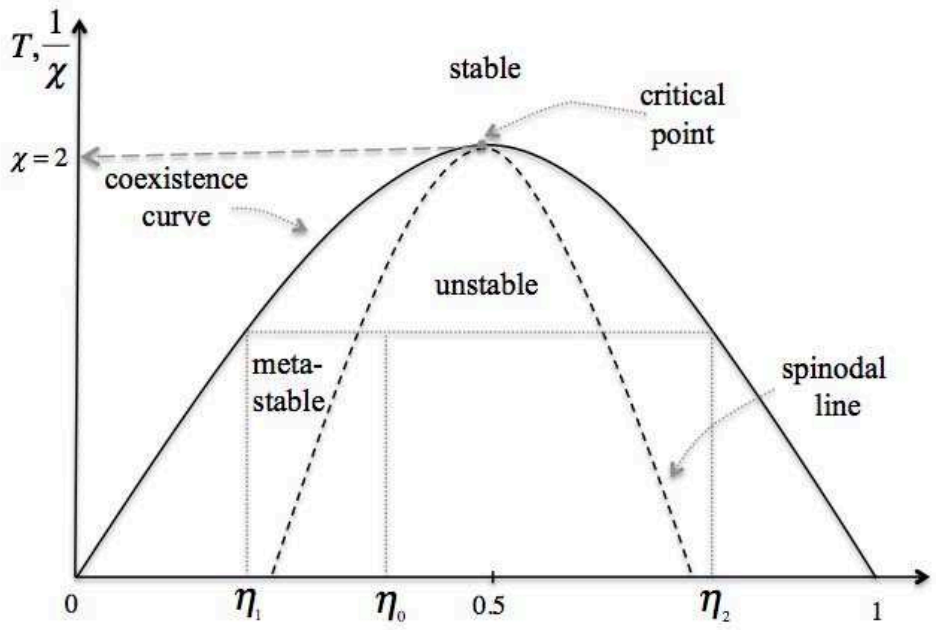

Figure 3.5: The phase diagram of a binary liquid mixture. The horizontal axis is the volume fraction of the A component. If we prepare the system at an initial volume fraction, η_0, and quench the system to the unstable region of the phase diagram, it will separate into two phases with volume fractions η_1 (B-rich) and η_2 (A-rich).

$N = N_1 + N_2$ is a constant and that $\eta_0 = \alpha_1\eta_1 + \alpha_2\eta_2$, i.e., Eq. 3.6. Minimizing with these two constraints gives us a set of equations that is the mathematical formulation for the common tangent construction [56]

$$\mu = \frac{\partial F_{mix}}{\partial \eta_1} = \frac{\partial F_{mix}}{\partial \eta_2} \tag{3.9}$$

$$\mu = \frac{F_{mix}(\eta_1) - F_{mix}(\eta_2)}{\eta_1 - \eta_2} \tag{3.10}$$

These sets of equations were used to calculate the phase diagram of the phase-field crystal [16].

As the phase diagram suggests, depending on whether the system is quenched to a metastable state or to an unstable state, different dynamics towards the phase separation is observed. If the system is quenched to the metastable state, nucleation dynamics occurs. In this region any local fluctuation in the composition needs to be large enough (greater than a critical size) to give the system enough energy to jump out of the metastable state and achieve the global energy minimum by phase separation. On the other hand if the system is quenched to the region within the spinodal line, the system is globally unstable and any small local change in composition lowers the free energy and therefore is amplified.

3.2.2 Nucleation

Considering the phase diagram in Fig. 3.5, if a mixture is quenched into the metastable part of the phase diagram, it will be stable with respect to small changes in concentration and so the continuous process of spinodal decomposition does not occur in this case. Instead, the approach to equilibrium occurs via nucleation of droplets of the other phase. This causes a temporary increase in free energy. As the droplet grows further, the free energy starts to decrease again. The nucleation occurs by a thermal fluctuation which is large enough to overcomes the energy barrier for growth of the droplet [34].

The energy barrier for formation of droplets is due to the surface tension, γ, associated with the formation of an interface. This has a positive contribution to the free energy. There is also a negative contribution to the free energy which is proportional to the volume of the droplet. This is due to the fact that the mixture is globally unstable, so that if it continues to phase separate, the free energy of the system will be lowered. Therefore, we can estimate the net change in free energy when a droplet of size r is forming:

$$\Delta F(r) = \frac{4}{3}\pi r^3 \Delta F_v + 4\pi r^2 \gamma \tag{3.11}$$

where ΔF_v is the bulk energy per unit volume which is defined to be negative.

This energy has a maximum for a critical value r^*. Droplets of a size below r^* are unstable and they shrink away. Once the size of the droplet grows more than r^*, the bulk term becomes dominant, the droplet becomes stable, and the free energy of the system is lowered. The critical radius can be easily calculated and is equal to:

$$\Delta r^* = -\frac{2\gamma}{\Delta F_v} \tag{3.12}$$

Nucleation can occur only if a fluctuation occurs which increases the local free energy by an amount $\Delta F(r^*)$. The nucleation barrier is greatly reduced in the presence of dust and other foreign particles in the melt as well as the walls of the containers in which solidification is occurring. This kind of nucleation is called *heterogeneous* which in practice is much more common than the *homogeneous* nucleation, explained above. Heterogeneous nucleation has a faster growth rate relative to homogeneous nucleation.

In the case of solidification to a crystal phase, if the nucleation process successfully occurs in different regions of the system, the crystals will start to grow. These regions, having crystal structures in arbitrary directions, are called *grains*. The grains grow until they impinge and form grain boundaries. The grain boundaries are considered as defects since they tend to decrease electrical and thermal conductivity of the material. Figure 3.6 shows differently oriented grains and grain boundaries.

3.3 Grain size and magnetic properties

As discussed in section 2.7, the hysteresis properties of a sample depend mainly on its purity, quality and defects. Therefore, we can design materials to optimize their properties for desired applications. For example if there are many defects or impurities in a sample, we need a larger field to magnetize it, but it will retain much of its magnetization when the field is removed.

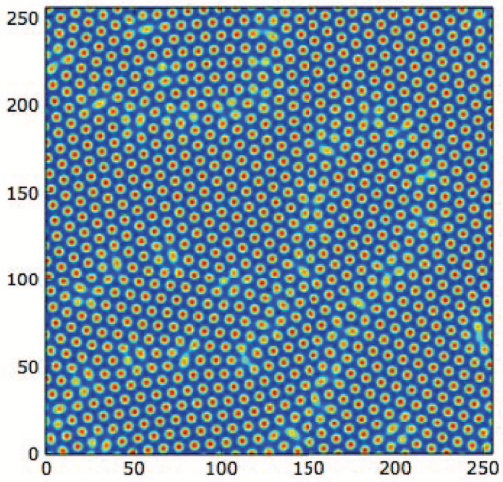

Figure 3.6: Differently oriented grains and the grain boundaries between them. This structure is produced by performing a phase field crystal simulation. The system was initialized with a supercooled liquid, and a few seeds were nucleated at arbitrary positions of the system. As the simulation starts, the crystal state starts to form and grow from the positions where the seeds are located. The grains grow until they contact and the boundaries between them form. The configuration shown here is the final state of the system, in which the crystal has filled the whole system, with grain boundaries between different grains.

Materials with higher remanence and larger coercive force are called *hard* magnetic materials and are used as permanent magnets [60].

High purity materials, which have few defects or dopants are easily magnetized and demagnetized. These are known as *soft* magnetic materials. Soft magnetic materials are of great importance in electromagnets and transformer cores, where they must be able to reverse their direction of magnetization rapidly and the energy loss must be low [60].

It is known that microstructure, notably the grain size D, determines the hysteresis curve of a ferromagnetic material [29]. Figure 3.7 summarizes the coercivity, H_c, observed in the whole range of grain sizes starting from amorphous alloys with grain sizes, in the nanometer regime up to permalloy with macroscopic grain sizes. It can be seen that there are two regimes in the plot of coercivity vs. grain size: In the regime of small grains, the coercivity increases with the grain size as D^6. On the other hand if the grains are larger than a cetrian value ($D > 100\mu m$), the coercivity decreases with grain size as $1/D$.

The *Random Anisotropy Model* is a model introduced by Herzer (1989) to explain the crossover observed in Fig. 3.7. The basic idea of RAM is schematically shown in Fig. 3.8. Based on the RAM, the ratio of the grain size and the ferromagnetic exchange length determines the hardness of the material, *i.e.,* its coercivity. If the grain size is smaller than the ferromagnetic exchange length, the local magneto-crystalline anisotropy is randomly averaged out by exchange interaction so that there is only small anisotropic net effect on the magneti-

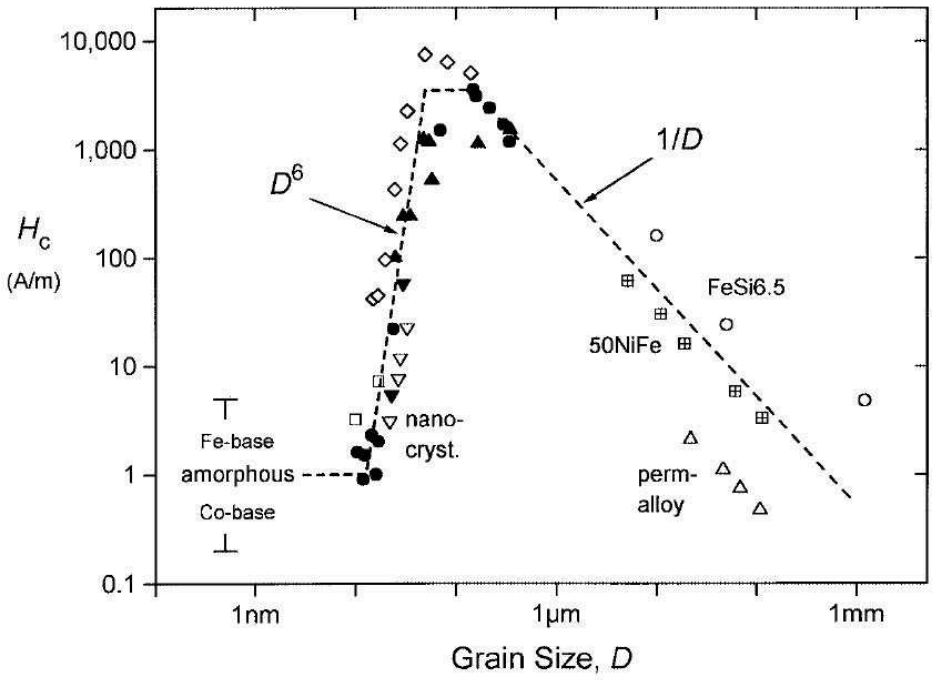

Figure 3.7: Figure and caption from [29]; Coercivity, H_c, vs. grain size, D, for various soft magnetic metallic alloys: Fe-Nb-Si-B (solid up triangles, Herzer 1990), Fe-Cu-Nb-Si-B (solid circles, Herzer 1990-1995 and Herzer and Warlimont 1992), Fe-Cu-V-Si-B (solid and open down triangles, this work and Sawa and Takahashi 1990, respectively), Fe-Zr-B (open squares, Suzuki et al. 1991), Fe-Co-Zr (open diamonds, Guo et al 1991), NiFe alloys (+ center squares and open up triangles, Pfeifer and Radeloff 1980) and Fe-Si (6.5 wt %)(open circles, Arai et al. 1984).

zation process [28]. In this case, the smaller the grain size, the more effective averaging and the smaller the coercivity (the D^6 regime).On the other hand if the grain size is big enough, the ferromagnetic exchange length lies within a single grain. Obviously in this case as the grain size is increased, the anisotropy decreases (the 1/D regime).

The soft magnetic properties and the D^6 dependence of the coercivity in amorphous materials observed in Fig. 3.7 is discussed in [2]. In this work a computer simulation study of ferromagnets with random-axis uniaxial anisotropy is presented, using a simple model. The continuum free energy density they used to model amorphous ferromagnets is composed of two competing terms

$$F(\mathbf{r}) = A\left[\frac{\nabla \mathbf{M}(\mathbf{r})}{M_0}\right]^2 - K_2\left[\frac{\mathbf{M}\cdot\hat{n}(\mathbf{r})}{M_0^2} - \frac{1}{3}\right] \tag{3.13}$$

where $\mathbf{M}(\mathbf{r})$ is the local magnetization vector, M_0 is its magnitude, A is the exchange stiffness parameter, K_2 is the strength of local uniaxial anisotropy and $\hat{n}(\mathbf{r})$ is a unit vector giving the local easy axis direction. The first term in the free energy includes the free energy cost of

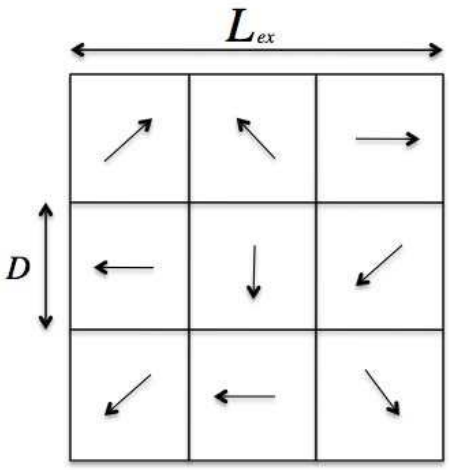

Figure 3.8: Figure from [28]: The basic idea of the Random Anisotropy Model. The arrows show the randomly fluctuating anisotropy axis with correlation length of D and the ferromagnetic correlation length is represented by the exchange length L_{ex}.

changes in $\mathbf{M}(\mathbf{r})$. This term incorporates the exchange energy described in Section 2.6.1. The second term is associated with the magnetocrystalline energy described in section 2.6.3 and it is minimized when the magnetization aligns with the easy axis of the crystal. The anisotropy direction is assumed to vary over a structural correlation length D.

The optimal magnetic correlation length L over which $\mathbf{M}(\mathbf{r})$ varies is calculated assuming that $L \gg D$, so that the magnetization fluctuations average over many regions with different anisotropy direction. In a region of volume L^3, there will be an easiest direction determined by the statistical fluctuations.As in a random walk, the mean fluctuation amplitude varies as the square root of number of independent contributions. It follows that if the moment points along the easiest direction, the average anisotropy energy density is

$$F^a \sim -K_2(\frac{D}{L})^{\frac{3}{2}} \tag{3.14}$$

and the average exchange energy is given by:

$$F^{ex} \sim \frac{A}{L^2} \tag{3.15}$$

The total free energy, $F^{tot} = F^a + F^{ex}$, is minimized by solving the equation $\partial F^{tot}/\partial L = 0$. The value of L which minimizes the total free energy is given by

$$L \sim \frac{16A^2}{9K_2^2D^3} \tag{3.16}$$

and the energy associated with the fully aligned state is

$$F \sim \frac{K_2^4 D^6}{A^3} \tag{3.17}$$

The field necessary to uniformly rotate the moments into alignment, i.e., the coercivity is approximately given by [13]

$$H_s = -F/M_0 \tag{3.18}$$

Combining Eqs. 3.17 and 3.18, we obtain the relation for the intrinsic coercivity of a perfectly random amorphous material to be [2]

$$H_c \sim \frac{1}{20} \frac{K_2^2 D^6}{A^3 M_0} \tag{3.19}$$

This relation applies providing the magnetic length scale L is much greater than the structural length scale D.

Chapter 4

Landau-Ginzburg Theory of Phase Transition

In this chapter a review of the Landau-Ginzburg formalism to study phase transitions, such as ferromagnetic phase transition is given. The LG free energy is the main ingradient of the Phase Field method (Chapter 5) to study the dynamics of the order parameter (magnetization in the ferromagnetic transition and density in liquid-solid transition). As will be explained in this chapter, the LG phenomenological free energy is written as a polynomial expansion in terms of the relevant order parameter and its gradients. This provides the background needed to understand the derivation of the PFC free energy, explained in Chapter 6, to model the phase transition from liquid to a crystal phase.

To study how phase transitions happen, it is useful to classify phase transitions into two categories: *first order phase transitions* and *continuous phase transitions*. A rather quantitative definition of the nature of the phase transition is possible using f, the free energy[1]. A phase transition is defined as the possible *non-analyicities* of f [21].

If the derivative of the free energy with respect to one of the thermodynamic variables is discontinuous, the transition is said to be *first order*. As will be discussed later, in a first order phase transition, the two phases coexist at the transition point and a *latent heat* is involved.

On the other hand if the first derivative of f with respect to all the thermodynamic variables is continuous and the discontinuity occurs in higher order derivatives. the phase transition is called a *continuous* phase transition. Neither coexistence nor latent heat is involved in a continuous phase transition.

The phase diagram of a typical solid-liquid-gas system is depicted in Fig. 4.1. It shows the state of the matter at a particular temperature and pressure. The double lines denote phase boundaries and the two phases coexist in the regions between the double lines.

As apparent from the figure, there is a line along which the liquid and gas phases coexist, but it terminates at a point called the *critical point*. Beyond the critical point, it is possible to go from liquid to gas without any phase transition, i.e., no singular behaviour in the thermodynamic quantities. This is a reflection of the fact that liquid and gas have the same symmetry [21]. However, a fluid has a higher degree of symmetry than a solid. Therefore, it is not

[1]The free energy is defined by $f = -k_B T lnZ$, in which k_B is the Boltzman constant, and Z is the partition function which is defined as $Z \equiv Tre^{-H/k_B T}$. The operation Tr means "sum over all degrees of freedom", H is the hamiltonian of the system and T is the temperature.

possible to go from liquid to solid without a phase transition.

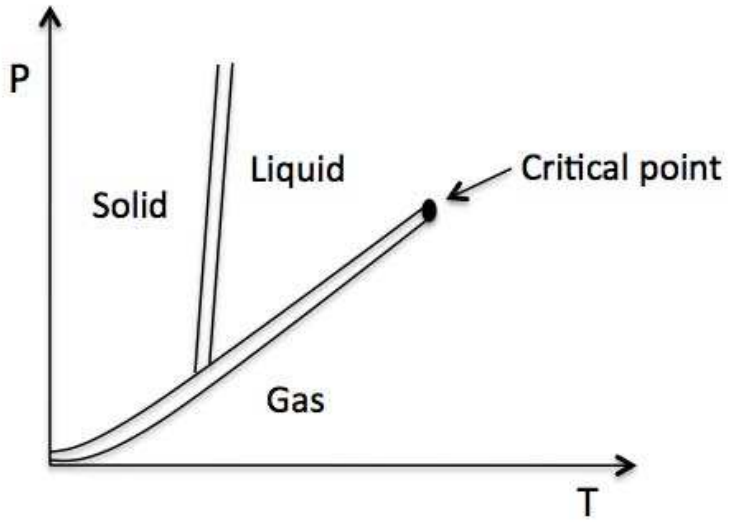

Figure 4.1: Phase diagram of a typical system (Argon for example) showing three phases in the P(pressure) - T(temperature) diagram. The lines show the regions that the free energy is singular, and therefore, the phase boundary. Although the liquid-solid phase boundary exist for all pressures and temperatures, the gas-liquid phase boundary terminates at the critical point.

From a more qualitative point of view, in continuous phase transitions, the state of the body changes continuously; however, the symmetry changes discontinuously at the transition point, i.e., there is a *spontaneous symmetry breaking* and at any instant we can assign the state of the system to one of the two phases. *At the transition point*, the states of the two phases are the same.

In contrast, in a first order phase transition, two different states stay in equilibrium, and coexist at the transition point. Because the state of the system changes discontinuously in a first order phase transition, the thermodynamic functions of the state of the system (entropy, energy, volume, pressure) also vary discontinuously at the transition point and therefore, in a first order phase transition latent heat is involved.

An example of a continuous phase transition would be the transition in symmetry of $BaTiO_3$, as the temperature varies [41]. At high temperature $BaTiO_3$ has a cubic lattice, with barium atoms in the vertices, the oxygen at the centres of the faces, and the titanium atoms at the centres of the cells. As the temperature decreases below the transition temperature, the titanium and oxygen atoms begin to move relative to the barium atoms parallel to an edge of the cube. As a result the symmetry of the lattice is affected and it becomes tetragonal instead of cubic. In this transition, no discontinuous change in the state of the body happens. The configuration of atoms changes continuously. However, an arbitrary small change in the atom's positions from their original sites, is sufficient to change the symmetry of the lattice.

Another example of the continuous phase transition is the magnetic transition that occurs in the Curie point (T_c) in ferromagnetic materials [12]. In this case a change in the symmetry of

the configuration of the magnetic moments happens and the mean magnetization of the system changes from zero in the paramagnetic phase ($T > T_c$) to a nonzero value in the ferromagnetic phase ($T < T_c$). This transition is schematically shown in Fig. 4.3.

For a continuous phase transition to be possible, it is necessary but not sufficient that the symmetry of one phase be higher than that of the other. But in the first order phase transition, the symmetries of the two phases may be unrelated, as the liquid-gas phase transition in which the two phases have the same symmetry [41].

To describe a phase transition, we can define a quantity η, called the *order parameter* in such a way that it takes non-zero values in the lower symmetry phase (the ordered phase) and zero in the higher symmetry phase (disordered phase) [41]. Passing through a continuous phase transition, the order parameter continuously changes to zero.

4.1 Continuous phase transition

The Landau theory of continuous phase transition is based on a description of the thermodynamic quantities in terms of deviations from the symmetrical state [41]. The thermodynamic potential of the body, f, is represented as a function of thermodynamic variables such as P, T and the order parameter, η.

Since η takes arbitrarily small values near the transition point, f also changes continuously, at the transition point [21]. To find the stable states, we need to solve $\frac{\partial f}{\partial \eta} = 0$ and find the η that minimizes f. From the definition of the order parameter, while for $T > T_c$, $\eta = 0$ must solve the minimum equation for f and for $T < T_c$, $\eta \neq 0$. Considering the neighbourhood of the transition point, $f(P, T, \eta)$ is expanded in powers of η:

$$f(P, T, \eta) = a_0 + a_1\eta + \eta^2 + a_3\eta^3 + a_4\eta^4 + ..., \tag{4.1}$$

where the coefficients a_0, a_1, a_2, a_3, a_4 are functions of P and T. This analytical Taylor series expansion of the thermodynamic potential near a phase transition is reasonable, as will be explained in sections 4.3 and 4.3.2.

For $T > T_c$, $\eta = 0$ and $a_0 = 0$ if f is defined as the free energy difference between two states. Moreover, f has to be consistent with the symmetries of the system. Considering the symmetry constraint, in a ferromagnetic system for example, the thermodynamic relation in the system must be invariant under the transformation $\eta \to -\eta$, since the properties of the material do not change if we rotate all of the spins by an arbitrary angle. Therefore, the coefficients of the odd power terms must be zero. The coefficient a_4 must be positive, otherwise the *free energy*, f, can be minimized by $|\eta| \to \infty$, which is not physical. This argument is correct if we expand the free energy up to the fourth order term. Higher order terms might be needed in the free energy to describe other phenomena, for example to describe a ferroelectric transition, an expansion to the sixth order term is needed and a different argument is required to determine the coefficients. For the purpose of this research the expansion up to the fourth order term is sufficient. Since the temperature dependence of f is not governed by a_4, it is sufficient to take it to be a positive constant. Therefore, for a continuous phase transition we have:

$$f(P, T, \eta) = a_2\eta^2 + a_4\eta^4 \tag{4.2}$$

a_2 is also expanded in temperature near T_c as

$$a_2 = a_2^0 + \frac{T - T_c}{T_c} a_2^1 + O((T - T_c)^2) \tag{4.3}$$

solving $\frac{\partial f}{\partial \eta} = 0$ to minimize the free energy, we find:

$$\eta = 0, \eta = \pm \sqrt{\frac{-a_2(T)}{2a_4}} \tag{4.4}$$

For η to be non-zero when $T < T_c$, a_2^0 must be zero. The higher order terms in Eq. 4.4 do not contribute to the leading behaviour near T_c and we have

$$a_2 = a_2^1 (\frac{T - T_c}{T_c}) \tag{4.5}$$

The free energy in Eq. 4.2, explaining the continuous phase transition, is plotted in Fig. 4.2. If $T > T_c$, the coefficient a_2 given by Eq. 4.5 is positive and the free energy has only one minimum at $\eta = 0$. On the other hand if $T < T_c$, the coefficient a_2 is negative and the free energy has two minima at $\eta = \pm\eta_1$.

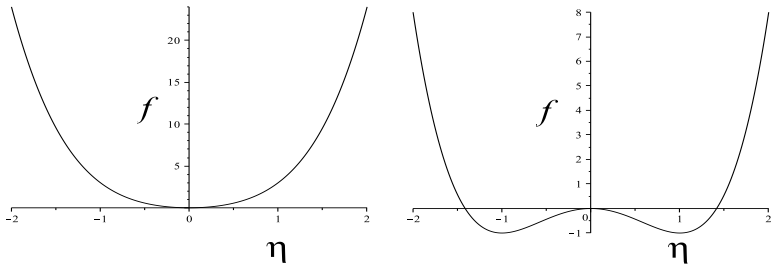

(a) $T > T_c$ (b) $T < T_c$

Figure 4.2: Plot of the free energy of Eq. 4.2 as a function of the order parameter η for (a) the symmetrical phase ($T > T_c$) for which $\eta = 0$ and (b) the unsymmetrical phase ($T < T_c$) for which $\eta \neq 0$.

For example in a ferromagnetic transition, shown schematically in Fig. 4.3, a reasonable choice for the order parameter would be the mean magnetization defined in Eq. 2.1. Above the Curie temperature, where the system is in the paramagnetic state, the mean magnetization of the system is zero and the system is in the symmetrical phase Fig. 4.2(a). When the temperature is decreased below the Curie temperature, the system undergoes a continuous phase transition to the ferromagnetic state, in which a net non-zero magnetization exists as seen in Fig. 4.2 (b).

4.2 Effect of an external field on the phase transition

We now consider how the properties of the continuous phase transition change when the body is subjected to an external field. It is important to consider this case in particular because it provides the basis for understanding the concept of hysteresis in ferromagnetic materials.

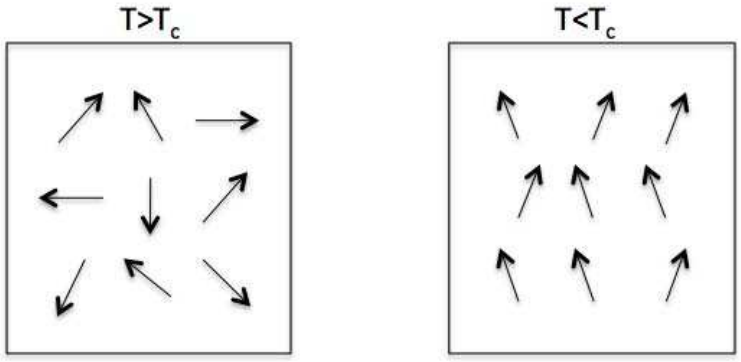

Figure 4.3: Paramagnetic to ferromagnetic phase transition, as the temperature is decreased below the Curie temperature. The mean magnetization is zero at the paramagnetic state, $T > T_c$, and nonzero at the ferromagnetic state, $T < T_c$.

Firstly, we need the Hamiltonian of the system. We know from thermodynamics that with each extensive variable, there is an associated generalized force such that the change in the internal energy [2] is the generalized force times the change in the extensive variable [12]. The extensive variable and its associated generalized force are called *conjugate variables*. Thus temperature and entropy, negative of the pressure and volume, and chemical potential and the number of particles in the system are conjugate variables.

Similarly, in a ferromagnetic system, the magnetic field and the order parameter $\eta = M$ are conjugate. Therefore, we may write the Hamiltonian of the body in terms of the conjugate variables η and the external field H as $-\eta HV$, where V is the volume of the body [41]. Therefore, we obtain the final expression for the Landau free energy:

$$f(P, T, \eta) = a_2\eta^2 + a_4\eta^4 - H\eta \tag{4.6}$$

A schematic plot of the free energy given by E.q.4.6 is shown in Fig. 4.4. The external magnetic field tilts the free energy and breaks the symmetry above and below the Curie temperature. Furthermore, in this case as Fig. 4.4(b) shows, a metastable phase, i.e., a local minimum could appear in the free energy which did not exist when $H = 0$.

4.3 Mean field approach

To understand how different forms of matter with different macroscopic properties emerge, we need to give a description of macroscopic properties based on the dynamics of microscopic degrees of freedom [35]. The macroscopic description usually involves a few thermodynamic variables such as pressure, volume, temperature, internal energy and entropy. In contrast,

[2] For example if the energy of a system (E) is a function of extensive variables entropy (S), volume (V) and particle number (N), then $dE = TdS - pdV + \mu dN$. Temperature (T), pressure (p) and chemical potential (μ) are referred to as generalized forces.

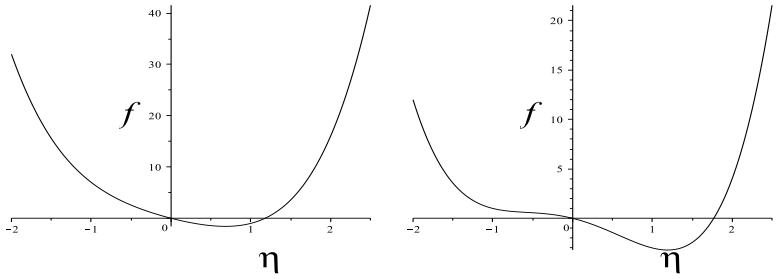

(a) $T > T_c$ (b) $T < T_c$

Figure 4.4: Schematic plot of the thermodynamic potential given by Eq. 4.6, for (a) $T > T_c$ and (a) $T < T_c$. In the presence of an external field, H, the free energy is tilted comparing to Fig 4.2, for which $H = 0$. Also local minima has appeared in the free energy, which do not exist when $H = 0$.

there are many microscopic degrees of freedom involved in a microscopic description of the system. These degrees of freedom which appear in the Hamiltonian of the system (H_Ω), are the positions and momenta of all of the particles or spins of all of the magnets and so on. Bridging between microscopic world and the macroscopic world based on the statistical mechanics laws (probabilistic connection between the two scopes) is very challenging in the thermodynamic limit ($N \to \infty$) due to the existence of many degrees of freedom and interactions between particles.

However, we could still study many macroscopic features of the material by *averaging* over sufficiently many degrees of freedom, to obtain a simpler description of the problem. The reason is that averaging and summing over many degrees of freedom, removes the complexities and singularities in the probabilistic description (in the same manner as the Central Limit Theorem does). This gives rise to a description of collective behaviour of the system at longer length and time scales. The averaged degrees of freedom are continuous and slowly varying *fields*. Therefore it is reasonable to expand the free energy f, as an analytical expansion of the fields.

As an example, in a ferromagnetic material, each atom has a magnetic moment. The probability distribution at the microscopic level might be complicated, since the moments might be constrained to have a fixed magnitude or have quantized specific values. At the coarse grained level, however, the magnetization field is obtained by averaging over many such magnetic moments and shows a smooth behaviour and has a rather simple probability distribution [35].

4.3.1 Correlation length

Because of the importance of the concept of correlation length in the discussions related to coarse graining, it is useful to take a look at its definition here.

Roughly speaking, the correlation length is a measure of the spatial extent of fluctuations in the order parameter about the average of the order parameter [21]. For example in a gas, there will be density fluctuations when the system is in thermal equilibrium. In a particular region of the gas, the density could be greater than the average density of the gas. These are droplet of near-liquid density, which are floating in the gas [21]. In thermal equilibrium, there

is a distribution of such droplet sizes, but there is a well-defined average size, at least away from the critical point. This characteristic size is, loosely speaking, the *correlation length*, ξ. The correlation length depends strongly on temperature near a continuous phase transition, and diverges to infinity at the transition point [21].

4.3.2 Coarse graining

The averaging process used to eliminate microscopic fast degrees of freedom, is called *coarse graining* [50]. Coarse graining close to a phase transition gives rise to a reasonable description of macroscopic properties of the system because the spatial correlations grow as $T \to T_c$, and the system contains regions having a uniform order parameter.

For simplicity we carry out the coarse graining calculations by focusing on a magnetic system, although the results are of more general applicability.

Close to a continuos phase transition only long wavelength collective excitations of spins are the important degrees of freedom. Therefore, it makes sense to focus on the statistical properties of these long wavelength fluctuations [35]. To do so, we change focus from microscopic length scales to mesoscopic length scales which are much larger than the lattice spacing but much smaller than the system size. The idea is schematically shown in Fig. 4.5.

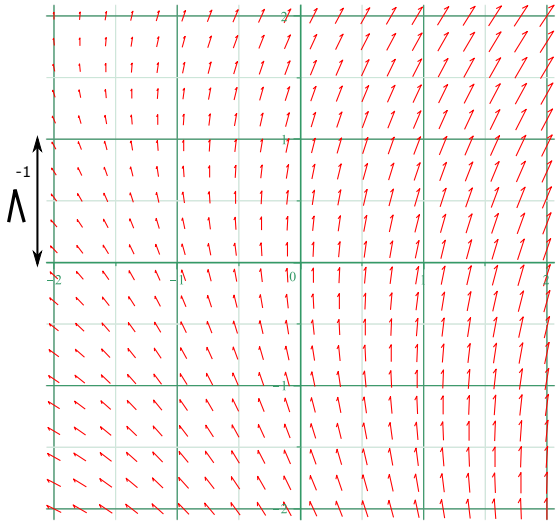

Figure 4.5: Schematic picture of showing the the idea of coarse graining in a magnetic system. Λ^{-1} is the length scale over which the magnetization is almost constant.

In the Ising model, close to a phase transition, the system contains blocks of spins of linear dimensions, in which the magnetization is approximately constant [21]. We divide the system into blocks of lengths smaller than the *correlation length*, $\xi(T)$ and define the local magnetization within each block centred at $\mathbf{r}$

$$M_\Lambda(\mathbf{r}) = \frac{1}{N_\Lambda(\mathbf{r})} \sum_{i \in \mathbf{r}} < S_i > \tag{4.7}$$

where is the number of spins in the block located at $\mathbf{r}$ and a is the lattice constant. In a d-dimensional system $N_\Lambda(\mathbf{r}) = (a/\Lambda)^d$ and Λ^{-1} is a length scale that satisfies

$$a \ll \Lambda^{-1} \leq \xi(T) \tag{4.8}$$

This definition for $M_\Lambda(\mathbf{r})$ is sensible for the condition given by Eq. 4.8 since as $T \to T_c, \xi \gg a$. Therefore by definition, the coarse grained magnetization $M_\Lambda(\mathbf{r})$ does not fluctuate sharply in the space, but varies smoothly.

4.4 First order phase transition

The main assumption in the Landau theory of phase transition is that the order parameter is arbitrarily small as $T \to T_c$. We saw in section 4.1 that a free energy of the form $at\eta^2 + b\eta^4$ describes a continuous phase transition, where $t = T - T_c$ is the reduced temperature. As discussed, the symmetry of the problem did not allow for a cubic term in η.

Now let us consider the effect of a cubic term [21]. If we have such a term, then:

$$f = at\eta^2 + C\eta^3 + \frac{1}{2}b\eta^4 \tag{4.9}$$

with a and b positive. Calculating the equilibrium value of η we obtain:

$$\eta = 0, \eta = -c \pm \sqrt{c^2 - at/b} \tag{4.10}$$

where $c \equiv 3C/4b$. The solution $\eta \neq 0$ is real only for reduced temperatures that satisfy

$$c^2 - \frac{at}{b} > 0 \tag{4.11}$$

or $t < t^* \equiv bc^2/a$. t^* is positive, so this occurs at a temperature greater than T_c. Plotting f, we obtain the forms shown in Fig. 4.6 for the free energy at different temperatures.

For $t < t^*$, a local minimum and a maximum exist in addition to the minimum at $\eta = 0$. If t is reduced further to t_1, then the value of f at the secondary minimum will become equal to the value at $\eta = 0$. For $t < t_1$, the secondary minimum becomes the global minimum, so the value of the equilibrium order parameter jumps *discontinuously* from $\eta = 0$ to a non-zero value. This is a *first order* phase transition.

In this chapter the static properties of the continuous and first-order phase transitions were discussed. In the next chapter we mainly focus on the dynamic properties of phase transitions. In particular we focus on the solidification process which is the process of transition from liquid phase to a crystalline solid phase.

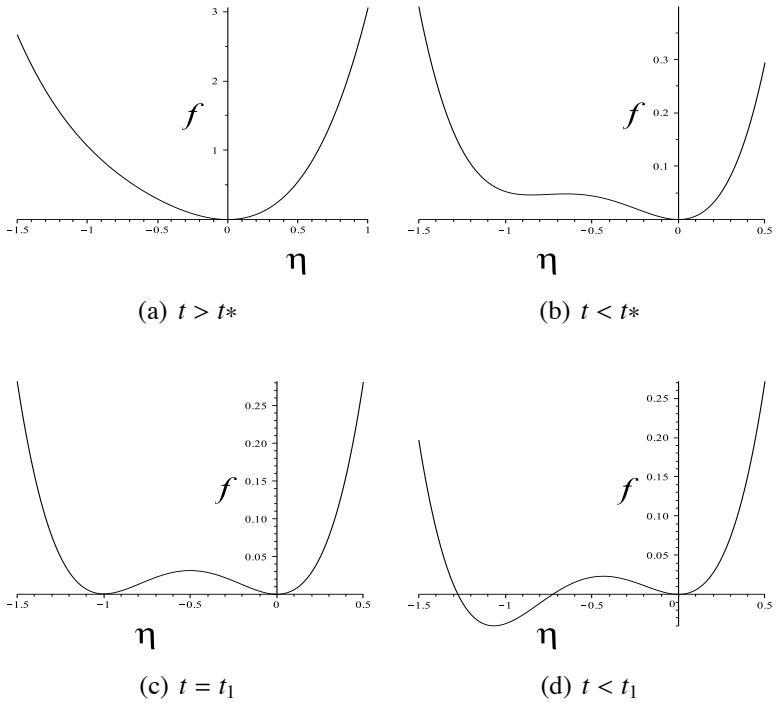

(a) $t > t*$ (b) $t < t*$

(c) $t = t_1$ (d) $t < t_1$

Figure 4.6: Plot of the free energy given by Eq. 4.9 as a function of the order parameter η, describing the first order phase transition. Here the existence of an odd term in the free energy causes appearance of a new minimum at $t < t^*$. Therefore, the two phases coexist at the transition point and the equilibrium order parameter changes discontinuously from zero at $t > t_1$ to a non-zero value at $t < t_1$.

Chapter 5

Phase Field Modeling

The LG formalism discussed in Chapter 4, only includes the equilibrium states of a system undergoing phase transition. In this chapter, the Phase Field modeling of microstructural pattern formation is reviewed. In this method the time evolution of the relevant order parameter is governed by a dissipative dynamics, driven by the LG free energy of the phase transition. Then in Chapter 6 we review the PFC method, which is an extension of the Phase Field method to produce crystalline structures.

Due to the importance of the process of solidification and dendritic pattern formation, different approaches have been applied to understand this process. Although the main idea of solidification is captured in the Stefan Problem, there are certain ambiguities in the description of solidification process with it. This comes from the fact that the regions separating the two phases in this model are treated as sharp interfaces, whose location is part of the unknown solution.

The moving interface is a source (or sink) of heat which once produced, should be diffused into the adjacent volume phases. Therefore, the interface needs to be tracked explicitly. Although such interface tracking approach can be successful in one-dimensional systems, it is not practical for complicated three-dimensional microstructures [7].

With progress in computational methods and facilities, Molecular Dynamics simulations also have been applied to understand the complex microstructures evolution in solidification process. The problem with MD and atomistic simulations is its efficiency. In MD approach the equations of motion for all atoms are solved. The growth patterns in solidification process exhibit characteristic length scales that lie in the 10-100 μm range [11]. In this length scale, the details of atomic motion do not enter and one can forget about the details of atomic organization and motion [47]. This allows efficient simulation over mesocopic time scales.

The phase field method is used to study non-equilibrium interface phenomena [1]. The basic idea in *phase field* model of solidification is to employ a *phase-field* variable which is a function of position and time, to describe whether the material is liquid or solid. Interfaces are described by smooth but highly localized changes of this variable between fixed values that represent solid and liquid. The dynamics of the field is governed by *Langevin equation*. This approach avoids the mathematically difficult problem of tracking the moving interface. The location of the interface is obtained from the numerical solution for the phase-field variable at positions where ϕ has a value between its bulk values. Therefore one does not need to track the interfaces explicitly. The interface emerge naturally as part of the solution of the dynamical

equations of motion. This model is a powerful method to study solidification process and is free from the disadvantages of the previous two methods.

5.1 Construction of free energy

The principle feature of the phase field model is the coarse-grained Landau-Ginzburg free energy. As described in section 4.3.2 the coarse graining process includes removing the microscopic degrees of freedom (such as individual spins in Fig. 4.5) by integrating them out, in such a way that mesoscopic degrees of freedom (spin blocks in Fig. 4.5) remain. This allows us to capture the information about mesoscopic time and length scales which are of interest in pattern formation processes. For a ferromagnetic system this process gives rise to the coarse grained Landau free energy $\mathcal{L}$, given by

$$\mathcal{L} = \int d^d\mathbf{r}\Big[\frac{1}{2}W_0\big(\nabla\mathbf{m}(\mathbf{r})\big)^2 + \frac{r(T)}{2}|\mathbf{m}(\mathbf{r})|^2 + \frac{u}{4}|\mathbf{m}(\mathbf{r})|^4\Big] \tag{5.1}$$

where $r(T) = a(T - T_c)$ and a is constant. When the temperature is above T_c, the coefficient, $r(T)$, is positive and the minimum of the free energy occurs at $|\mathbf{m}| = 0$. If the temperature is decreased below the Curie temperature, T_c, the coefficient $r(T)$ becomes negative. This causes the free energy to have two minima at nonzero magnetizations $|\mathbf{m}| = \pm\sqrt{-r(T)/u}$. This is the paramagnetic to ferromagnetic phase transition. The gradient term describes the free energy cost of spatial inhomogeneities and leads to surface tension between two phases.

The coefficient W_0 determines the domain wall width. We minimize the above free energy in one dimension with the assumption that $\mathbf{m} = (0, m)$ and require that $m(x \to +\infty) = |m_0|)$ and $m(x \to -\infty) = -|m_0|)$, where $|m_0| = \sqrt{|r|/u}$. We obtain the profile for the change in magnetization across the magnetic domain to be

$$m(x) = \sqrt{\frac{|r|}{u}}\tanh\Big(\frac{x}{2\xi_m}\Big) \tag{5.2}$$

where $\xi_m = \sqrt{W_0/2r}$ is the magnetic correlations length and gives a measure of the width of the domain wall. A plot of this profile is shown in Fig. 5.1. It is clear that if W_0 increases, the width of the domain wall also increases.

While the coarse graining procedure provides a connection between the microscopic and mesoscopic descriptions, it can only be accomplished for relatively simple systems [1]. In practice the general structure of the free energy could be determined by considering the physical properties of the system and its *symmetries*. In this approach the functional form of $\mathcal{L}$ is written as an expansion in powers of $\mathbf{m}$ and its gradients. The polynomial expansion gives the correct free energy form because the coarse graining (summing up the microscopic probability distributions) process simplifies the probability distribution and in most cases the Central Limit theorem could be used to justify that the probability distribution for the sumshould converge to a Gaussian form [35] and therefore a polynomial form for the free energy.

The gradient terms are needed when the system is not uniform, so that the order parameter depend on the position. This happens when the system is in an external potential or has internal

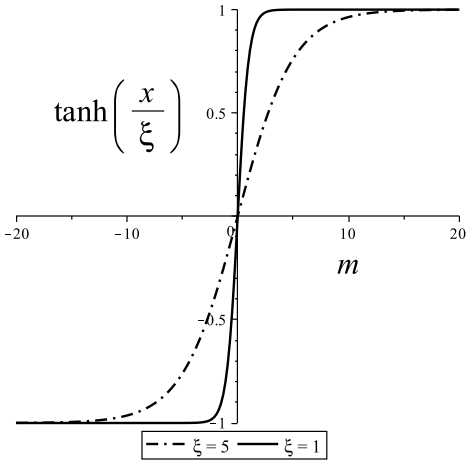

Figure 5.1: Schematic plot of the domain file profile between two domains with $m_0 = 1$ and $m_0 = -1$. The solid and dashed lines are obtained by plotting Eq. 5.2 with $\xi_m = 1$ and $\xi_m = 5$, respectively. It can be seen that the parameter W_0 determines the magnetic correlation length, ξ_m, and the domain wall width.

impurities. General interactions can be described by including many derivatives[1].

An underlying microscopic symmetry survives the averaging process and thus constrain the terms in expansions of the Hamiltonian. For example when there is no external field, all directions for the magnetization order parameter are similar and the hamiltonian should be symmetric under any rotation operator. A linear term in $\mathbf{m}$ is not allowed in such a system because it is not invariant under rotation.

For the gradient terms we should be careful about the spatial symmetries of the system. For example in an isotropic system i.e., a system that all directions in space are equivalent, we should use gradient terms that are invariant under spatial rotation, such as

$$(\nabla \mathbf{m})^2 \equiv \sum_{i=1}^{n} \sum_{\alpha=1}^{d} \partial_\alpha m_i \partial_\alpha m_i \tag{5.3}$$

in which ∂_α is the partial derivative in the α-th direction.

5.2 Dissipative dynamics

Brownian motion is the random jittery motion of a particle suspended in a fluid (Fig. 5.2). The random motion of a colloidal particle floating in a liquid medium is an example of a Brownian motion. This motion of the brownian particle is due to the random impacts of the much smaller fluid particles [35].

[1]This method is useful when a good description can be obtained by including only a few derivatives. This could be done for short-range interactions (including van der Waals interactions) but not long-range ones (such as Coulomb) [35].

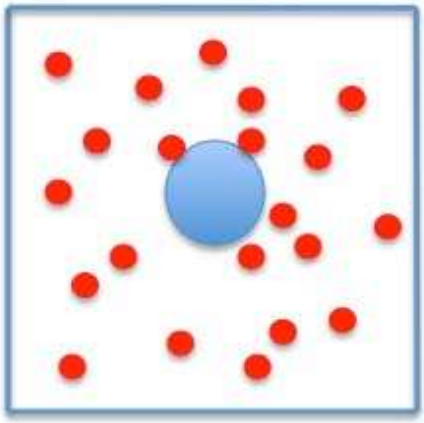

Figure 5.2: A Brownian particle suspended in a fluid. The fluid molecules which have smaller size relative to the Brownian particle, cause the random motion of the particle.

If the colloidal particle floating in a liquid medium is charged, it can be driven by an external electric field. Such a forced motion always suffers from a friction or a resistive force. It results from the impacts of molecules on the particle. Although the molecular collisions are random, a number of collisions produce a systematic result, force that is proportional to the velocity of the particle [40]. The displacement $\mathbf{r}(t)$ of such a brownian particle is given by

$$m\ddot{\mathbf{r}} = -\frac{\dot{\mathbf{r}}}{\mu} - \frac{\partial V}{\partial \mathbf{r}} + \mathbf{f}_{random}(t) \tag{5.4}$$

where m is the mass of the particle. On the right hand side of the equation above, there are three forces which are acting on the particle: The first term is a friction force due to the viscosity of the fluid, and μ is the mobility (the inverse of the friction constant). The second term is the force due to the external potential $V(\mathbf{r})$, for example electric field (if the particles are charged) and the third term is a random force of zero mean, which is due to the impacts of fluid particles. If the viscous term dominates the inertial force, i.e., an overdamped motion, we could ignore the acceleration term. Then the equation of motion would be

$$\dot{\mathbf{r}} = -\mu \partial V/\partial \mathbf{r} + \mu \mathbf{f}_{random}(t) \tag{5.5}$$

where $\mathbf{v}(\mathbf{r}) \equiv -\mu \partial V/\partial \mathbf{r}$ is the *deterministic velocity* and $\eta(t) \equiv \mu \mathbf{f}_{random}(t)$ is the *stochastic velocity*. Equation 5.5 could be written as

$$\dot{\mathbf{r}} = \mathbf{v}(\mathbf{r}) + \eta(t) \tag{5.6}$$

which is the *Langevin equation* [35].

For simplicity the probability distribution of the noise in velocity is assumed to be Gaussian with zero mean, and its different components at different times are assumed to be independent

$$< \eta(t) > = 0 \tag{5.7}$$
$$< \eta_\alpha(t)\eta_\beta(t') > = 2D\delta_{\alpha,\beta}\delta(t-t') \tag{5.8}$$

where D is related to the diffusion constant of particle in the fluid [35] and is related to the mobility by *Einstein relation*

$$D = k_B T \mu \tag{5.9}$$

where k_B is the Boltzmann constant and T is the temperature [15]. Einstein relation connecting the *fluctuations* of the noise to the *dissipation* in the medium, guarantees that the Langevin equation at long times reproduces the correct mean and variance for a particle in equilibrium at temperature T in the potential $V(\mathbf{r})$, i.e, the normalized Boltzmann probability distribution [35].

Random impacts of surrounding molecules cause two kinds of effect: 1) they act as a random driving force on the Brownian particle to maintain its incessant irregular motion. 2) they give rise to the frictional force for a forced motion. This means that frictional force and the random force must be related, because they come from the same origin. The Einstein relation, Eq. 5.9, connecting the deterministic and stochastic forces, is a manifestation of the *fluctuation-dissipation theorem* [40], which is a very general concept.

The Gaussian assumption for noise is quite reasonable since a Brownian particle has a mass much larger than the colliding fluid molecules and its motion is a result of a great number of successive collisions, which is a condition for the Central Limit theorem to work. This assumption also justifies the other assumption that the noise at different times are independent, since correlation between successive impacts remains only for the time of such molecular motion, which is short compared to the time scale of Brownian motion [40].

Langevin equations might be used for the systems in which the timescales of slow and fast dynamical variables are distinctly separated [51]. The fast variables enter the Langevin dynamics only in the form of a noise. It makes sense to apply such a dynamics to study the pattern formation, magnetic domain evolution and crystal growth in solidification process, since in such processes, there are two distinct sets of degrees of freedom: The slow variable are the mesoscopic length and time scales related to the interface motion and microstructures and the fast variable are the atomic motions and fluctuations that describe the random (thermal) effect of the environment that guarantees the relaxation to correct stationary equilibrium distribution (Boltzmann distribution) [1].

5.3 Dynamical equations of motion

We can generalize the Langevin formalism to a collection of degrees of freedom [35], described by a continuous field and construct a Langevin equation that governs the relaxational dynamics of a field, i.e., dissipative equations of motion. There are a set of models for evolution of a continuous field with time, which are referred to as *time-dependent Ginzburg-Landau* models and are classified based on whether the order parameter is conserved and whether it is coupled to any other relevant variable [30].

5.3.1 Model A

As an example of application of the Langevin dynamics to a continuous field, we consider the order parameter $\mathbf{m}$ in a magnetic system. Taking the functional derivative[2] of the potential energy, produces the deterministic force and therefore the deterministic velocity, i.e., the first term in the right hand side of Eq. 5.6. Analogues to this equation we can write

$$\frac{\partial m_i(\mathbf{r},t)}{\partial t} = -\mu \frac{\delta \mathcal{L}[\mathbf{m}]}{\delta m_i(\mathbf{r})} + \eta_i(\mathbf{r},t) \tag{5.10}$$

This equation is the simplest form of governing dynamics of the field, known as *Model A*, which describes the dynamics of a single non-conserved field such as magnetization in a magnetic phase transition [1]. From Eq. 5.1 the deterministic force could be calculated to give

$$F_i(\mathbf{r}) = -\frac{\delta \mathcal{L}[\mathbf{m}]}{\delta m_i(\mathbf{r})} = -r(T)m_i - u m_i|\mathbf{m}|^2 + W_0\nabla^2 m_i \tag{5.11}$$

which results in the dynamical equation of motion

$$\frac{\partial \mathbf{m}(\mathbf{r},t)}{\partial t} = -\mu r(T)\mathbf{m} - \mu u|\mathbf{m}|^2\mathbf{m} + \mu W_0\nabla^2\mathbf{m} + \eta(\mathbf{r},t) \tag{5.12}$$

with

$$< \eta_i(\mathbf{r},t) > \;=\; 0 \tag{5.13}$$

$$< \eta_i(\mathbf{r},t)\eta_j(\mathbf{r}',t') > \;=\; 2\mu k_B T \delta_{ij}\delta(\mathbf{r}-\mathbf{r}')\delta(t-t') \tag{5.14}$$

Figure 5.3.1 shows the coarsening process in a paramagnetic to ferromagnetic transition with magnetization in the z direction, i.e., $\mathbf{m} = (0, 0, m_z)$ in Eq. 5.1 and the system is quenched, so that the configuration that minimizes the free energy has a nonzero magnetization. The configurations show the order parameter m_z. The system has been initiated with magnetization fluctuations then it is allowed to relax to the configuration that minimize the free energy. Two different colours denote regions having positive and negative magnetizations. The "droplets" of negative magnetization grow in the regions of positive magnetization. The system will eventually be filled with one of the states, i.e., spin up or down, to minimize the free energy.

5.3.2 Model B

The equation of motion governing the dynamics of a conserved order parameter is called *Model B* or Cahn-Hilliard model [12]. Cahn and Hilliard derived a general equation for the free energy of a nonuniform system having a spatial variation in one of its intensive scalar properties such as composition or density [10]. As an example, this model could be used in a binary

[2]The functional derivative of a $F[f(x)]$ with respect to $f(x_0)$ is defined as [6]

$$\frac{\delta F[f]}{\delta f(x_0)} \equiv \lim_{\epsilon\to 0}\frac{F[f(x)+\epsilon\delta(x-x_0)] - F[f(x)]}{\epsilon}.$$

solution (A and B liquids) to describe the dynamics of the concentration (ϕ) of the A component, which is a conserved quantity if the system is closed, i.e., $\int \phi d^d\mathbf{r}$ is a conserved quantity since any concentration that is removed from one part of the system must appear in a neighbouring region. Therefore we need a dynamics that satisfy [35]

$$\frac{d}{dt}\int d^d\mathbf{r}\phi(\mathbf{r},t) = 0 \tag{5.15}$$

This is satisfied if the integrand is a total divergence. This occurs if we replace μ with $-D\nabla^2$ in Eqs. 5.10

$$\frac{\partial\phi(\mathbf{r},t)}{\partial t} = D\nabla^2\mu(\mathbf{r},t) + \eta(\mathbf{r},t) \tag{5.16}$$

where $\mu(\mathbf{r},t)$ is the "chemical potential"

$$\mu(\mathbf{r},t) = \frac{\delta F[\phi(\mathbf{r},t)]}{\delta\phi} \tag{5.17}$$

The noise should have a zero mean and a total divergence form. Replacing μ with $-D\nabla^2$ in Eq. 5.14, we obtain

$$< \eta(\mathbf{r},t)\eta(\mathbf{r}',t') >= -2Dk_BT\nabla^2\delta(\mathbf{r}-\mathbf{r}')\delta(t-t') \tag{5.18}$$

It could be observed that Eq. 5.16 guarantees that the current $\mathbf{j} = -D\nabla\mu(\mathbf{r},t)$ which is due to a difference in the chemical potential at different sites of the system be conserved, by following the local conservation law, i.e., $\partial_t = -\nabla\cdot\mathbf{j}$ [1].

5.4 Applications and limitations of the phase field method

Phase field methods are used to study situations in which the spatial patterns can be described by fields that are relatively uniform in space except near interfaces where a rapid change in the field occurs, e.g., order-disorder transitions in a binary solution or spinodal decomposition, where the field is concentration. The reason is the free energy that is exploited in this model, i.e., Eq. 5.1: the bulk free energy contain two wells to account for the two different phases (A-rich zones and B-rich zones in the binary solution example); the gradient term describes the fact that spatial gradients of field are unfavourable. This type of free energy always leads to a phase separation dynamics with a particular equation of motion for interfaces [17].

Many properties of matter, however, are controlled by elasticity and symmetry [16]. For example in the common phenomenon of crystal growth of a supercooled melt, initially small crystallites of arbitrary directions nucleate and grow until they contact each other and grain boundaries form. Further growth which will be dominated by motion of grain boundaries, will lead to a particular material structure that controls the material properties. As an other example, crystal symmetry can affect the final anisotropic shape of the a crystal grain [54].

To model such phenomena, the free energy must incorporate elasticity, dislocations, grain boundaries and crystals of arbitrary orientations. These features are quite difficult to be included in the traditional phase field models, with double well bulk free energy and the gradient term. As will be discussed in the next chapter, any free energy functional that is minimized by a

periodic field naturally includes the elastic energy and symmetry properties of the periodic field which are needed for a more realistic description of microstructure formation. Some generic features of periodic systems are that they naturally contain an elastic energy, are anisotropic, and have defects that are topologically identical to those found in crystals [16]. Incorporating the "periodic features" into phase field models leads to quite complicated continuum models [48] and this is a notable restriction of the phase field model.

5.5 Using phase field to study solidification of magnetic materials

Phase field model has been used to model microstructure evolution in magnetic materials [38], [39]. In their simulation, two order parameters are defined to describe the process: an order parameter which describes microstructure changes in paramagnetic states, $c_i(\mathbf{r}, t)$ and the phase field, $s_i(\mathbf{r}, t)$ with i indicating the number of components in the system.

The free energy in this model, contains various terms to account for elastic effects as well as the magnetic effects, i.e., $G_{tot} = G_c + E_{grad} + E_{str} + E_{mag}$ where G_c is the mean field chemical free energy, E_{grad} is the gradient energy induced by the spatial inhomogeneity of the order parameter, E_{str} is the elastic strain energy and E_{mag} is a magnetic energy that accounts for the magnetic domain morphology and the external magnetic field, which itself contains different terms: $E_{ext} + E_{exch} + E_{an} + E_{mstr} + E_d$. These terms describe effects of external magnetic field, exchange energy, magnetocrystalline anisotropy energy, magnetostriction energy and magnetostatic energy, respectively. This model is used to describe some of the effects observed in experiments related to microstructure changes under the effect of an external magnetic field in a few ferromagnetic alloys.

As mentioned in section 5.4, because of the form of the free energy that is employed in phase field models, it is unable to naturally capture the elastic effects and different terms ($E_{str}, E_{an}, E_{mstr}$ in the model described above) are needed to incorporate these effects into the formalism and this makes the model very complicated.

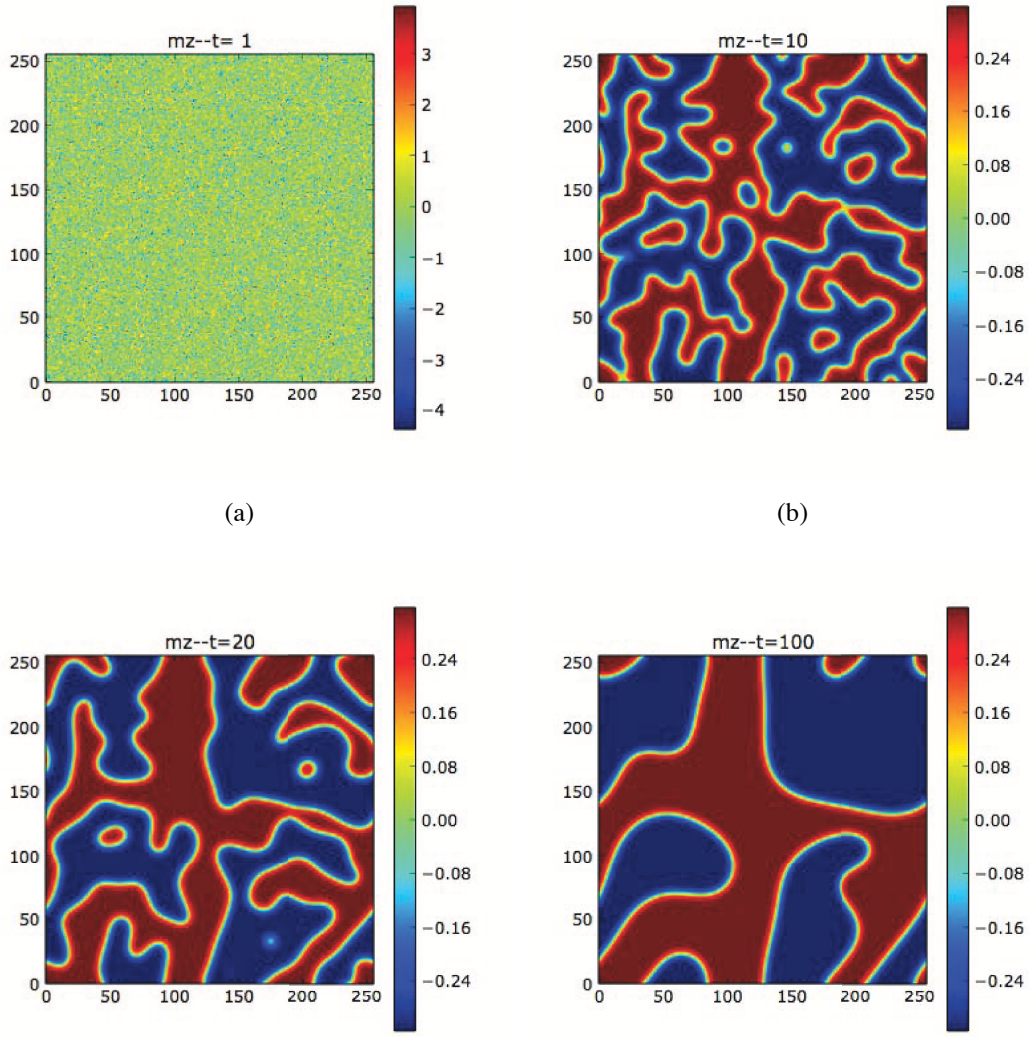

(a) (b)

(c) (d)

Figure 5.3: Model *A* simulation of a paramagnetic to ferromagnetic transition. The plot shows the phase field, the two colours denote the domains of spin up and down. The phase field is uniform inside the domains but has a rapid change at the boundaries between the regions. The simulations show coarsening of domains.

Chapter 6

Phase Field Crystal Modeling

The Phase Field Crystal (PFC) approach is an extension of the Phase Field modeling of microstrucure formation, in which the free energy is modified so that phases with spatial variations minimize the free energy. In this chapter we review the PFC free energy, its phase diagram and its elastic properties. This review helps us to understand the Magnetic PFC model introduced in Chapter 7, which is the original work in this thesis and is a novel method to study the magneto-elastic effects in ferromagnetic solids.

As discussed in the previous chapter, the MD approach to study solidification includes the integration of equations of motion for every single particle and as a result it automatically includes the elastic interactions, defects and crystalline symmetries. However, because it includes all of the atomic details, MD method is limited to very small length and time scales.

On the other hand continuum phase field theories can access longer length and time scales, namely, correlation length and diffusive time scales but as discussed in section 5.4 miss part of the relevant physics of processes involving atomic scale elastic and plastic properties. The reason is that the phase field models treat all solids equivalently, i.e., as a spatially uniform field. This eliminates many physical features, which are inherently due to the periodic nature of the crystalline solid such as elastic and plastic deformations, anisotropy and multiple orientations [19].

An extension to the phase field model, called the *phase field crystal* model, has relatively recently emerged to accomplish long-time simulation of materials at the microscopic length scales [16], [18]. This model is able to resolve microscopic structure [63]. In this approach the continuous field corresponding to a solid in equilibrium has a periodic structure and contains the symmetries that match those of the crystal structure of the material.

Figure 6.1 shows a typical configuration from a two dimensional phase field crystal simulation, modeling the growth of a crystalline phase in a supercooled liquid. It is a plot of the order parameter, i.e., the density field. The peaks in the density field denoting the atoms are analogous to those observed in electron diffraction experiments. Comparing the form of the field in phase field and phase field crystal, it is clear that unlike the phase field, the phase field crystal produces fields that are not uniform in the solid phase. In addition to the hexagonal symmetry of the peaks, differently orientated grains and grain boundaries between them are evident in this figure.

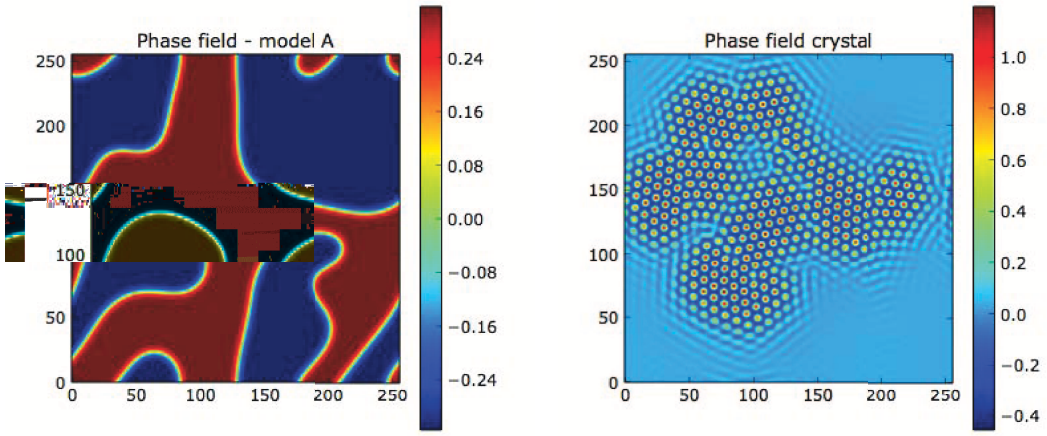

(a) (b)

Figure 6.1: Plot of the order parameter (density) for a phase field model simulation (a) and a phase field crystal simulation (b). The field in the phase field model is constant at two different phases, e.g., spin up and down regions in ferromagnetic transition. The field plot of the phase field crystal model shows a uniform field in the liquid phase and a periodic structure with a hexagonal symmetry in the solid phase. The simulations were performed by solving the model *A* dynamics for (a) and *PFC* conserved dynamics for (b), using the finite difference scheme.

6.1 Free energy

Periodic structures appear in many physical systems [16]. Examples include block copolymers [23], [8] , oil-water systems containing surfactants [45] and magnetic thin films [57]. To describe such systems, we need a free energy functional that incorporates the periodicity of the system. This free energy is different from the traditional phase field free energy in that it is minimized by periodic fields.

6.1.1 Minimal periodic free energy

To construct the free energy for periodic systems, we note that in periodic systems there is a specific length scale (or set of length scales) that characterizes the equilibrium state [54]. For example in a crystalline state the system is in equilibrium when all atoms lie on the points characterized by the unit cell. The dimensions of the unit cell define the characteristic length of the crystal. If the atoms are displaced from the points characterized by the unit cell, i.e., if the system is stretched or compressed, it will not be in equilibrium and its free energy will increase.

In periodic systems spatial periodic gradients are favourable. Therefore in a lowest order gradient expansion the coefficient of $|\nabla\phi|^2$ in the free energy has to be negative [16]. However, this term alone would result in infinite spatial gradients of ϕ and the next order term, compatible with the symmetries of the system must be included, i.e., $|\nabla^2\phi|$. Odd terms which result in the dependence of the free energy on the direction of the gradients are not included in the gradient

expansions of this model. The polynomial expansion in ϕ is also needed to serve as the bulk free energy, with two wells, to make the phase transition between the liquid and crystalline phase possible. The generic free energy functional for periodic structures can be written as [16]

$$\mathcal{F} = \int dV\Big(\frac{K}{\pi^2}\Big[-|\nabla\phi|^2 + \frac{a_0^2}{8\pi^2}|\nabla^2\phi|^2\Big]\Big) + f_{bulk}(\phi) \tag{6.1}$$

where K and a_0 are phenomenological constants and a_0 determines the equilibrium length scale. Inserting a one dimensional periodic solution for ϕ of the form of $\phi = Asin(2\phi x/a)$ into the free energy we obtain

$$\frac{\mathcal{F}}{a} = KA^2\Big[-\frac{2}{a^2} + \frac{a_0^2}{a^4}\Big] + \frac{1}{a}\int dV f_{bulk}(\phi) \tag{6.2}$$

which is the free energy per unit length. If the system is displaced from its equilibrium state a_0, by Δa the free energy will be

$$\frac{\mathcal{F}}{a} = KA^2\Big[-\frac{2}{(a_0+\Delta a)^2} + \frac{a_0^2}{(a_0+\Delta a)^4}\Big] + \frac{1}{a}\int dV f_{bulk}(\phi) \tag{6.3}$$

which is obtained by inserting $a = a_0 + \Delta a$. Assuming the displacement Δa is small enough, we expand the free energy about the equilibrium length scale a_0

$$\frac{\mathcal{F}}{a} \approx -\frac{KA^2}{a_0^2} + \frac{4KA^2}{a_0^4}(\Delta a)^2 + \frac{1}{a}\int dV f_{bulk}(\phi) \tag{6.4}$$

Although this is a very simplified situation, it shows that the energy can be written in the form of the Hooke's law, i.e., $E = E(a_0) + k(\Delta a)^2$, which is a characteristic of elastic phenomena. A generic feature of periodic systems is therefore that for small perturbations from the stationary state, they show elastic behaviour.

6.1.2 Classical density functional theory of freezing

As mentioned before the phase field crystal (PFC) method was developed [16] to model crystal growth, including elasticity, dislocations, different crystal orientations and anisotropy. The phase field crystal free energy functional was originally introduced in [16], using phenomenological arguments given in the previous section. Then it was further developed using classical density functional theory of freezing [55]. The CDFT of freezing was used to derive the original phase field crystal model [19]. This derivation clarified the relationship between the phenomenological parameters of the original PFC free energy and physical properties of the material such as the liquid phase isothermal compressibility and the bulk modulus of the crystal and the lattice constant [19].

In this theory the free energy functional $\mathcal{F}[\rho]$ is a functional of the local density $\rho(\mathbf{r})$ of atoms in the system. For an *ideal*, non-interacting, gas the free energy could be calculated exactly to give [32]

$$\frac{\mathcal{F}_{id} - \mathcal{F}_{id}(\rho_0)}{k_B T} = \int d\mathbf{r}\Big[\rho(\mathbf{r})ln\Big(\frac{\rho(\mathbf{r})}{\rho_0}\Big) - \delta\rho(\mathbf{r})\Big] \tag{6.5}$$

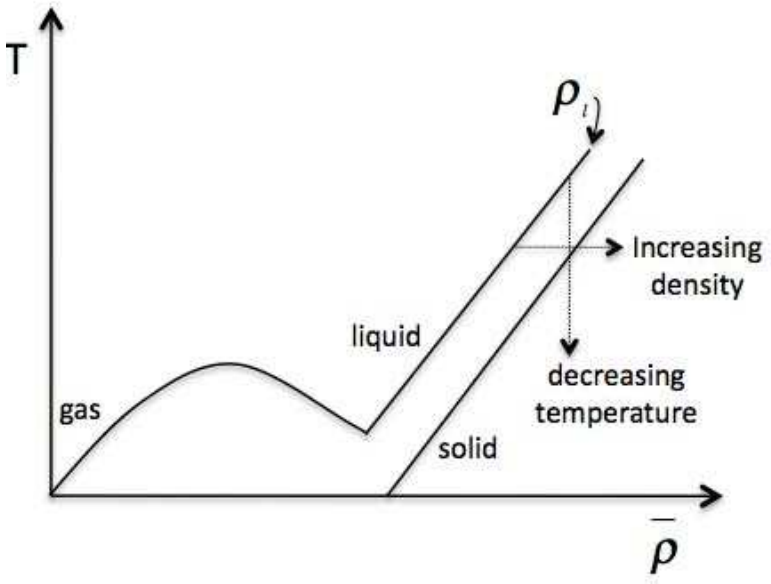

Figure 6.2: The typical temperature-density phase diagram of a pure material. The free energy in the CDFT method is expanded about a liquid state on the liquidus line.

where $\delta\rho(\mathbf{r}) = \rho(\mathbf{r}) - \rho_0$. To calculate the the total free energy, i.e., $\mathcal{F} = \mathcal{F}_{id} + \mathcal{F}_{in}$ we also need the contribution from the *interactions* between particles, $\mathcal{F}_{in}$. This contribution is approximated by expanding $\mathcal{F}$ in terms of the n-point direct correlation functions, C_n, defined as

$$C_n(\mathbf{r}_1, \mathbf{r}_2, ...) \equiv \frac{\delta^n \mathcal{F}_{in}}{\prod_{i=1}^{i=n} \delta\rho(\mathbf{r}_i)} \tag{6.6}$$

where $\mathcal{F}_{in}$ is the contribution to the total free energy functional $\mathcal{F}$ from the interactions between particles. For example $C_2(\mathbf{r}_1, \mathbf{r}_2)$ describes the probability that if an atom exists at point $\mathbf{r}_1$, another atom also exists at point $\mathbf{r}_2$.

Expanding to second order about a uniform reference density ρ_0, the total $\mathcal{F}$, is calculated by adding the ideal gas free energy and the nonlocal free energy corresponding to the interactions between particles

$$\frac{\mathcal{F} - \mathcal{F}(\rho_0)}{k_B T} = \int d\mathbf{r}\Big[\rho(\mathbf{r}) ln\Big(\frac{\rho(\mathbf{r})}{\rho_0}\Big) - \delta\rho(\mathbf{r})\Big] - \frac{1}{2}\int\int d\mathbf{r}_1 d\mathbf{r}_2 \delta\rho(\mathbf{r}_1) C_2(\mathbf{r}_1, \mathbf{r}_2) \delta\rho(\mathbf{r}_2) \tag{6.7}$$

where ρ_0, corresponds to a liquid state on the liquidus line of the solid-liquid coexistence region in the temperature-density phase diagram of a pure material, sketched in Fig. 6.2. This expansion is only valid if $\delta\rho(\mathbf{r})$ is small which certainly is not the case in the solid phase, yet even at this level of approximation the CDTF is able to describe the emergence of a solid phase in the liquid-solid phase transition.

6.1.3 Phase field crystal model

To derive the PFC free energy from the CDFT, we define the dimensionless number density field

$$n \equiv \frac{(\rho - \rho_0)}{\rho_0} \tag{6.8}$$

Then we insert it into the CDFT free energy, Eq. 6.7, and make two approximations: 1) The local portion of the free energy, i.e., the free energy of the ideal gas is expanded to the fourth-order

$$(1+n)ln(1+n) - n = \frac{1}{2}n^2 - \frac{1}{6}n^3 + \frac{1}{12}n^4 \tag{6.9}$$

2) We simplify the calculations by expanding the nonlocal portion of the free energy in terms of gradients of the density. This can be guided by expanding the two point correlation function in a Taylor series in Fourier space. To the fourth order

$$\hat{C}(k) \approx \hat{C}_0 + \hat{C}_2 k^2 + \hat{C}_4 k^4 \tag{6.10}$$

where the subscript "2", referring to the two point correlation function, has been dropped from the term $\hat{C}(k)$. This approximation is relevant assuming that n varies slowly compared with the range of the two-point correlation function, C_2. It is the lowest order expansion to capture the periodic features of the crystalline phase. A sketch of $\hat{C}(k)$ for a typical liquid is shown in Fig 6.3.

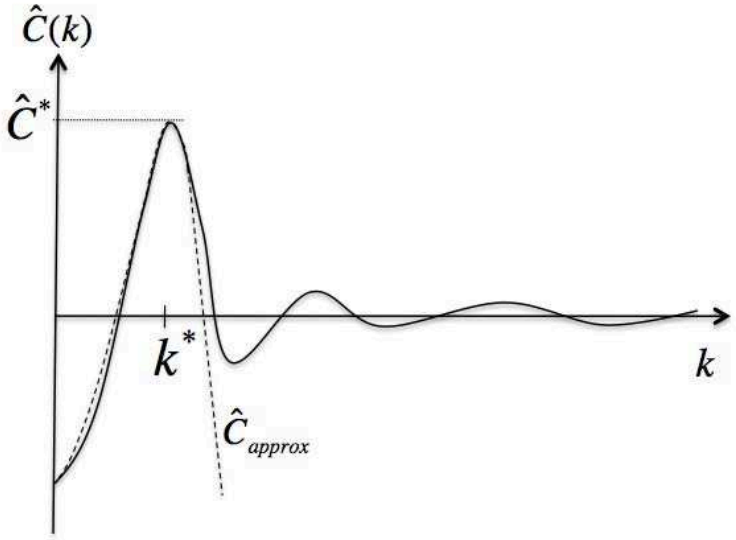

Figure 6.3: Schematic plot of a two point correlation function for an isotropic liquid in Fourier space. The dashed line denotes the approximation to k^4 order. The parameters $\hat{C}_0$, $\hat{C}_1$ and $\hat{C}_2$ are chosen so that the the $\hat{C}$ expansion fits the main peak of the two-point correlation curve.

In real space the expansion in Eq. 6.10 corresponds to $C = (\hat{C}_0 - \hat{C}_2\nabla^2 + \hat{C}_4\nabla^4)\delta(\mathbf{r}_1 - \mathbf{r}_2)$. The parameters $\hat{C}_0$, $\hat{C}_2$ and $\hat{C}_4$ should be chosen in such a way that they fit the first peak in $\hat{C}$. To be able to fit they should be negative, positive and negative, respectively. These variables are related to three basic properties of the material, the liquid isothermal compressibility ($B_l \sim (1 - \rho_0\hat{C}_0)$), the bulk modulus of the crystal ($B_x \sim \bar{\rho}_0 C_2^2/|\hat{C}_4|$) and lattice constant ($R \sim (\hat{C}_2/|\hat{C}_4|)^{1/2}$) [19]. With these simplifications we obtain

$$\frac{\Delta\mathcal{F}}{k_B T V \rho_0} \approx \frac{1}{V}\int d\mathbf{r}\left[\frac{B_l}{2}n^2 + \frac{B_x}{2}n(2R^2\nabla^2 + R^4\nabla^4)n - t\frac{n^3}{3} + v\frac{n^4}{4}\right] \tag{6.11}$$

where formally $t = 1/2$, $v = 1/3$ and $V = \int d\mathbf{r}$. The relevant length scale of the model is given by R which determines the lattice constant of the crystal phase. The only length scale R appearing in this equation can be rescaled and taken out of the integral. Therefore we obtain the *PFC free energy functional* as

$$\frac{\Delta\mathcal{F}}{k_B T V \rho_0} \approx \frac{R^d}{V}\int d\mathbf{x}\left[\frac{n}{2}(\Delta B + B_x(1 + \nabla^2)^2)n - t\frac{n^3}{3} + v\frac{n^4}{4}\right] \tag{6.12}$$

where $\mathbf{x} \equiv \mathbf{r}/R$ and $\Delta B \equiv B_l - B_x$. With this rescaling, the free energy contains only two parameters, B_l and B_x.

In this model, the transition from liquid to solid occurs when ΔB changes sign which means that ΔB is related to *temperature*. To see this, we use the definitions of B_l and B_x

$$\Delta B = B_l - B_x = (1 + \rho_0\hat{C}_0) - (\rho_0\hat{C}_2^2/4\hat{C}_4) = 1 + \rho_0(\hat{C}_0 - \hat{C}_2^2/4\hat{C}_4) \tag{6.13}$$

Noting that the first peak of $\hat{C}$ occurs at $k^* = (\hat{C}_2/2\hat{C}_4)^{1/2}$ with $\hat{C}^* = -\hat{C}_0 + \hat{C}_2^2/4\hat{C}_4$, we obtain

$$\Delta B = 1 - \rho_0\hat{C}^* \tag{6.14}$$

From this equation it is apparent that as $\hat{C}^*$, the nearest neighbour correlation increases (the emergence of crystalline structure), ΔB decreases. Furthermore, as the average number density of the system ρ_0 increases, ΔB decreases and a transition to the crystalline state occurs. Therefore decreasing ΔB is equivalent to decreasing temperature or increasing the average density, as illustrated in Fig. 6.2.

6.1.4 Dynamics

The dynamics of the field in the PFC model is taken to be conserved

$$\frac{\partial\phi(\mathbf{r},t)}{\partial t} = D\nabla^2\frac{\delta F[\phi(\mathbf{r},t)]}{\delta\phi} + \eta(\mathbf{r},t) \tag{6.15}$$

With the noise having a zero mean and a total divergence form

$$< \eta(\mathbf{r},t)\eta(\mathbf{r}',t') >= -2Dk_B T\nabla^2\delta(\mathbf{r} - \mathbf{r}')\delta(t - t') \tag{6.16}$$

Conserved dynamics is needed to model the crystal growth since the PFC model tracks the evolution of density. For example a defect such as an extra row of atoms in a cryatal can not simply disappear, they must remove diffusively.

6.2 Equilibrium states and phase diagram in two dimensions

It is possible to analytically calculate the equilibrium states of the PFC free energy to the lowest order, i.e., the states that minimize the free energy, by expanding the number density of the crystalline state in Fourier series using a one-mode approximation. The free energy is then minimized with respect to the parameters of this simplified expansion. Possible coexistence regions of the phase diagram are calculated using the double tangent construction.

In two dimensions the PFC free energy is minimized by three different states. These states are formulated by periodic functions of the density field n. A constant density state or liquid phase, the stripe phase which is represented by a one dimensional periodic function and the hexagonal phase which is presented by a two dimensional periodic function are the three states that minimize the PFC free energy [16].

Here we only present the calculation of the liquid-hexagonal coexistence line in the PFC phase diagram. The procedure is basically the same for the hexagonal-stripe phase. One only needs to start with a different expansion for the density of the stripe phase.

To calculate the liquid-hexagonal coexistence line we expand the number density of the crystalline phase around n_0, the density along the liquid coexistence line, i.e.,

$$n = n_0 + \sum_{\mathbf{G}} \eta_{\mathbf{G}} e^{i\mathbf{G}\cdot\mathbf{r}} + C.C \tag{6.17}$$

where $C.C$ is the complex conjugate, $\mathbf{G} \equiv n_1\mathbf{q}_1 + n_2\mathbf{q}_2$ and the vectors $\mathbf{q}_1$ and $\mathbf{q}_2$ are the primitive vectors[1] of the reciprocal lattice[2] describing a specific crystalline symmetry. The points in the reciprocal lattice are mapped by $\mathbf{G}$. The coefficients $\eta_{\mathbf{G}}$ represent the amplitude of a given reciprocal lattice vector, or the X-ray scattering amplitude.

For a triangular two dimensional lattice the primitive reciprocal lattice vectors are

$$\mathbf{q}_1 = -\frac{2\pi}{a}\left(\frac{\sqrt{3}}{2}\hat{x} + \frac{1}{2}\hat{y}\right) \tag{6.18}$$

$$\mathbf{q}_2 = \frac{2\pi}{a}\hat{y} \tag{6.19}$$

where a is the lattice constant. A one-mode approximation, i.e, expansion to the lowest order harmonics, is made to evaluate the phase diagram [16]. In this approximation we assume that the amplitudes of the density expansion η_j are real and equal to a constant value, ϕ, for all of the $\mathbf{G}$ vectors. In two dimensions, a one-mode approximation corresponds to retaining all Fourier components that have the same length. More precisely the lowest order harmonics consist of all (n_1, n_2) pairs such that the vector $\mathbf{G}$ has length $2\pi/a$. This set of vectors includes $(n_1, n_2) = (1, 0), (0, 1)$ and $(-1, -1)$. The lowest order set thus leads to

[1] The lattice is defined by three fundamental translation vectors $\mathbf{a}_1, \mathbf{a}_2, \mathbf{a}_3$ such that the atomic arrangement looks the same in every respect when viewed from the point $\mathbf{r}' = \mathbf{r} + n_1\mathbf{a}_1 + n_2\mathbf{a}_2 + n_3\mathbf{a}_3$, where n_1, n_2, n_3 are arbitrary integers. The primitive translation vectors form the smallest cell that serve as the building block for the crystal structure [37].

[2] The reciprocal lattice points represent the allowed modes in the Fourier series expansion of the number density $n(\mathbf{r})$. A term is allowed if it is consistent with the periodicity of the crystal and its symmetry. It can be shown that a diffraction pattern of a crystal obtained from an X-ray scattering experiment is a map of the reciprocal lattice of the crystal [37].

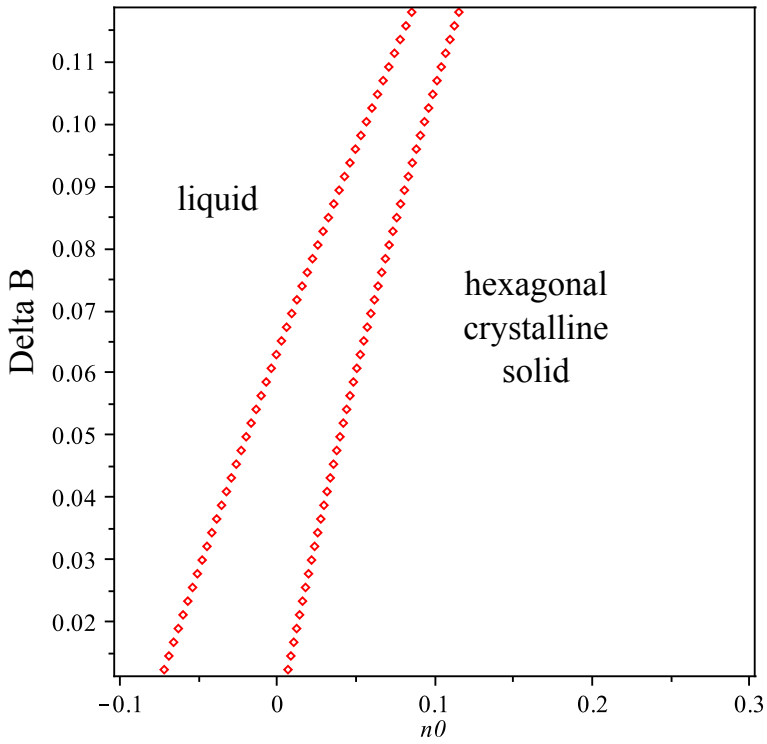

Figure 6.4: The portion of the PFC phase diagram that contains the liquid and solid equilibrium phases and the liquid-solid coexistence lines. It should be mentioned that the stripe phases can also minimize the PFC free energy, Eq. 6.12, however the stripe phase appears at higher densities that is not shown in this plot. This sample phase diagram is calculated with $t = 1/2, v = 1/3$ and $B_x = 98/100$ in the PFC free energy.

$$n = n_0 + \phi(\frac{1}{2}cos(\frac{2q}{\sqrt{3}}y) - cos(qx)cos(\frac{q}{\sqrt{3}}y)) \tag{6.20}$$

where $q = (2\pi/a)(\sqrt{3}/2)$. Substituting this expansion into the free energy and minimizing with respect to q gives $q_{eq} = \sqrt{3}/2$ and

$$F(q_{eq}, \phi, n_0) = \frac{B_l}{2}n_0^2 - t\frac{n_0^3}{3} + v\frac{n_0^4}{4} + \frac{3}{16}[\Delta B - n_0(2t - 3vn_0)]\phi^2 - \frac{1}{16}[t - 3vn_0]\phi^3 + \frac{45v}{512}\phi^4 \tag{6.21}$$

Minimizing this free energy with respect to the amplitude, ϕ, we arrive at

$$\phi_{tri} = \frac{4}{15v}(t - 3vn_0 + \sqrt{t^2 - 15v\Delta B + 12n_0v(2t - 3vn_0)}) \tag{6.22}$$

and, obviously, $\phi_{liq} = 0$ for liquid. We can now calculate the coexistence lines knowing the free energy of the solid and liquid phases, and applying the common tangent formulation given by Eqs. 3.9 and 3.10. Solving the set of equations at different temperatures, we obtain the liquid-hexagonal coexistence line in the PFC phase diagram as shown in Fig. 6.4. The details of the common tangent construction are given in [19].

6.3 Amplitude expansion and elastic deformations

In the PFC model explained above, the number density field is expanded (Eq. 6.17) in terms of the amplitudes of the periodic structure, that are assumed to be constant. Much more information can be retained if the amplitudes are allowed to vary [54]. This is the basic idea of the *amplitude expansion method* and as we will see, it allows us to model local elastic deformations in the lattice that result in long range elastic effects associated with dislocations. As an example a liquid-solid interface can be described by smoothly varying the amplitude from a finite value in the solid phase to zero in the liquid (Fig. 6.5). Dislocations can also be modeled by a rapid change in the amplitude.

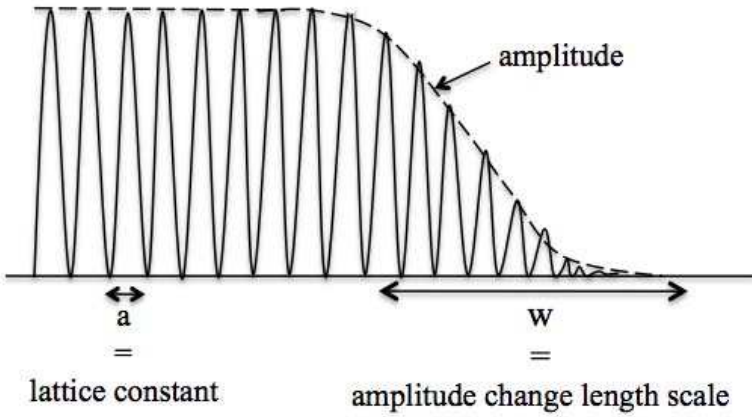

Figure 6.5: The basic idea of the amplitude expansion method. This plot schematically shows how the amplitude of the Fourier expansion of the density field, Eq. 6.23 changes smoothly from a finite value in the crystalline phase to zero in the liquid phase. The smooth change in the amplitude represents the solid-liquid interface

Expanding the number density in terms of the Fourier modes

$$n = n_0 + \sum_j \left(\eta_j \exp\left(i\mathbf{G}_j \cdot \mathbf{r} \right) + \eta_j^* \exp\left(-i\mathbf{G}_j \cdot \mathbf{r} \right) \right) \tag{6.23}$$

where η_j is a complex variable that is assumed to vary on length scales that are much larger than the density field. Therefore we can define two distinct length scales in the system: the lattice spacing a and the length scale of the change from liquid to solid w or the size of the dislocation, $a << w$.

Although by this assumption we loose a bit of the physics of the system, we can still capture the essential physics of crystallization and elasticity. As shown in Appendix B, this assumption simplifies the calculation of the free energy significantly. With this assumption we can integrate over the unit cell by assuming that the amplitudes η_j are constant which is a significant simplification in calculation of the integrals involved.

The equations of motion for the amplitudes are calculated in [54] for the PFC model. In the next chapter we calculate the free energy in terms of the amplitudes for the Magnetic PFC

model. Here we only give a general picture of the method and how this method gives us more information about the elastic properties of the material.

The elasticity can be described using the displacement field. If we have a perfect lattice, then the arrays of the atoms are located at the equilibrium positions, that are a lattice constant distance apart. Atoms can move from their equilibrium position if the system is under strain, as shown in Fig. 6.6. Each atom can have a different displacement depending on its position. We can describe the displacement of the atoms, using the displacement field $u(\mathbf{r})$ which is a function of the position of the atom in the lattice, $\mathbf{r}$.

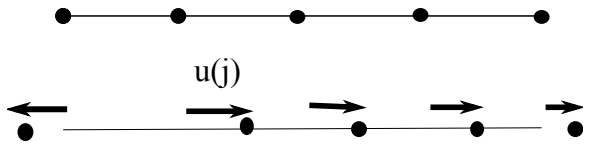

Figure 6.6: Schematic plot of the displacement of the particles from their equilibrium lattice positions (the grey points), being a distance of a apart. The displacement of the j-th particle in the lattice is represented by u_j in the figure.

We expect the energy to depend on the spatial gradients of the displacement field since if all the atoms are displaced by the same mount, nothing has really happened in the crystal except the displacement of the whole crystal.

If there are some deformations, then the density field expansion in Eq. 6.23 will be $\eta_j e^{i\mathbf{G}_j\cdot\mathbf{r}} \rightarrow \eta_j e^{i\mathbf{G}_j\cdot(\mathbf{r}+\mathbf{u})}$. We can express this as a change in the amplitudes, i.e., $\eta_j \rightarrow \eta_j e^{i\mathbf{G}_j\cdot\mathbf{u}}$. Therefore to incorporate elastic deformations into the equations, we let $\eta_j = \phi e^{i\mathbf{G}_j\cdot\mathbf{u}}$. The calculations have been performed in [54] for the PFC free energy and the free energy is written in terms of the strain tensor elements which are based on the derivatives of $\mathbf{u}$. Writing the free energy this way, the elastic constants of the material can be directly read from the free energy.

In the next chapter we present a new model called the Magnetic Phase-Field Crystal model to study the magneto-elsatic effects in ferromagnetic materials. We use the amplitude expansion method to calculate the free energy of a ferromagnetic material in terms of the strain tensor elements and the magnetic parameters of the metarial, i.e., saturation magnetization magnetic susceptibility and the coefficient of magnetostriction.

Chapter 7

Magnetic Phase Field Crystal Model

In this chapter, the Magnetic Phase Field Crystal (Magnetic PFC) model is presented. It is a novel approach we proposed, to study the inter-relation between morphological structure and magnetic properties of ferromagnetic solids and is based on the PFC formalism of grain growth and solidification. In this chapter the free energy of this model is introduced and a description of the different terms of the free energy and the phenomenological parameters. This chapter, together with Chapters 8, 9 and Appendices A and B covers the original production of our studies to understand the inter-relation between morphological structure and magnetic properties of ferromagnetic solids.

The calculations presented in this chapter and Chapter 8 show that the model comprise first order liquid-solid transition, ferromagnetic transition and Curie temperature, elastic effects and magnetocstriction effect. The anisotropic magnetostriction effect is consistent with the symmetry of the crystalline structure and if the crystal forms in another direction the anisotropy effect exactly follows and the crystal structure selects the preferred directions for magnetization.

Similar to the other field theoretical approaches, the Magnetic PFC free energy is a phenomenological free energy and the parameters of the free energy need to be estimated. By averaging over the microscopic degrees of freedom and replacing the microscopic Hamiltonian with a coarse-grained one, we simplified the calculations but the price to pay is to find the connection between the phenomenological parameters appeared in the free energy and measurable quantities.

In Sections 7.1 and 7.2, the free energy of the Magnetic PFC model is introduced, the physical significance of each term of the free energy is explained and the dynamical equations of the motion are discussed. Also we estimate the values of some of the phenomenological parameters involved in the free energy, by examining the effects arising from the different terms and comparing the effects with real systems. For example the value of the permeability, μ_0, in the units of the model, is estimated using the fact that the molecular field inside the ferromagnetic material is mostly due to the exchange interaction rather than the classical dipole-dipole interaction. Knowing the relative significance of these two fields in real materials, we can estimate the value of μ_0.

In Section 7.3 the free energy of the magnetic field inside the material is calculated.

In Section 7.4 we estimated the values of the magnetic phenomenological parameters by connecting them to physical macroscopic quantities such as saturation magnetization and magnetic susceptibiliy.

7.1 Free energy

To incorporate elastic and magnetic properties of ferromagnetic crystalline solids, the free energy is written in terms of the two relevant order parameters: dimensionless density n and magnetization vector, $\mathbf{m} = (m_x, m_y)$.

The free energy we propose is

$$\begin{aligned}\frac{\Delta F}{k_B T V \bar{\rho}} \approx \int d\mathbf{r}\Bigg(\Bigg[n\left(\Delta B + B_s\left(1+\nabla^2\right)^2\right)\frac{n}{2} - t\frac{n^3}{3} + v\frac{n^4}{4}\Bigg] - \frac{\alpha}{2}\left(\mathbf{m}\cdot\nabla n\right)^2 \\ + \left[\frac{W_0^2}{2}\left|\nabla\mathbf{m}\right|^2 + (r_c - \beta n^2)\frac{|\mathbf{m}|^2}{2} + \gamma\frac{|\mathbf{m}|^4}{4}\right] - \mathbf{m}\cdot\mathbf{B} + \frac{|\mathbf{B}|^2}{2\mu_0}\Bigg),\end{aligned} \tag{7.1}$$

where the first square brackets enclose the common phase field crystal free energy, which was introduced in Eq. 6.12. We refer to this part of the free energy density (the integrand) as f_{pfc}. The field $n = (\rho - \bar{\rho}_l)/\rho$ is the dimensionless number density, in which $\bar{\rho}_l$ is a constant density and is defined to be the density of liquid at coexistence. As discussed in Section 6.1.3, the quantity $\Delta B = B_l - B_s$ is related to the temperature. It decreases when the temperature decreases. The parameters t and v are associated with the local part of the free energy (intrinsic free energy of the ideal gas).

The second term in the free energy, $f_{m-e} = \alpha/2(\mathbf{m}\cdot\nabla n)^2$, couples the magnetization field to the gradient of the density field. This term is associated with 1) the magneto-elastic effects leading to the deformation of a ferromagnetic sample under the influence of an external magnetic field, namely, the magnetostriction effect. The coefficient α is related to the magnetostrictive coefficient, L. 2) the fact that the magnetic effects only appear in the solid phase. In a system consisting of the supercooled liquid phase and crystalline phase, the magnetic effects only arise in the crystalline phase. This is because the magnetization is coupled to the *gradient* of the density field. In the liquid phase where the density is constant, $\nabla n = 0$ and f_{m-e} becomes zero. The PFC free energy leads to a periodic structure that matches the atomic sites in the crystalline structure and gives a microscopic description of the properties of the solid [63].

The next square brackets (which will be referred to as $f_{\mathbf{m}}$ in this text) is very similar to the coarse-grained Landau-Ginzburg (LG) free energy for the ferromagnetic transition which was discussed in Section 5.1. There is however a modification to the coefficient of the $|\mathbf{m}|^2$ term. The coefficient of the $|\mathbf{m}|^2$ term in the LG free energy is $a(T - T_c)/2$ and it is responsible for the paramagnetic to ferromagnetic phase transition. The coefficient of $|\mathbf{m}|^2$ in this model is chosen to be $(r_c - \beta n^2)$. It is implicitly temperature dependent and is responsible for the magnetic phase transition in this model. The parameters r_c and β are constant and their values are chosen in such a way that the Curie temperature lies below the coexistence lines in the phase diagram. This condition needs to be satisfied because ferromagnetism normally happens in the solid phase. There are some synthesized materials, called *ferrofluids*, which are ferromagnetic in the liquid phase, but the emergence of a natural ferromagnetism in the liquid phase is not a common phenomenon [24], [25], [31]. The parameters W_0 and γ are equivalent to the parameters W_0 and u in Eq. 5.1. It will be shown in Section 7.4 that the parameter γ is related to the saturation magnetization and the magnetic susceptibility of the material. The parameter W_0 is associated with the width of the magnetic domain walls and determines the magnetic exchange length. It plays an important role in the discussions of Section 9.3.2.

The estimated values of the parameters are $B_s = 0.98, t = 1/2, v = 1/3, \alpha = 10^{-3}, \beta = 1/25, r_c = 1/100, \mu_0 = 10^{-3}$, and $\gamma = 1$. The description of the parameters, how to link them to measurable physical quantities, and how to estimate their numerical values are discussed this section and in Section 7.4.

The last two terms of the free energy

$$f_{\mathbf{B}} = -\mathbf{m} \cdot \mathbf{B} + \frac{|\mathbf{B}|^2}{2\mu_0}, \tag{7.2}$$

is associated with the free energy of the magnetic field inside the ferromagnetic material. The derivation of this free energy is given in Section 7.3.

The magnetic field $\mathbf{B} = \mathbf{B}(\mathbf{r})$ represents the total local magnetic field at a particular position of the material. It can be calculated by adding the induced magnetic field and the external magnetic field

$$\mathbf{B}(\mathbf{r}) = \mathbf{B}_{ind}(\mathbf{r}) + \mathbf{B}_{ext}. \tag{7.3}$$

The external magnetic field is produced by an external source. We set the value of the external magnetic field and its value in this equation is explicitly known. The induced magnetic field is not a result of true current densities arising from charge transport but is a result of atomic currents inside the matter. These atomic currents can be expressed in terms of the macroscopic quantity, magnetization, $\mathbf{M}$. From a macroscopic point of view, all magnetic effects due to the matter can be described in terms of $\mathbf{M}$ [33]. The magnetic field produced by the magnetic current density can be calculated through the vector potential which is defined as

$$\mathbf{B} = \nabla \times \mathbf{A}. \tag{7.4}$$

The vector potential satisfies the Poisson equation

$$\nabla^2 \mathbf{A} = -\mu_0 \nabla \times \mathbf{m}. \tag{7.5}$$

Equation 7.5 can be derived from Ampere's law. The details of the derivation is given in Appendix A. Knowing the value of the magnetization at each position of the system, we solve Eq. 7.5 to calculate the vector potential $\mathbf{A}$, then we use Eq. 7.4 to calculate the magnetic field $\mathbf{B}$.

7.2 Dynamical equations of motion

Similar to the phase field crystal model, the dynamics of the density field n is governed by the the conserved, model B dynamics [54]. Thus

$$\begin{aligned} \frac{\partial n(\mathbf{r}, t)}{\partial t} = \nabla^2 \left(\frac{\delta F(n, \mathbf{m})}{\delta n} \right) = \left(\Delta B + B_s \left(1 + \nabla^2 \right)^2 \right) n - t n^2 + v n^3 - \beta n |\mathbf{m}|^2 \\ + \alpha \left[(\mathbf{m} \cdot \nabla n)(\nabla \cdot \mathbf{m}) + \mathbf{m} \cdot \nabla (\mathbf{m} \cdot \nabla n) \right]. \end{aligned} \tag{7.6}$$

The dynamics of the magnetization fields m_x and m_y are governed by the model A dynamics [30]. The magnetization is not a conserved quantity in the ferromagnetic phase transition. Thus the equations of motion for magnetization in x and y directions follow

$$\begin{aligned}\frac{\partial m_x(\mathbf{r},t)}{\partial t} &= -\frac{\delta F(n,\mathbf{m})}{\delta m_x} = W_0^2\nabla^2 m_x - \left(r_c - \beta n^2\right) m_x - \gamma m_x|\mathbf{m}|^2 \\ &\quad + \alpha\left(\mathbf{m}\cdot\nabla n\right)\partial_x n + B_x,\end{aligned} \tag{7.7}$$

$$\begin{aligned}\frac{\partial m_y(\mathbf{r},t)}{\partial t} &= -\frac{\delta F(n,\mathbf{m})}{\delta m_y} = W_0^2\nabla^2 m_y - \left(r_c - \beta n^2\right) m_y - \gamma m_y|\mathbf{m}|^2 \\ &\quad + \alpha\left(\mathbf{m}\cdot\nabla n\right)\partial_y n + B_y.\end{aligned} \tag{7.8}$$

The details of calculations of the equations of motion and the functional derivative calculations are given in Appendix A.

7.3 Magnetic Free Energy

In this section, we derive the thermodynamic relations for a magnetic substance in a magnetic field. The discussions of this section are based on [42] and are in *SI units*. It can be shown that the work required to change the magnetic induction in a unit volume of material is [33]

$$dw_b = \mathbf{H}\cdot d\mathbf{B}, \tag{7.9}$$

where $\mathbf{H}$ is the external magnetic field and $\mathbf{B}$ is the magnetic induction inside the material.

The differential of the free energy per unit volume of the material is given by

$$dF = -S\,dT + \xi d\rho + \mathbf{H}\cdot d\mathbf{B}, \tag{7.10}$$

where S is the entropy, ξ is the chemical potential, ρ is the density and T is the temperature of the system. The thermodynamic potential is defined as

$$\tilde{F} \equiv F - \mathbf{H}\cdot\mathbf{B}. \tag{7.11}$$

The differential form of this equation is

$$d\tilde{F} = -S\,dT + \xi d\rho - \mathbf{B}\cdot d\mathbf{H}, \tag{7.12}$$

which implies that

$$\frac{\partial\tilde{F}}{\partial\mathbf{H}} = -\mathbf{B}. \tag{7.13}$$

Integrating this equation and using the fact that $\mathbf{B} = \mu_0(\mathbf{H} + \mathbf{M})$, where μ_0 is the permeability of the free space, we obtain

$$\tilde{F} = \tilde{F}(\mathbf{M},0) - \mu_0\Big(\mathbf{M}\cdot\mathbf{H} - \frac{\mathbf{H}^2}{2}\Big). \tag{7.14}$$

From this equation and using Eq. 7.13, we can calculate the free energy to be

$$\begin{aligned} F &= \tilde{F} + \mathbf{H}\cdot\mathbf{B} \\ &= \tilde{F}(\mathbf{M},0) - \mu_0\mathbf{M}\cdot\mathbf{H} - \frac{\mu_0}{2}\mathbf{H}^2 + \mathbf{H}\cdot\mathbf{B} \\ &= \tilde{F}(\mathbf{M},0) - \frac{\mu_0}{2}\mathbf{H}^2 + \mathbf{H}\cdot(\mathbf{B}-\mu_0\mathbf{M}) \\ &= \tilde{F}(\mathbf{M},0) + \frac{\mu_0}{2}\mathbf{H}^2 \\ &= \tilde{F}(\mathbf{M},0) + \frac{\mathbf{B}^2}{2\mu_0} + \frac{\mu_0}{2}\mathbf{M}^2 - \mathbf{M}\cdot\mathbf{B}. \end{aligned} \tag{7.15}$$

This is the expression we used in the free energy of the magnetic PFC model, Eq. 7.1.

7.4 Estimation of the parameters

The Magnetic PFC free energy is a phenomenological free energy constructed to describe certain properties of magnetic materials. The quantities and variables in this free energy are made dimensionless by dividing them by relevant parameters of the system. For example lengths are written with respect to lattice spacing.

We estimate the values of these dimensionless quantities by comparing the numerical values of the different terms obtained from simulations with each other and knowing the physical significance of each term from experiments. We can also link the parameters of the free energy to measurable physical quantities and estimate their values.

7.4.1 Estimation of the permeability

To estimate the value of μ_0 it is useful to note that the LG part of the free energy for the ferromagnetic phase transition, $f_{\mathbf{m}}$, incorporates the exchange interaction of the Weiss molecular field into the free energy. On the other hand in the absence of an external magnetic field, $\mathbf{B} = \mathbf{B}_{ind}$ and $f_{\mathbf{B}}$ is the free energy of the induced magnetic field which is equal to the classical magnetic moment interaction of the Weiss molecular field. As estimated in Section 2.4, the field arising from the magnetic dipole interaction is 10^{-4} times weaker than the exchange interaction. This information helps us to set the value of the permeability, mu_0, in the units of our model. Comparing the numerical values of the exchange portion of the free energy in Eq. 7.1 (obtained from simulations) with the magnetic dipole interaction, $f_{\mathbf{B}}$,we can see that by choosing $\mu_0 \equiv 10^{-3}$ the free energy of the magnetic dipole interaction becomes of the order of $10^{-4} - 10^{-5}$ relative to the exchange interaction. If $\mu_0 \equiv 1$ for example, these two energy terms become of the same order of magnitude, which is not physical.

7.4.2 Estimation of the parameters of the magnetic system

In this section we first discuss how to connect the parameters of the LG free energy of ferromagnetic transition, $f_{\mathbf{m}}$, to measurable quantities such as the saturation magnetization, m_s, and

the magnetic susceptibility, χ. Considering the simple LG free energy of ferromagnetic phase transition

$$f(m) = \frac{A(T - T_c)}{2} m^2 + \frac{u}{4} m^4, \tag{7.16}$$

and minimizing with respect to m, for the magnetization below the Curie temperature we obtain

$$m = \sqrt{\frac{-A(T - T_c)}{u}}. \tag{7.17}$$

Noting that the saturation magnetization is the magnetization at $T = 0$, namely, $m_s = m(T = 0)$, we obtain

$$m_s = \sqrt{\frac{AT_c}{u}}. \tag{7.18}$$

The saturation magnetization is an experimentally measurable quantity. It has a value of the order of $m_s = 1752, 1446$, and 512 for Iron, Cobalt, and Nickel, respectively [59]. The value of T_c is measured to be $780(774)^\circ C$, $1075(1231)^\circ C$, and $365(372)^\circ C$ for Iron, Cobalt and, Nickel, respectively. The first temperature is obtained from the heat capacity measurements at constant volume and the second one enclosed in the parentheses is measured at constant pressure. Knowing m_s and T_c, we can calculate the value of the ratio A/u.

To estimate the value of A, we consider the LG free energy of magnetic phase transition in the presence of an external magnetic field, Eq. 4.6,

$$f_{m,B} = \frac{A(T - T_c)}{2} m^2 + \frac{u}{4} m^4 - Bm. \tag{7.19}$$

Minimizing with respect to m

$$\frac{\partial f_{m,B}}{\partial m} \equiv 0, \tag{7.20}$$

yields

$$A(T - T_c)m + um^3 - B = 0. \tag{7.21}$$

The magnetic susceptibility, χ, is defined as

$$\chi = \frac{\partial m}{\partial B}\Big|_{B=0}. \tag{7.22}$$

Differentiating Eq. 7.21, with respect to B gives

$$(A(T - T_c) + 3um^2)\frac{\partial m}{\partial B} = 1, \tag{7.23}$$

Rephrasing this equation for $\chi = \partial m/\partial B$ and noting that $m = 0$ for $T > T_c$ and $m \neq 0$ for $T < T_c$, we obtain

$$\chi = \begin{cases} \frac{1}{A(T-T_c)} & \text{for } T > T_c \\ \frac{1}{2A(T-T_c)} & \text{for } T < T_c. \end{cases} \tag{7.24}$$

Knowing the behaviour of χ near the critical point, we can calculate the value of A.

7.4.3 Estimation of the coefficient of the magneto-elastic coupling term

The purpose of this section is to estimate the value of the parameter α. To estimate α, we need the expression for the free energy in terms of the stain tensor. This calculation is done in Section 8.3. Here we use the equations obtained in that section, and estimate α, to keep continuity of the subject.

The magnetostrictive coefficient, L, is defined as the fractional change in the length of the sample as the magnetization of the material increases from zero to the saturation value (m_s).

Considering Eqs. 8.23-8.25, we can see that

$$U_{ij} \propto \frac{\alpha}{B_s}|\mathbf{m}|^2, \tag{7.25}$$

Substituting $|\mathbf{m}| = |\mathbf{m}_s|$ into this relation, we obtain a relation for fractional change in the length at saturation magnetization, which is equal to the magnetostrictive coefficient

$$L \sim \frac{\alpha}{B_s}|\mathbf{m}_s|^2. \tag{7.26}$$

The measured values for the magneostrictive coefficient L are $\sim 10^{-5}$.The quantities in the free energy, i.e., B_s and $\mathbf{m}$ are written in dimensionless units. We set $B_s = 0.98$ and the saturation magnetization from the simulations comes out to be of order of unity. Therefore for α, we obtain

$$\alpha \sim 10^{-5}. \tag{7.27}$$

Chapter 8

Analytical Results

In this chapter we use the amplitude expansion method to obtain an expression for the free energy in terms of the amplitudes of the density field in Fourier space and consider the small elastic deformations. This helps us to further discover the properties of the model and to comprehend the implications of each term more profoundly. In Section 8.2, we minimize the free energy using a set of estimated values of the parameters of the free energy and calculate the equilibrium phases of the model, *i.e.*, liquid, non-magnetic solid and magnetic solid. In Section 8.3, we discuss the magneto-elastic effects in ferromagnetic materials, using the Magnetic PFC model. Finally, in Section 8.4 we discussed what happens when an external magnetic field is applied to a magnetic system both qualitatively and quantitatively, by plotting the free energy obtained in Section 8.2. This helps us to analytically calculate the hysteresis curve of a single crystal using the free energy of the Magnetic PFC model.

8.1 Amplitude Expansion

In this section, we use the amplitude expansion method explained in Section 6.3 to calculate the Magnetic PFC free energy in terms of the variable amplitudes of the density field. This enables us to include the longer-range elastic effects in the free energy and study the effect of small deformations in the system.

We perform the phase diagram calculations, by excluding the terms that contain the magnetic field $\mathbf{B} = \mathbf{B}_{ind} + \mathbf{B}_{ext}$. This is reasonable, since the Curie temperature should be calculated in the absence of any external magnetic field ($\mathbf{B}_{ext} = 0$). The induced magnetic field, $\mathbf{B}_{ind}$, can also be ignored since as explained in Section 2.4.1, the dipole-dipole interaction portion of the molecular field is much smaller than the exchange interaction portion (by a factor of 10^{-4}). Therefore it is reasonable to ignore $\mathbf{B}_{ind}$ and define:

$$F \equiv \frac{\Delta F}{k_B T V \bar{\rho}} - \int d\mathbf{r}\Big(- \mathbf{m} \cdot \mathbf{B} + \frac{|\mathbf{B}|^2}{2\mu_0}\Big). \tag{8.1}$$

As explained in Section 6.3, in the amplitude expansion method we expand the density field in Fourier series

$$n = n_0 + \sum_j \eta_j e^{i\mathbf{q}_j \cdot \mathbf{r}} + C.C, \tag{8.2}$$

where $C.C$ is the complex conjugate of the expansion and $\mathbf{q}_1 = -\sqrt{3}/2\mathbf{i} - 1/2\mathbf{j}$, $\mathbf{q}_2 = \mathbf{j}$ and $\mathbf{q}_3 = \sqrt{3}/2\mathbf{i} - 1/2\mathbf{j}$ for a triangular two dimensional system. We insert this expansion into the free energy and integrate over the space.

To integrate we use the assumption that the amplitudes, η_j, vary on length scale much larger than the lattice constant. With this assumption, we can approximate the integrals by ignoring the spatial dependence of the amplitudes over a unit cell. Using this "quick and dirty approximation" [54], we can evaluate the integrals to get

$$
\begin{aligned}
F_\eta = \int d\mathbf{r} \Bigg\{ & (\Delta B + B_s)\left(\frac{1}{2}n_0^2 + \sum_j |\eta_j|^2\right) \\
& + B_s\left(-\sum_j |\eta_j|^2 + \sum_j |\mathcal{G}_j\eta_j|^2\right) \\
& - t\left(\frac{1}{3}n_0^3 + 2n_0\sum_j |\eta_j|^2 + 2\left(\prod_j \eta_j + \prod_j \eta_j^*\right)\right) \\
& + v\left(\frac{1}{4}n_0^4 + 3n_0^2\sum_j |\eta_j|^2 + \frac{3}{2}\sum_j |\eta_j|^4 + 6\left(|\eta_1|^2|\eta_3|^2 + |\eta_1|^2|\eta_2|^2 + |\eta_2|^2|\eta_3|^2\right) + 6n_0\left(\prod_j \eta_j + \prod_j \eta_j^*\right)\right) \\
& - \alpha\sum_j |\mathcal{A}_j\eta_j|^2 \\
& + \left(\frac{W_0^2}{2}|\nabla^2\mathbf{m}|^2 + \left[r_c - \beta\left(n_0^2 + 2\sum_j |\eta_j|^2\right)\right]\frac{|\mathbf{m}|^2}{2} + \gamma\frac{|\mathbf{m}|^4}{4}\right)\Bigg\},
\end{aligned}
\tag{8.3}
$$

where the operators $\mathcal{G}_j$ and $\mathcal{A}_j$ are defined as $\mathcal{G}_j \equiv \left(\nabla^2 + 2i\mathbf{q}_j\cdot\nabla\right)$ and $\mathcal{A}_j \equiv \mathbf{m}\cdot\left(\nabla + i\mathbf{q}_j\right)$.

We can now consider the elastic deformations by inserting $\eta_j = \phi e^{i\mathbf{q}_j\cdot\mathbf{u}}$ into Eq. 8.3 and knowing the vectors $\mathbf{q}_1$, $\mathbf{q}_2$ and $\mathbf{q}_3$ for the triangular two dimensional lattice.We obtain:

$$
\begin{aligned}
F_{\phi,U_{ij}} = \int d\mathbf{r} \Bigg\{ & \Big(-\frac{t}{3} + \frac{1}{2}(\Delta B + B_s)\Big)n_0^2 + \frac{v}{4}n_0^4 + \phi^2\Big(3\Delta B - 6tn_0 + 9vn_0^2\Big) + \phi^3\Big(-4t + 12vn_0\Big) + \phi^4\Big(\frac{45}{2}v\Big) \\
& + B_s\left[\phi^2\left(\frac{9}{2}\left(U_{xx}^2 + U_{yy}^2\right) + 3U_{xx}U_{yy} + 6U_{xy}^2\right)\right] \\
& - 3\alpha\phi^2\left(U_{xx}|m_x|^2 + U_{yy}|m_y|^2 + 2U_{xy}m_xm_y\right) \\
& + \left(\frac{W_0^2}{2}|\nabla\mathbf{m}|^2 + \left[r_c - \beta\left(n_0^2 + 6\phi^2\right) - 3\alpha\phi^2\right]\frac{|\mathbf{m}|^2}{2} + \gamma\frac{|\mathbf{m}|^4}{4}\right)\Bigg\},
\end{aligned}
\tag{8.4}
$$

where U_{ij} are the linear strain tensor elements and are defined as

$$
U_{ij} = \frac{1}{2}\left(u_{ij} + u_{ji} + \sum_k u_{ik}u_{jk}\right) \tag{8.5}
$$

in which $i, j = 1, 2$ and u_{ab} is defined as:

$$u_{ab} = \frac{\partial u_a}{\partial b}. \tag{8.6}$$

Thus,

$$U_{xx} = u_{xx} + \frac{1}{2}(u_{xx}^2 + u_{yx}^2) \tag{8.7}$$

$$U_{yy} = u_{yy} + \frac{1}{2}(u_{yy}^2 + u_{xy}^2) \tag{8.8}$$

$$U_{xy} = \frac{1}{2}(u_{xy} + u_{yx} + u_{xx}u_{xy} + u_{yx}u_{yy}). \tag{8.9}$$

The complete derivation of the amplitude expansion and the elastic deformation can be found in Appendix B. Writing the free energy in this form helps us to better understand the physical meaning of each term. The first line of this equation describes the first order solid-liquid phase transition, the second line represents the elastic energy which is zero in the liquid phase ($\phi = 0$), as expected. The third line is associated with f_{m-e}, *i.e.*, the magneto-elastic effects in ferromagnetic materials and its physical implications will be considered in Section 8.3. The last line describes the ferromagnetic phase transition. Using this free energy, and the one-mode approximation, we calculate the phase diagram of the model in the next section.

8.2 Phase diagram

In this section we minimize the free energy, Eq. 8.4, with respect to the strain tensor elements, U_{ij}, and magnetization, $|\mathbf{m}|$. Then we set the parameters r_c and β so that the ferromagnetic transition occurs in the solid phase [31]. We show that this free energy is minimized by three phases: liquid, non-magnetic solid and magnetic solid.

To minimize the free energy with respect to U_{xx}, U_{xy} and U_{yy} we need to solve

$$\frac{\partial f_{\phi,U_{ij}}}{U_{ij}} = 0, \tag{8.10}$$

for U_{xx}, U_{yy} and U_{xy}, and we obtain

$$U_{xx} = \frac{\alpha}{8B_s}(3m_x^2 - m_y^2) \tag{8.11}$$

$$U_{yy} = -\frac{\alpha}{8B_s}(m_x^2 - 3m_y^2) \tag{8.12}$$

$$U_{xy} = \frac{\alpha}{2B_s}m_x m_y. \tag{8.13}$$

Inserting U_{xx}, U_{yy} and U_{xy} into the free energy, Eq. 8.4 gives

$$
\begin{aligned}
F_\phi = \int d\mathbf{r}\Bigg\{ & \frac{W_0^2}{2}\left|\nabla\mathbf{m}\right|^2 + \left(-3\alpha\phi^2 - 6\beta\phi^2 + r_c - \beta n_0^2\right)\frac{|\mathbf{m}|^2}{2} + \left(-\frac{9}{4}\frac{\phi^2\alpha^2}{B_s} + \gamma\right)\frac{|\mathbf{m}|^4}{4} \\
& + \left(3\Delta B - 6tn_0 + 9vn_0^2\right)\phi^2 + \left(12vn_0 - 4t\right)\phi^3 + \frac{45}{2}v\phi^4 \\
& + \left[\frac{1}{2}\left(B_s + \Delta B\right) - \frac{1}{3}t\right]n_0^2 + \frac{1}{4}vn_0^4\Bigg\}.
\end{aligned}
\tag{8.14}
$$

To see the similarities of this free energy with the LG free energy of ferromagnetic phase transition of Eq. 5.1, F_ϕ is written in the order of decreasing powers of the magnetization, $|\mathbf{m}|$. Accordingly, the sign of the coefficient of the second order term, $|\mathbf{m}|^2$, determines whether the system is paramagnetic or ferromagnetic. To calculate the temperature and the density at which the ferromagnetic phase transition occurs, we minimize f_ϕ (the integrand) with respect to $|\mathbf{m}|$. Solving the equation $\partial f_\phi/\partial|\mathbf{m}| = 0$ we obtain

$$
|\mathbf{m}| = 0, \pm\sqrt{\frac{-\left(r_c - n_0^2\beta - 6\phi^2\beta + 3\phi^2\alpha\right)}{\gamma - \frac{9}{4}\frac{\alpha^2\phi^2}{B_s}}},
\tag{8.15}
$$

where ϕ is the amplitude of the density field expansion, in the traditional PFC model. We calculate it by minimizing the Magnetic PFC free energy with respect to ϕ, assuming $|\mathbf{m}| = 0$. This gives

$$
\phi_{min}^{PFC} = -\frac{n_0}{5} + \frac{1}{10} + \frac{1}{10}\sqrt{1 + 16n_0 - 16n_0^2 - 20\Delta B}.
\tag{8.16}
$$

It is a function of the mean density, n_0, and the temperature ΔB.

Since $\alpha = 10^{-3}$ is much smaller than $\gamma = 1$, the denominator in Eq. 8.15 is always positive. Therefore by requiring that the expression on the numerator be positive, we can determine the set of densities and temperatures for which the net magnetization of the system is not zero and the system is magnetic. To find the transition line in the $\Delta B - n_0$ plane, above which $|\mathbf{m}| = 0$ and below which $|\mathbf{m}|$ has a finite value, we should solve

$$
r_c - n_0^2\beta - 6\phi^2\beta + 3\phi^2\alpha = 0.
\tag{8.17}
$$

Inserting $\phi = \phi_{min}^{PFC}$ from Eq. 8.16 into this equation and solving it for ΔB gives us a line in the $\Delta B - n_0$ phase diagram, called the *Curie line*, that separates the non-magnetic phase from the magnetic phase

$$
\begin{aligned}
\Delta B = \; & -\frac{1}{30}\frac{1}{-2\beta+\alpha}\Bigg(\frac{-6\beta+12\beta n_0-6\alpha n_0+3\alpha+10\sqrt{-6\beta^2n_0^2+3\beta n_0^2\alpha+6\beta r_c-3\alpha r_c}}{-2\beta+\alpha}\left(-2\beta + 4\beta n_0 - 2\alpha n_0 + \alpha\right) \\
& + 14\beta n_0^2 + 36\beta n_0 + 6\beta + 18\alpha n_0^2 - 18\alpha n_0 - 3\alpha - 50r_c\Bigg).
\end{aligned}
\tag{8.18}
$$

Inserting the parameter values into this equation, we can plot the Curie line. The values of r_c and β can be assigned at this point. By changing the values of r_c and β, we can change

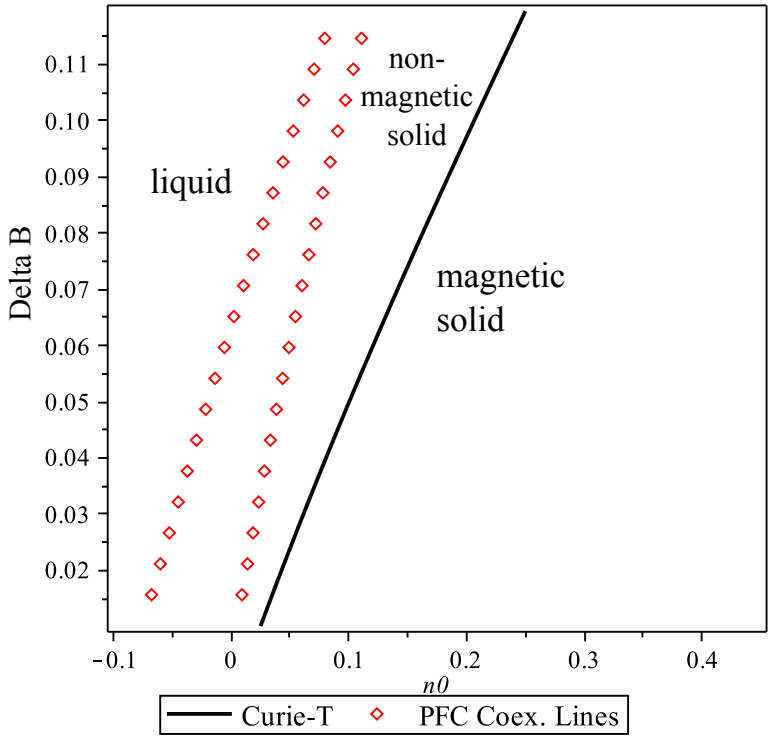

Figure 8.1: A phase diagram of the magnetic PFC model. The dots denote the liquid-solid coexistence lines of the PFC model and the line denotes the Curie line, above which the solid is not magnetic and below which it becomes magnetic.

the position of the Curie line in the phase diagram. Since we know that the magnetic phase only occurs in the solid phase, we choose them in such a way that this line lies below the PFC coexistence lines. If we increase r_c or decrease β, the line will shift down.

The phase diagram of the magnetic PFC model is shown in Fig. 8.1, with $B_s = 0.98, t = 1/2, v = 1/3, \alpha = 10^{-3}, \beta = 1/25, r_c = 1/100, \mu_0 = 10^{-3}, \gamma = 1$. It should be mentioned that the liquid-solid coexistence lines depicted in the phase diagram are the same as the PFC coexistence lines, since above the Curie line, where the liquid-solid transition happens, $|\mathbf{m}| = 0$ and the free energy reduces to the PFC free energy.

8.3 The magneto-elastic effects

In this section we consider only the effect of the magno-elastic term on a square crystal sample. Our purpose is to understand how a non-zero magnetization $\mathbf{m} = (m_x, m_y)$ caused by an external magnetic field, can deform the sample. To check this effect we consider the PFC portion of the free energy together with the magneto-elastic coupling term, f_{m-e}

$$\mathcal{F}_{m-e} \propto \int d\mathbf{r}\Big[n(B_s(1+\nabla^2)^2)n - \frac{\alpha}{2}(\mathbf{m}\cdot\nabla n)^2\Big]. \tag{8.19}$$

Performing the amplitude expansion we get

$$\mathcal{F}_{m-e} \propto 2 \int d\mathbf{r} \sum_j \Big(|\mathcal{G}_j \eta_j|^2 - \alpha |\mathbf{m} \cdot \mathcal{A}_j \eta_j|^2 \Big), \tag{8.20}$$

where $\mathcal{G}_j = \nabla^2 + 2\mathbf{q}_j \cdot \nabla$. Now considering the small deformations by letting $\eta_j = \phi e^{i\mathbf{q}_j \cdot \mathbf{u}}$, we get

$$\frac{\mathcal{F}_{m-e}}{\phi^2} = B_s \Big[9(U^2 xx + U_{yy}^2 + 12 U_{xy}^2) - 6\alpha(m_x^2 U_{xx} + m_y^2 U_{yy}) - 3\alpha |\mathbf{m}|^2 \Big]. \tag{8.21}$$

Since we are considering the effect at a constant temperature and density, ϕ is a constant and we can take it out of the integral. Minimizing this free energy with respect to the strain tensor elements, U_{xx}, U_{yy} and U_{xy} gives U_{xx}, U_{yy} and U_{xy} as in Eqs. 8.11, 8.12 and 8.13. Substituting back into the free energy $\mathcal{F}_{m-e}$, Eq. 8.20, we obtain

$$\mathcal{F}_{m-e} = -\frac{1}{2B_s} \Big(\frac{3}{2} \alpha \phi |\mathbf{m}|^2 \Big)^2. \tag{8.22}$$

To see the influence of a non-zero magnetization vector on the structure of a ferromagnetic sample, we assume that the magnetization, $\mathbf{m}$, has an angle, θ, with the x-axis and insert $\mathbf{m} = (m\cos\theta, m\sin\theta)$ into the strain tensor Eqs. 8.11, 8.12 and 8.13 giving

$$U_{xx} = -\frac{\alpha}{8B_s} m^2 (1 - 4\cos^2\theta) = \frac{\alpha}{8B_s} m^2 (2\cos(2\theta) + 1) \tag{8.23}$$

$$U_{yy} = -\frac{\alpha}{8B_s} m^2 (1 - 4\sin^2\theta) = -\frac{\alpha}{8B_s} m^2 (2\cos(2\theta) - 1) \tag{8.24}$$

$$U_{xy} = \frac{\alpha}{2B_s} m^2 (\cos\theta \sin\theta) = -\frac{\alpha}{B_s} \sin(2\theta). \tag{8.25}$$

Knowing the strain tensor elements as a function of $|\mathbf{m}|$ and θ, we can use the *infinitesimal strain theory*[1] to calculate the deformation of a square sample of dimension L as a result of a finite magnetization, $\mathbf{m}$. An external magnetic field can be used to change the value and direction of the magnetization vector, $\mathbf{m}$, and therefore to deform a ferromagnetic sample to the desired shape.

Using the infinitesimal strain theory and assuming that $u_{xy} = u_{yx}$ for simplicity, the four corners of a square sample of dimension L transform to [62]

$$(0,0) \rightarrow (0,0) \tag{8.26}$$

$$(L,0) \rightarrow (L(1+u_{xx}), Lu_{xy}) \tag{8.27}$$

$$(0,L) \rightarrow (Lu_{xy}, L(1+u_{yy})) \tag{8.28}$$

$$(L,L) \rightarrow (L(1+u_{xx}+u_{xy}), L(1+u_{yy}+u_{xy})). \tag{8.29}$$

[1] This theory discusses the infinitesimal deformation of a continuum body. A small displacement of particles of a deformed body is shown by the components of the displacements, u_x, u_y, in two dimensions. In this theory it is assumed that these two components are very small quantities and vary continuously [62].

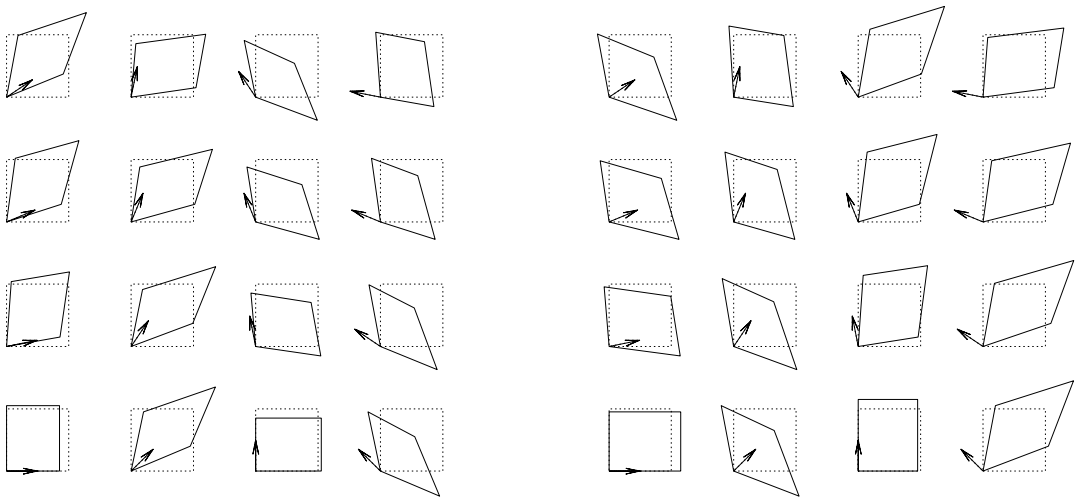

Figure 8.2: The magneto-elstic deformations for a ferromagnetic sample of dimension L. The original shape of the sample is depicted by the dotted lines and the deformed samples are depicted by solid lines. The arrows show the direction of the magnetization vector, $\mathbf{m}$, in each case. The left plots are for $\alpha = -0.1$ and the right plots for $\alpha = 0.1$.

Inserting the strain tensor elements from Eqs. 8.23-8.25, we calculated deformation of a square ferromagnetic sample for various magnetization vectors. The results for two values for the magnetostrictive coefficients, *i.e.*, $\alpha = 0.1$ and $\alpha = -0.1$ are shown in Fig. 8.2. The left bottom vertex of the square is at (0,0) and the arrows show the magnetization vector in each case. The deformations are evaluated, assuming that $m^2/8B_s = 1/2$. As explained in Section 2.6.4, for a negative magnetostrictive coefficient, we expect the change in length of the sample be negative and the sample shrinks, as shown in the left plots in Fig. 8.2.

8.4 Analytical coercivity calculations

In this section we first explain how hysteresis occurs in practice and then analytically calculate the coercivity in the Magnetic PFC model.

As explained in Section 4.2 an external magnetic field tends to tilt the double well structure of the LG free energy of magnetic transition and force the system to choose one of the states, $+|m_0|$ or $-|m_0|$ depending on the direction of the applied magnetic field.

We first assume that the temperature is below the Curie temperature, there is no external magnetic field and the system has a mean magnetization of $-|m_0|$. If now an external magnetic field of $+|H|$ is applied to the system, it tends to align the the magnetic moments with it by changing the direction of the magnetic moments from the negative direction to the positive direction.

From another point of view, application of an external magnetic field causes the free energy to be tilted. When the magnetic field is in the positive direction, it causes the free energy to have a local minimum at $-|m_0|$ and a global minimum at $+|m_0|$, as illustrated in Fig. 8.3(a).

The local minimum is a metastable state of the system. This means that if there is not any fluctuations in the system, for example when the temperature is zero, the moments that are in the negative direction are not able to flip to the positive direction and the mean magnetization of the system will remain negative.

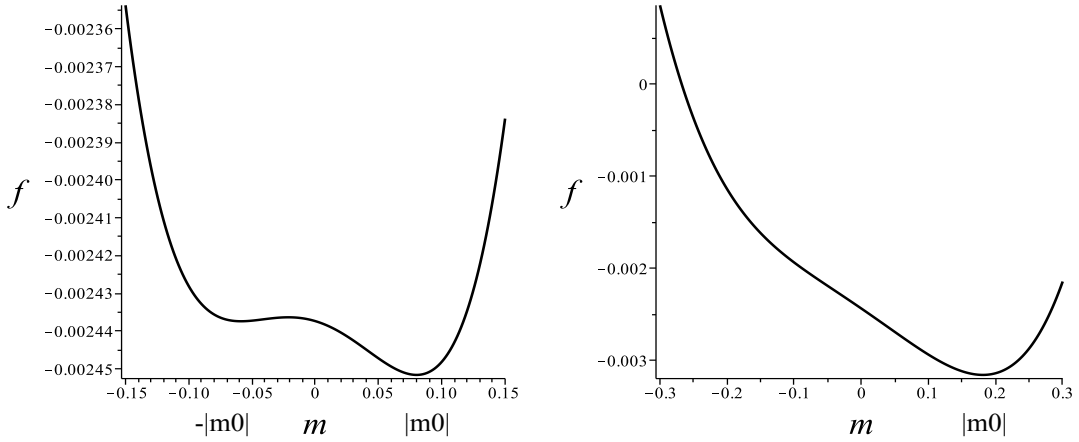

(a) $H_y < H_a$ (b) $H_y > H_a$

Figure 8.3: The plot of the magnetic free energy, Eq. 8.31, for different values of external magnetic field. The magnetic field H_a is the minimum field necessary to remove the local minimum of the free energy. In (a) $H_y = 10^{-4}$ is smaller than the analytical value $H_a = 1.5 \times 10^{-4}$. The free energy is tilted but has two minima at $-|m_0|$ and $+|m_0|$. In (b) the external magnetic field, $H_y = 5 \times 10^{-3}$, is larger than H_a and as expected, the local minima has disappeared and the free energy has only one minima at $+|m_0|$.

If we further increase the magnitude of the external magnetic field, it tilts the free energy to a greater extent until it reaches to a value at which the local minimum is removed and the free energy has only one global minimum. This state is illustrated in Fig. 8.3(b). Accordingly, in this state the magnetic moments gradually orient in the direction of the magnetic field and the mean magnetization of the system becomes $+|m_0|$.

We can see the same process in the hysteresis loop of a ferromagnetic material Fig. 2.4. In this plot the vertical axis represents both the magnetic induction, **B**, and the magnetization, **m**, i.e., both quantities have the same behaviour [60]. If we start from negative magnetization value, for example from the point where the loop crosses the vertical axis and increase the external magnetic field, the magnetization increases with a mild slope until it reaches to a point where the slope suddenly increases and the mean magnetization of the system sharply changes from a negative value to a positive value. This sharp change happens when the magnetic field **H** is strong enough to remove the local minimum of the free energy and all of the magnetic moments align with the external magnetic field. The coercivity is defined as the external magnetic field required to make the mean magnetization of the system zero and to completely demagnetize it [60].

To calculate the coercivity using the Magnetic PFC model, we need to find out at what external magnetic field the local minimum of the free energy disappears. To calculate this

magnetic field we should solve

$$\frac{df_\phi}{dm} = 0 \tag{8.30}$$

in which f_ϕ comes from Eq. 8.14 including $-\mathbf{m}\cdot\mathbf{H}$ for the interaction of the external magnetic field ($\mathbf{H}$) and magnetic moments.

$$\begin{aligned} f_\phi = {} & \frac{W_0^2}{2}|\nabla\mathbf{m}|^2 + \left(-3\alpha\phi^2 - 6\beta\phi^2 + r_c - \beta n_0^2\right)\frac{|\mathbf{m}|^2}{2} + \left(-\frac{9}{4}\frac{\phi^2\alpha^2}{B_s} + \gamma\right)\frac{|\mathbf{m}|^4}{4} \\ & + \left(3\Delta B - 6tn_0 + 9vn_0^2\right)\phi^2 + (12vn_0 - 4t)\,\phi^3 + \frac{45}{2}v\phi^4 \\ & + \left[\frac{1}{2}(B_s + \Delta B) - \frac{1}{3}t\right]n_0^2 + \frac{1}{4}vn_0^4 - \mathbf{m}\cdot\mathbf{H}. \end{aligned} \tag{8.31}$$

We use the same parameters as we used to calculate the phase diagram and solve Eq. 8.30. The roots of this equation represent the magnetization values fort which the free energy is minimum.

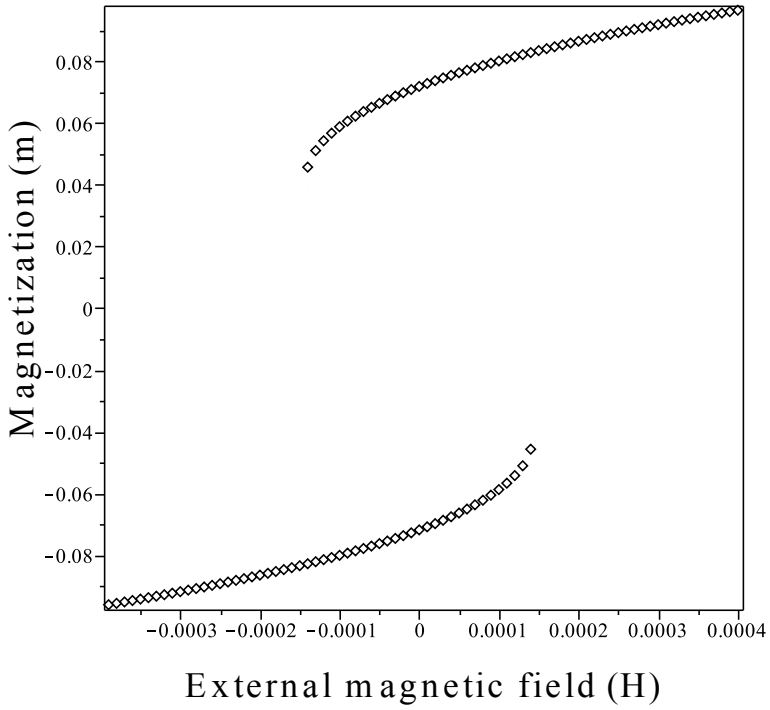

Figure 8.4: The vertical axis represents the magnetization m and the dotted lines represent the two roots of of Eq. 8.30, corresponding to positive and negative magnetization minimum. It is seen that the solid line stops at about $H_a = 1.5 \times 10^{-4}$. This magnetic field corresponds to the field at which the local minimum of the free energy disappears and the system jumps to the global minimum, i.e, the positive magnetization.

Fig. 8.4 shows the roots of Eq. 8.30 for different values of external magnetic field. It is clear from this plot that one of the roots disappears, *i.e.*, becomes a complex number, at an external magnetic field of approximately $H_a = 1.5 \times 10^{-4}$. This magnetic field is equivalent to the magnetic field at which the local minimum in the free energy disappears (Fig. 8.3(b)). This calculation gives us an insight into the approximate value[2] of the magnetic field to be applied to the system, for the system to jump from the $-|m_0|$ state to the $+|m_0|$ state, and allows us to calculate the coercivity using simulations.

To calculate the coercivity we first need to determine the exact magnetic field at which the transformation from one state to the other happens, using numerical simulations. This procedure and the results will be discussed in Section 9.2. Essentially we need to perform a few simulations, applying constant magnetic field about H_a to the system and check at what value of H, the mean magnetization of the system will change from a negative value to a positive value.

[2]It is "approximate" because we used a single mode approximation to calculate the free energy f_ϕ.

Chapter 9

Numerical Results

In this chapter we present the results of the simulations done, to reproduced the experimental data on soft magnetic nanocrystalline materials [27], using the Magnetic PFC model. We also provide theoretical arguments to explain the results of simulations and justify the dependence of the coercivity on the grain size.

The simulations are performed by solving the dynamical equations of motion Eqs. 7.6-7.8 together with Eqs. 7.4 and 7.5 to calculate the induced magnetic field. We used the values obtained in Appendix 7 for the phenomenological parameters involved in the free energy.

The aim of our simulations is to validate the results of the analytical phase diagram calculations and more importantly to reproduce the experimental diagram in Fig. 3.7 with the Magnetic PFC model.

This diagram presents the experimental data obtained by measuring the coercivity of materials having various grain sizes [29], to clarify the dependence of the coercivity on the grain size. They also reported the unusual combination of soft magnetic properties and ultrafine grain structure in iron based nanocrystalline alloys (Fe-Cu-Nb-Si-B) alloys. This phenomenon is theoretically explained by the Random Anisotropy Model [27] and was described in Section 3.3. This is an important phenomena since it offers the opportunity of tailoring the magnetic properties of soft magnetic materials using magnetic field annealing [28].

We perform simulations to reproduce this effect using the Magnetic PFC model. We also run simulations to check the dependence of the coercivity on the grain boundary angle.

9.1 Phase diagram simulations: liquid, non-magnetic solid and magnetic solid

Three sets of simulations were carried out by choosing the mean density of the system, n_0, and the temperature, ΔB, so that the equilibrium state of the system be located in the liquid, non-magnetic-solid and magnetic solid phases predicted by the phase diagram in Fig. 8.1.

The system was prepared by setting on a constant density everywhere in the system and nucleating solid seeds by creating random fluctuations at arbitrary places of the system. The mean density of the system is n_0. To produce the density fluctuations we generated random numbers of a Gaussian distribution with mean zero and a standard deviation of unity. We

initiated the magnetization field by assigning a random number at all of the grid points. Since this initial state is not the equilibrium state of the system, it will evolve towards

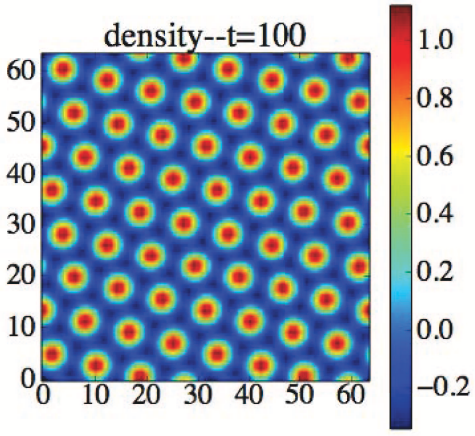

(a) Density-Non-magnetic solid

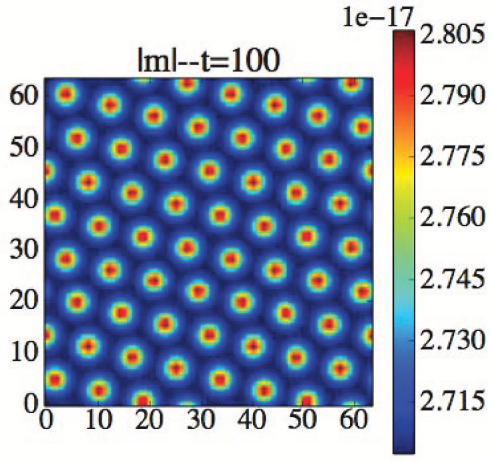

(b) Magnetization-Non-magnetic solid. The magnetization is of order of 10^{-17}.

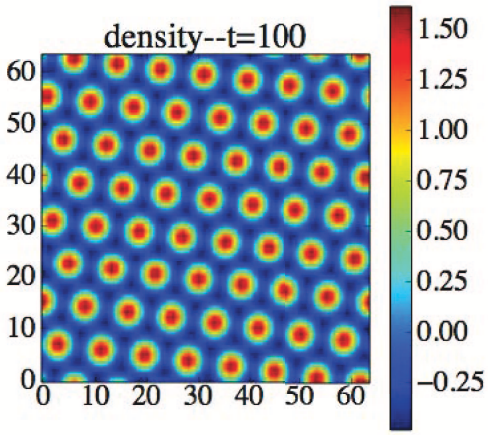

(c) Density-Magnetic solid

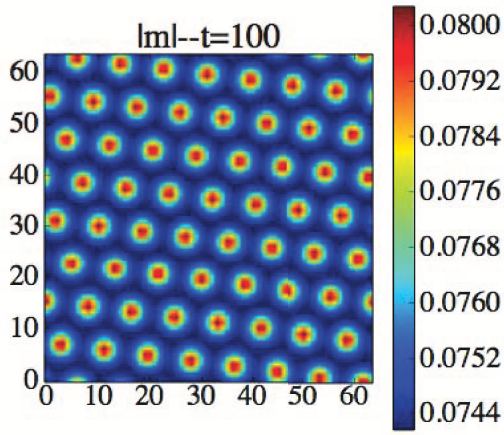

(d) Magnetization-Magnetic solid

Figure 9.1: The final configurations of non-magnetic solid for the density field (a), magnetization field (b) and the final configurations of the magnetic solid, the density field (c) and the magnetization field (d).

its stable state. The system size is $l_x = l_y = 64$ and the total number of time steps is 10^7 with $\Delta t = 10^{-3}$ and $\Delta x = \pi/4$.

Considering the phase diagram, Fig. 8.1, we can see that choosing the following values for density and temperature of the system, the equilibrium state of the system will be in the liquid, non-magnetic solid and magnetic solid:

1. **Liquid:** $n_0 = -0.1, \Delta B = 0.1$

2. **Non-magnetic solid:** $n_0 = 0.125, \Delta B = 0.1$

3. **Magnetic solid:** $n_0 = 0.2, \Delta B = 0.02$

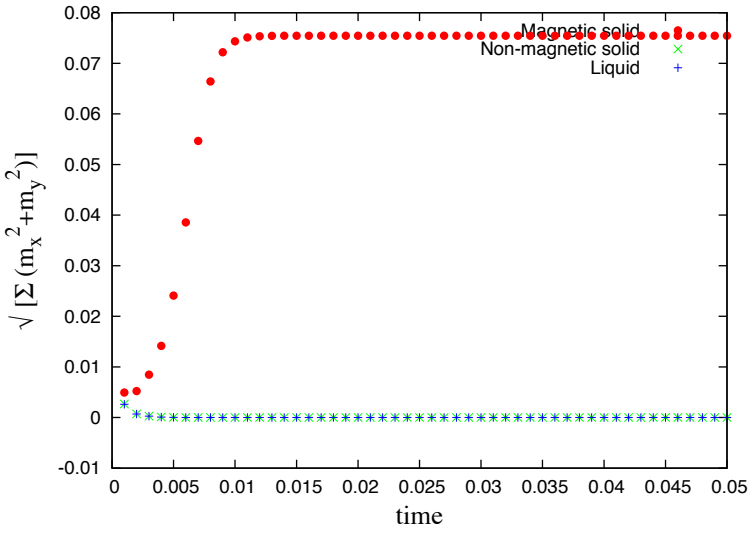

Figure 9.2: Plots of the total magnetization of the system for three phases predicted by the phase diagram, i.e., liquid (1), non-magnetic solid (2) and magnetic solid (3). The magnetization vanishes for cases 1 and 2 but has a finite value for case 3, as the phase diagram predicts.

Figure 9.2 shows the mean magnetization of the system vs. time for the three cases above. The plots show that starting from a random magnetization for the three cases, the magnetization decrease for cases (1) and (2), and eventually the system will have a zero magnetization, as predicted by the phase diagram. The magnetization increases in case (3), and the system eventually will have a finite magnetization. The reason for a non-zero magnetization in this case is that the coefficient of the term $|\mathbf{m}|^2$, i.e., $\left(-3\alpha\phi^2 - 6\beta\phi^2 + r_c - \beta n_0^2\right)$ is negative in this case.

The plots of the final configurations of the density and magnetization for the non-magnetic and magnetic solid are shown in Fig. 9.1. It is important to note that the magnetization field for the non-magnetic solid is almost zero, *i.e.*, of order of 10^{-17}.

9.2 Constant external magnetic field simulations

To confirm the analytical coercivity calculations of Section 8.4 we performed a few simulations by applying constant external magnetic fields in the positive y direction. We choose the density and temperature of the system to be in the magnetic solid state and assumed that the initial mean magnetization of the system is $m_y^0 = -6 \times 10^{-2}$. This value is chosen based on Fig. 8.4.

Before explaining the simulations, it is useful to review the plot of the free energy in the presence of an external magnetic field, shown in Fig. 8.3. The applied magnetic field in $+y$ direction tends to tilt the free energy as in Fig. 8.3(a). If H_y is large enough, it will remove the local minimum of the free energy, as in Fig. 8.3(b)

Since our final goal is to check the grain size dependence of the coercivity, we performed simulations on a single crystal and a two-grain system to examine the difference of the evolution of the magnetization field in two cases. The two-grain system is produced by rotating the hexagonal structure by an angle of $\theta_1 = 21.7867°$, in one grain and $\theta_2 = -21.7867°$ in the other grain. The rotation angle and the $\Delta x = 28\pi/(64\sqrt{3})$ are chosen so that the crystal is perfectly fitted inside the box, to remove any possible mismatching effects. The initial configurations of the single-grain and the two-grain systems are shown in Fig. 9.3.

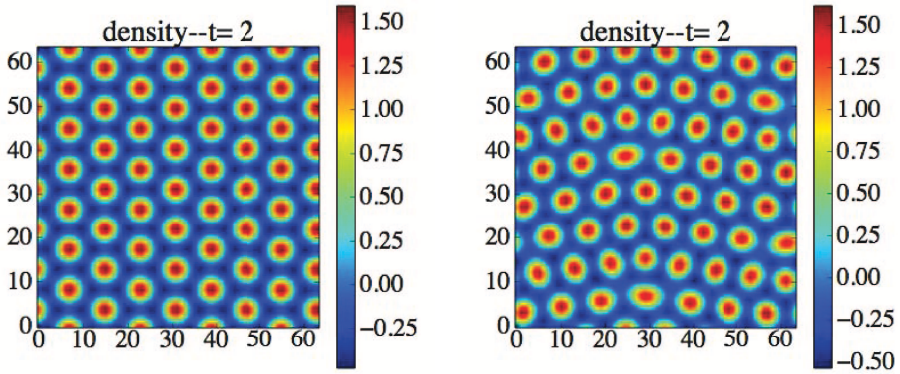

(a) (b)

Figure 9.3: The initial configuration of the system for (a) a single crystal, and (b) for a two-grain system. The boundary divides the system to two vertical grains with $\theta_1 = 21.7867°$ and $\theta_2 = -21.7867°$.

It is expected that the value obtained from the simulations and the value obtained from the analytical calculations to be a bit different. The reason is that the analytical calculations were carried out using the free energy that is calculated by applying the one-mode approximation, while this is not the case for the simulations.

The system size is $l_x = l_y = 64$ and the total number of time-steps is $t_{tot} = 45 \times 10^5$. We first run the simulations with $\mathbf{H} = (0, 0)$ for $t_{rlx} = 10^5$ time-steps and let the system relax, but do not gather any data. Then we apply the external magnetic field and calculate the mean magnetization and energy of the system. The magnetization plots for $\mathbf{H} = (0, 10^{-5})$ and $\mathbf{H} = (0, 5 \times 10^{-4})$ are shown in Fig. 9.4. The magnetic fields are chosen to be close the analytical coercivity $\mathbf{H}_a = (0, 1.5 \times 10^{-4})$, obtained in Section 8.4.

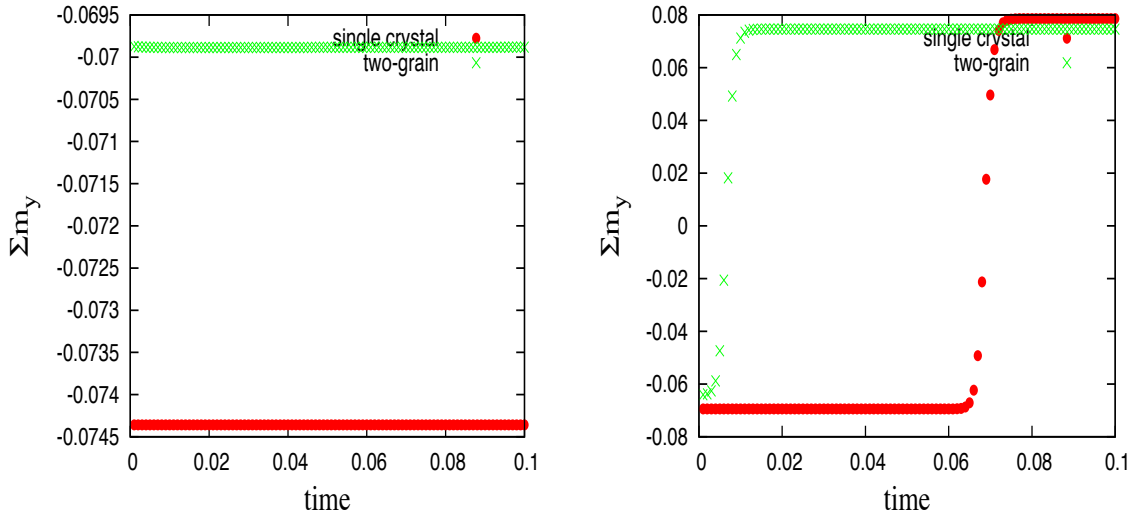

(a) $H = 10^{-5}$ (b) $H = 5 \times 10^{-4}$

Figure 9.4: The plot of the magnetization vs. time for a single crystal and a two-grain system. When the external magnetic field is small, the local minimum in the free energy is not removed and the magnetic moments are captured in the metastable state and the magnetization never becomes positive as in (a). If the magnetic field is large enough it can remove the local minimum of the free energy and eventually the magnetic moments are aligned with the external magnetic field and the mean magnetization of the system becomes positive as shown in (b).

It can be seen in Fig. 9.4(a) that the mean magnetization of the system for $|\mathbf{H}| < |\mathbf{H}_a|$ always remain negative and the magnetic field is not strong enough to change the mean magnetization of the system to a positive value. For $|\mathbf{H}| > |\mathbf{H}_a|$, Fig. 9.4(b) shows that the magnetic field removes the local minimum of the free energy and the system evolves to a positive mean magnetization state.

It is also instructive to compare the magnetization of the single crystal with that of the two-grain system for the two simulations. It can be seen in Fig. 9.4(b) that it takes more time for the single grain system to approach to the positive magnetization state while it is faster for a two-grain system. This means that the grain boundary affects the formation and growth of the domains. This result will be confirmed in Section.9.3, when we apply a periodic external magnetic field. Fig. 9.4(a) show that the equilibrium magnetization of the single crystal has a more negative value relative to that of a two grain system.

The results also show that the run-time of the simulations need to be long enough to give enough time to the magnetic moments to change direction and align with the magnetic field. This should be noted in simulations with a cyclic magnetic field. The frequency of the change in the magnetic field should be low enough to be able to see the change in the sign of the mean magnetization of the system.

9.3 Cyclic magnetic field simulations

In this section the main results obtained from the Magnetic PFC model are discussed. Here we examined the dependence of the magnetic properties of the ferromagnetic material on the microstructure of the material, in particular on the grain size and the grain boundary angle. Our aim is to reproduce the experimental coercivity measurements for magnetic nanocrystalline alloys, presented in Fig. 3.7.

In the following simulations, a cyclic external magnetic field is applied to the system after the system is relaxed for $t_{rlx} = 10^5$ time-steps. For $t > t_{rlx}$, the magnetic field is changed linearly from zero to $\mathbf{H} = (0, 2.5 \times 10^{-4})$, then decreased to $\mathbf{H} = (0, -2.5 \times 10^{-4})$ and finally increased to zero to complete the cycle as in Fig. 9.5. The whole cycle is done in $N = 4 \times 10^5$ time-steps.

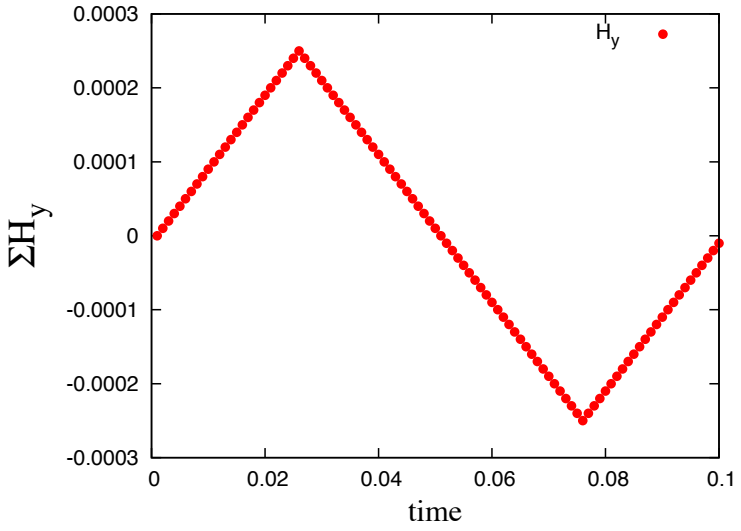

Figure 9.5: Cyclic external magnetic field in y direction with $H_{max} = 2.5 \times 10^{-4}$.

9.3.1 Single crystal and the two-grain system

As discussed in Section 9.2, when we apply a constant magnetic field to the systems, it takes a smaller external magnetic field to remove the local minimum of the free energy in the two-grain system while in the single crystal system a larger magnetic field is needed to remove the local minimum. This implies that the existence of a grain boundary facilitates the formation of the magnetic domains. This is a quite interesting result which can be also explained by considering the free energy of Eq. 8.14. Consulting the equation that determines the Curie line, Eq. 8.17, we see that in the grain boundary for which $\phi = 0$, the temperature at which the ferromagnetism happens is smaller. Therefore the grains are the sites of the system from which the magnetic domains start to from and grow. This difference also affects the hysteresis loops and the coercivities of the two cases and we expect that the two-grain system have a smaller coercivity relative to the single crystal system.

We run simulations, applying a cyclic external magnetic field to a single crystal and a two-grain system, having dimensions $l_x = l_y = 256$, and the hysteresis curves of a single crystal system is compared with that of a two-grain system. The simulations are performed in the magnetic solid phase by choosing the temperature, $\Delta B = 0.02$, and mean density, $n_0 = 0.2$. A cyclic magnetic field similar to Fig. 9.5 is applied to the systems. We prepared the two-grain system as explained in Section 9.2 and the grain boundary is located in the vertical direction similar to Fig. 9.3(b). The hysteresis loops for the two systems are shown in Fig. 9.6 and is in agreement with the predictions.

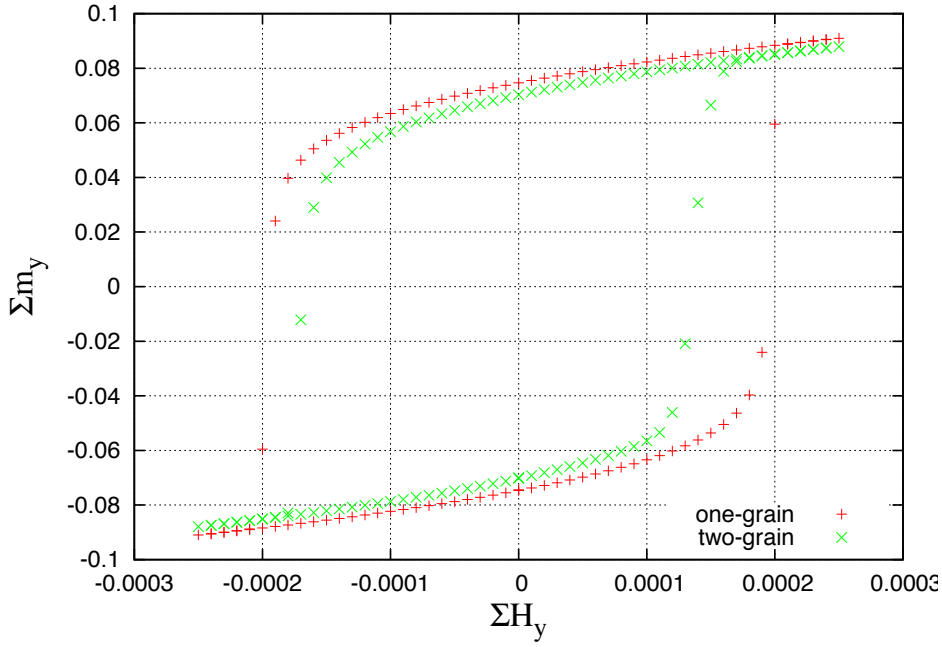

Figure 9.6: Hysteresis curves for a single crystal and a two-grain system.

It is also useful to picture the configurations of the magnetization m_y. The snapshots in Fig9.7 show m_y when the magnetic field is at its maximum $H_y = H_{max}$ and starts to decrease. It can be seen that the regions with smaller magnetization start to form around the grain boundary. This means that the magnetic domains initiate from the grain boundaries and the grain boundaries locally facilitate the formation of the magnetic domains.

9.3.2 Coercivity vs. Grain size simulations

We performed simulations with two-grain systems having a grain boundary angle of $\theta_1 = 21.7867°$, and $\theta_2 = -21.7867°$, in the magnetic solid phase. If the dimensions of the system are $l_x = l_y \equiv l$, then the grain size will be $D \sim l/2$. The parameter W_0 in the free energy was chosen to be 1. This parameter is related the magnetic correlations length or the magnetic exchange length, L_{ex}, in the Random Anisotropy Model (RAM) discussed in Section 3.3 and plays an important role in our arguments. We applied a cyclic magnetic field as shown in

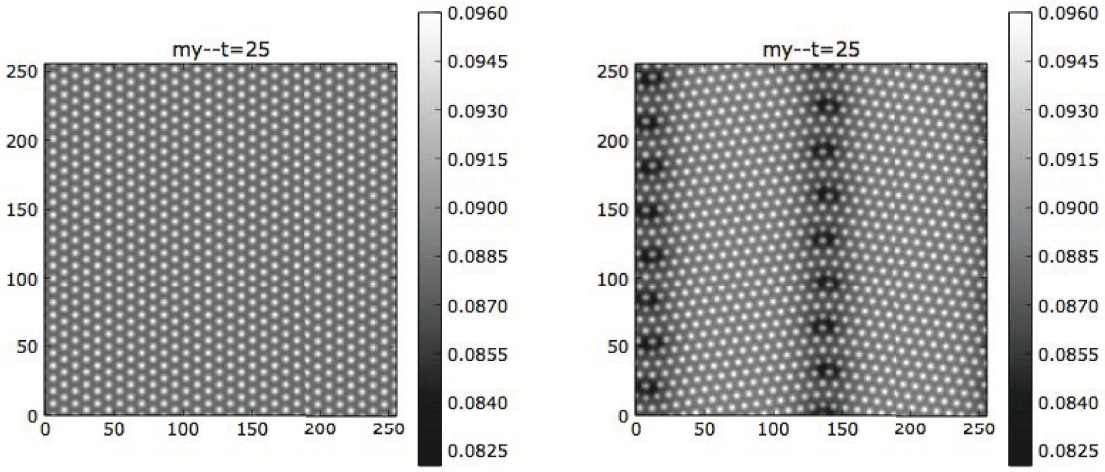

(a) (b)

Figure 9.7: The magnetization m_y configuration for (a) a single crystal, and (b) a two-grain system.

Fig. 9.5. We run the simulations for the following system sizes $l = 32, 64, 128, 256, 512$ and plot the magnetization as a function of the external magnetic field, *i.e.*, the hysteresis loop. The hysteresis plots are shown in Fig9.8.

It is quite interesting to see that the model captures the dependence of the hysteresis loop on the system size, namely, on the grain size. We can read the coercivity values off the hysteresis curves and plot the coercivity as a function of the system size.

As we see in Fig. 9.9(a) the coercivity increases with the system size if $l < 128$, then it starts to decrease as we further increase the system size and the crossover happens at the grain size of about $D_c = l_c/2 = 64$. This result is qualitatively in agreement with the magnetic nanocrystalline materials data of Fig. 3.7. We now show that this crossover size depends on the magnetic correlation length ξ_m which in turn depends on the magnetic exchange length L_{ex}.

As explained in Section 5.1, for a typical LG magnetic free energy similar to Eq. 5.1 the magnetic correlation length ξ_m, can be shown to be equal to [21]

$$\xi_m = \sqrt{\frac{W_0}{2|r|}} \tag{9.1}$$

where r in the Magnetic PFC model is equivalent to $r \equiv -3\alpha\phi^2 - 6\beta\phi^2 + r_c - \beta n_0^2$. We can calculate ϕ_{min}^{PFC} using Eq. 8.16 with $n_0 = 0.2$ and $\Delta B = 0.02$. For $W_0 = 1, \beta = 1/25, \alpha = 10^{-3}$, $r_c = 1/100$ we can calculate the magnetic correlation length to be $\xi_m = 10$ and obtain $D_c/\xi_m = 6.4$. This simulation suggests that for the grain size $D < D_c = 6.4\xi_m$, the domains forming at each boundary start to overlap and average over the anisotropies of the the grains.

We run a similar simulation with $W_0 = 1/4$. Figure 9.9(b) show the coercivity vs. time for this simulation. As the plot shows, the peak shifts to the smaller grain size of $D_c = l_c/2 = 32$ in this case. On the other hand calculation of ξ_m from Eq. 9.1 gives $\xi_m = 5$ in this case. Thus we

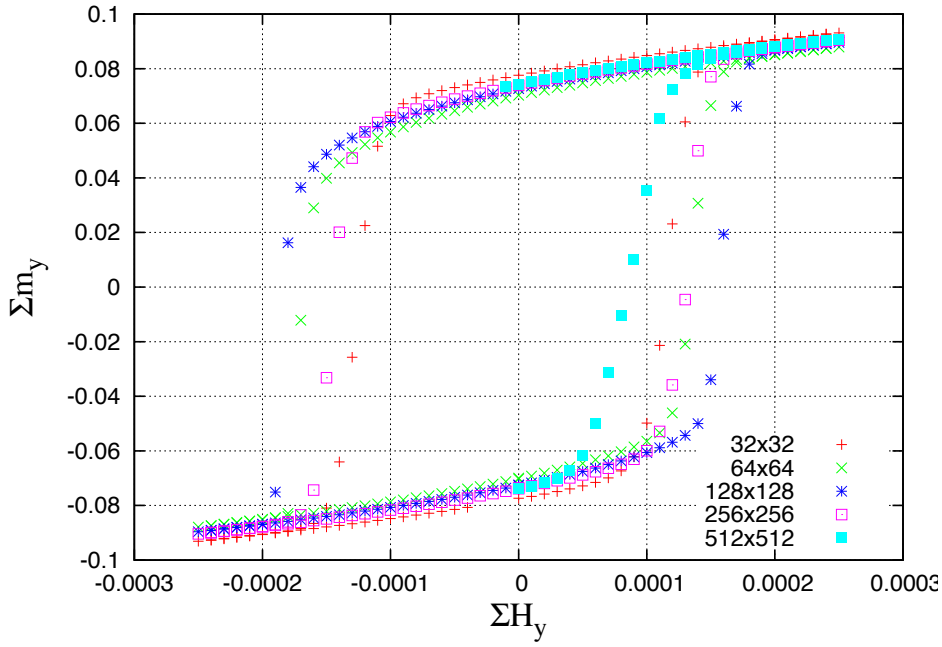

Figure 9.8: Magnetization m_y as a function of the external magnetic field H_y, when the external magnetic field is in y direction with $|H_{max}| = 2.5 \times 10^{-4}$.

again obtain the ratio $D_c/\xi_m = 6.4$ which is consistent with the previous simulation and with the RAM in the sense that a domains with smaller correlation lengths can average over smaller number of grains and therefore the crossover size shifts to smaller values.

This is a remarkable result showing the Magnetic PFC model is a powerful method to study anisotropic magneto-elastic effects. Due to the fact that the Magnetic PFC model incorporates the elastic and magnetic properties of the material in a microscopic level, it is ideal for studying the inter-relation between elasticity, grain, defect and morphological structure of the materials and their magnetic properties in reasonable time and length scales. No other continuum model is capable of studying such phenomena because of the lack of enough temporal and spatial resolution.

9.3.3 Coercivity vs. Grain boundary angle simulations

Simulations were performed for a system of size $l = 256$ an the following grain boundary angles $\theta = 21.7867°, 13.89789°, 10.893363°, 7.31115986°, 3.67041626°$, to check the dependence of the coercivity on the grain boundary angle. Fig. 9.10 shows the plot of the coercivity vs. grain boundary angle. Again we prepared the system including two grains, one rotated by and angle of θ and the other by $-\theta$. The angles are chosen so that the perfect crystal is fitted inside the simulation box, to prevent any change in the energy of the system regarding the boundary effects. This diagram shows that the maximum coercivity occurs for the smallest angle. This result is consistent with the simulations of the Section 9.3.1, and Fig. 9.6, since as

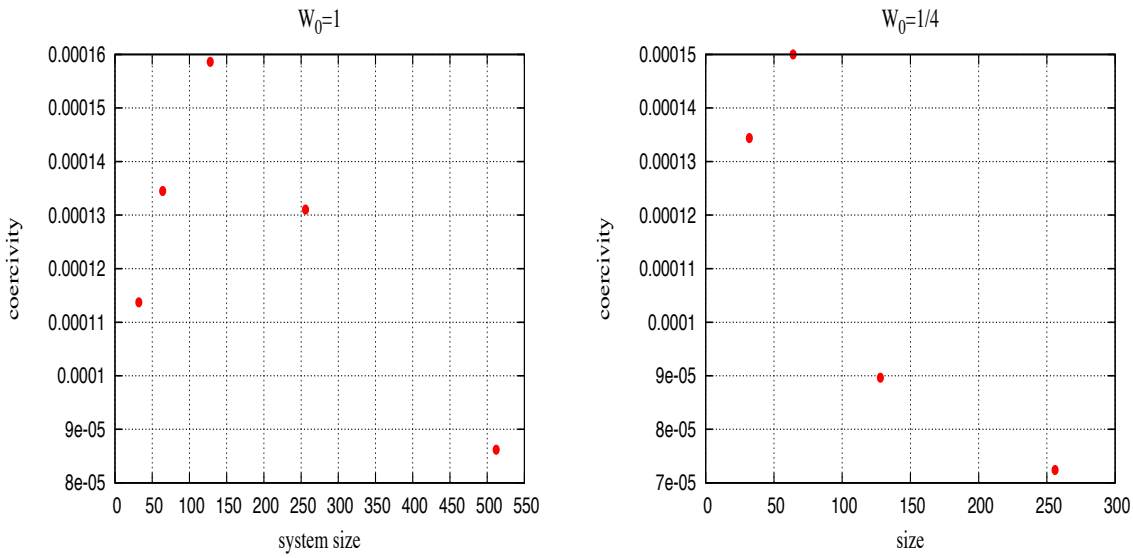

(a) (b)

Figure 9.9: Diagram of the coercivity vs. the size of the system for $W_0 = 1$, (a). It shows that for small system sizes, $l < 128$, the coercivity increases with increasing the grain size. For $l > 12$ the behaviour changes and the coercivity decreases with increasing the system size, and for $W_0 = 1/4$, (b). Here also there is a crossover in the coercivity vs. grain-size data which happens at $l = 64$.

this diagram suggests, the coercivity of a single crystal ($\theta = 0$) is bigger than the coercivity of a two-grain system.

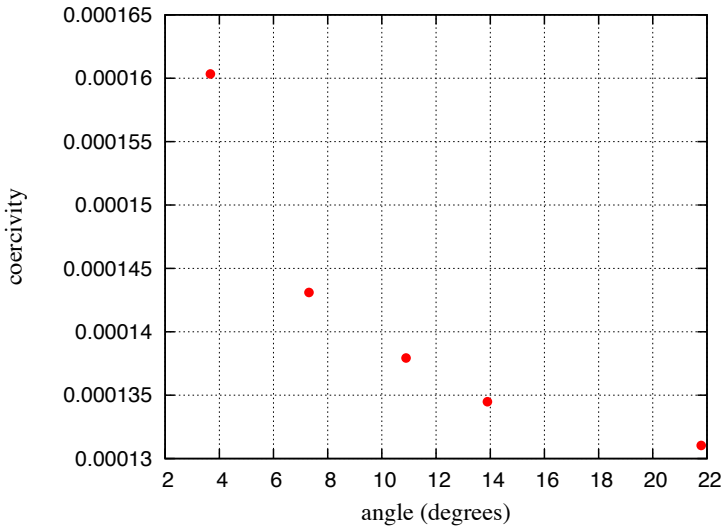

Figure 9.10: Diagram of the coercivity vs. the grain boundary angle for a system of $L = 256$. The coercivity decreases as we increase the grain boundary angle.

Chapter 10

Conclusion

In this work we constructed a new model, the Magnetic Phase Field Crystal Model, to study the interconnection between morphological properties of magnetic solids and their magnetic properties. The free energy we constructed is the minimal free energy which combines the PFC model with the Landau-Ginzburg free energy of ferromagnetic transition, and a coupling terms to link the elastic and magnetic effects. The specific forms of the coupling terms guarantee the ferromagnetic phase transition to occur in the solid phase and result in the anisotropic magnetostriction effects.

The Magnetic PFC free energy, Eq. 7.1, is a phenomenological free energy with a few parameters to be estimated. To estimate the parameters, we connected them to physical measurable quantities and approximate their values in the dimensionless units.

We studied the properties of the model using both analytical arguments and finite difference simulations. The analytical calculations consist of minimizing the free energy and calculating the equilibrium states in the temperature-density plane and evaluating the phase diagram of the model. To minimize the free energy we first estimated it in terms of the amplitudes of the density η_j in the Fourier space, using Eq. 8.2, and assumed that the amplitude in the density expansion varies in space. Evaluating the free energy in terms of the variable amplitudes enables us to study the small elastic deformations of the system via a displacement field $u(\mathbf{r})$ and to calculate the free energy in terms of the strain tensor elements, obtaining Eq. 8.4. This expression for the free energy gives us an insight into the elastic and magnetic effects and their connection, in terms of macroscopic strain tensor.

Since above the Curie temperature the magnetization is zero, the free energy reduces to that of the PFC free energy. On the other hand from experiments, [24], [25], [31], we know that the Curie line lies below the solid-liquid coexistence lines. Therefore the coexistence lines for the Magnetic PFC free energy are similar to the traditional PFC free energy. The only task remaining to completely evaluate the phase diagram is to determine the Curie line in the density-temperature plane. This can be done by applying a similar process used to calculate the Curie temperature in the LG ferromagnetic free energy, Eq. 5.1. The resulting phase diagram is shown in Fig. 8.1, and implies three equilibrium phases, namely, liquid, non-magnetic solid and magnetic solid.

In the next step we considered the magnetostriction effects by examining the coupling term and using the infinitesimal strain theory. We calculated the deformations in a macroscopic ferromagnetic sample by applying an external magnetic field. The schematic deformations are

depicted in Fig. 8.2. As apparent from the figure, for a negative magnetostrictive coefficient, the sample shrinks and for a positive value of the magnetostrictive coefficient, it expands, which is quite reasonable.

The other analytical calculation was to estimate the hysteresis loop of a single crystal which is free from any defect. When an external magnetic field, $+|H|$, is applied to the system having negative mean magnetization $-|m_0|$, the LG ferromagnetic free energy which is symmetric in the absence the magnetic field, Fig. 4.2, becomes unsymmetric under the influence of the external magnetic field as in Fig. 8.3(a). If the magnetic field is large enough, it can tilt the free energy to the extent that one of the local minima completely disappears and only one minima remains, as in Fig. 8.3(b). At this stage the majority of magnetic moments are rotated in the direction of the magnetic field and the positively oriented magnetization "droplet" has filled the system. Existence of the defects can change the mechanism as our simulations show. Based on this picture, we calculated the analytical hysteresis loop of a single crystal by calculating and plotting the roots of Eq. 8.31. The result is shown in Fig. 8.4 and implies that the magnetic field required to remove the local minimum of the free energy is about $\mathbf{H}_a = (0, 1.5 \times 10^{-4})$.

Using finite difference simulations to solve the dynamical equations of motion 7.6-7.8, and the Fast Fourier Transform method to calculate the magnetic field, we confirmed the analytical results obtained in Chapter 8. It should be noted that we do not expect the simulation results to give exactly the same values that the analytical calculations predict. The reason is that to make the analytical calculations possible, we used the single-mode approximation in expanding the density field.

As the first check we produced liquid, non-magnetic solid and magnetic solid using the density and temperatures provided by the analytical phase diagram of the model.

To confirm the analytical hysteresis plot and the value H_a we run simulation with constant magnetic field in the positive direction, with two values of $|\mathbf{H}| < |\mathbf{H}_a|$ and $|\mathbf{H}| > |\mathbf{H}_a|$ and plotted the magnetization for both a single crystal and a two-grain system having a negative mean magnetization, $-|\mathbf{m}_0|$. We observed that if the magnetic field is smaller than $|\mathbf{H}_a|$, the single crystal system does not transfer to the positive magnetization state, but if $|\mathbf{H} > |\mathbf{H}_a|$ it will jump to the positive magnetization state. We also noticed the interesting result that it takes a smaller magnetic field for the two-grain system to make the system transfer to the positive magnetic state, or equivalently the two grain system has a smaller coercivity. This means that the existence of a grain boundary facilitates the formation of the magnetic domains.

To further study this effect, we carried out simulations, applying a periodic magnetic field and studied the hysteresis loop for a single crystal and a two-grain system. We observed that the hysteresis loop has a smaller width for the two-grain system and therefore a smaller coercivity.

The final stage of the simulations are related to the Herzer experiments [27] summarized in Fig. 3.7 and the Random Anisotropy Model schematically depicted in Fig. 3.8. These studies clarified the dependence of the magnetic coercivity to the grain size of the material in ferromagnetic alloys [27]. They observed that for nanocrystalline magnetic alloys with the grain size of $D < 40nm$ the coercivity scales as $H_c \propto D^6$ while for alloys with larger grain size of $D > 150nm$, the coercivity $H_c \propto 1/D$ [29]. They discussed that this change in the behaviour of the alloy happens when the magnetic exchange length L_{ex} becomes comparable to the grain size D. If $L_{ex} > D$, the crystalline anisotropic effects is suppressed and averaged out by the randomly oriented magnetic domains [28]. This results in a smaller coercivity.

It is useful to note that the magnetic exchange length is determined by the parameter W_0 in

the Magnetic PFC model, and is associated with the width of the domain wall. To reproduce the experimental results we run simulations by applying periodic magnetic field to two-grain systems of different sizes of $l_x = l_y = 32, 64, 128, 256, 512$, set $W_0 = 1$ and computed the coercivity. The result is shown in Fig. 9.9(a). It is quite interesting to observe that the simulation results qualitatively reproduce a similar behaviour to the experimental data. For smaller grains, H_c increases when the grain size increases. This behaviour happens for $D < D_c = 64$. Then as the grain size further increases, the coercivity decreases. We run a set of similar simulations with $W_0 = 1/4$ and observed that the crossover in the coercivity-size diagram happens at $D_c = 32$ this time. This means that the when we change W_0 the crossover grain size also changes, as the RAM suggests.

Finally we studied the dependence of the coercivity on the grain boundary angle. The results are summarized in Fig. 9.10. The bigger the grain boundary angle, the smaller the coercivity.

The Magnetic PFC model which was constructed in this research, has essential properties that make it ideal for the subject of this thesis and for other magneto-elastic effects in ferromagnetic materials or (with a minor change) for electro-elastic effects in piezoelectric materials. The advantage of this model is that even though the free energy is written in terms of the coarse-grained order parameters, it still resolves the atomic scales and therefore many properties that originate from microscopic scales, such as elastic and plastic properties, defects and grains are included in this model. The model also averages the order parameters over time, which allows simulations to reach time scales that are necessary to observe the phenomena that happens in diffusive time scales such as diffusion of defects, grain growth and formation of microstructures. These are the distinguishing properties of this model which are not covered in any other model.

The results above imply that it is possible to tune the magnetic properties of ferromagnetic materials by modifying their microstructures, namely the grain size and the grain boundary angle. This is a quite interesting and significant result since due to a wide range of applications of soft magnetic materials in today's electrical engineering and electronics, it is important to engineer and optimize them for their special application they are selected for.

In this research we focused on the effect of the morphology on the magnetic properties. It is however known that the magnetic ordering can also affect the nucleation behaviour and therefore the morphology of the meterial [31]. For all known ferromagnetic materials the melting temperature is much higher than the Curie temperature [26]. The first observation of magnetic ordering in liquid phase in undercooled Co-based melts was reported in [3]. More experimental observations in Co-Pd alloys and calculation of the Gibbs free energy of nucleation showed that the magnetic phase transformation is coupled with the liquid-solid transition by a magnetic contribution to the free energy and therefore it is possible to facilitate the nucleation [31] by applying a magnetic field to the undercooled Co-Pd melts.

There is really a mutual relationship between morphological and elastic properties and magnetic properties of materials. A possible future work can be to use the Magnetic PFC model to consider the effect discussed by Herlach *et.al*..

Bibliography

[1] T. Ala-Nissila, S. Majaniemi, and K. Elder. Phase-field modeling of dynamical interface phenomena in fluids. In M. Karttunen, I. Vattulainen, and A. Lukkarinen, editors, *Novel Methods in Soft Matter Simulations*, pages 357–384. Springer-Verlag Berlin Heidelberg, 2004.

[2] R. Alben, J. J. Becker, and M. C . Chi. Random anisotropy in amorphous ferromagnets. *J. Appl. Phys.*, 49:1653–1658, 1978.

[3] T. Albrecht, C. Buhrer, M. Fahnle, K. Maier, D. Platzek, and J. Reske. First observation of ferromagnetism and ferromagnetic domains in a liquid. *Appl. Phys. A*, 65:215–220, 1997.

[4] N. W. Ashcroft and N. D. Mermin. *Solid States Physics*. Harcourt College Publishers, Orlando, FL, 1976.

[5] W. G. Bickley. Finite difference formulae for the square lattice. *Q. J. Mechanics Appl. Math.*, 1:35–42, 1948.

[6] J. J. Binney, N. J. Dowrick, A. J. Fisher, and M. E. J. Newman. *The Theory of Critical Phenomena*. Oxford University Press, New York, 1992.

[7] W.J. Boettinger, J. A. Warren, C. Beckermann, and A. Karma. Phase field simulations of solidification. *Ann. Rev. Mater. Res.*, 32:163–194, 2002.

[8] D. Boyer and J. Vinals. Weakly nonlinear theory of grain boundary motion in patterns with crystalline symmetry. *Phys. Rev. Lett.*, 89:055501, 2002.

[9] W. F. Brown. Magnetic materials. In E. U. Condon and H. Odishaw, editors, *Handbook of Physics*, chapter 8. McGraw-Hill, New York, 1958.

[10] J. W. Cahn and J. E. Hilliard. Free energy of a nonuniform system. i. interfacial free energy. *J. Chem. Phys.*, 28:258–267, 1958.

[11] B. Caroli, C. Caroli, and B. Roulet. Instabilities of planar solidification fronts. In C. Godreche, editor, *Solids Far From Equilibrium*, chapter 2. Cambridge University Press, Cambridge, 1983.

[12] P. M. Chaikin and T. C Lubensky. *Principles of Condensed Matter Physics*. Cambridge University Press, Cambridge, 2000.

[13] M. C. Chi and R. Alben. Hysteresis curves and magnetization processes in a model for an amorphous magnet with random uniaxial anisotropy. *J. Appl. Phys.*, 48:1653–1658, 1977.

[14] B. D. Cullity. *Introduction to Magnetic Materials*. Addison-Wesley Publishing Company, Inc., USA, 1972.

[15] A. Einstein. *Ann. d. Physik*, 17:549–560, 1905.

[16] K. R. Elder and M. Grant. Modeling elastic and plastic deformations in nonequilibrium processing using phase field crystals. *Phys. Rev. E*, 70:051605, 2004.

[17] K. R. Elder, M. Grant, N. Provatas, and J. M. Kosterlitz. Sharp interface limits of phase-field models. *Phys. Rev. E*, 64:021604, 2001.

[18] K. R. Elder, M. Katakowski, M. Haataja, and M. Grant. Modeling elasticity in crystal growth. *Phys. Rev. Lett.*, 88:245701, 2002.

[19] K. R. Elder, N. Provatas, J. Berry, P. Stefanovic, and M. Grant. Phase-field crystal modeling and classical density functional theory of freezing. *Phys. Rev. B*, 75:064107, 2007.

[20] Wikipedia: The free Encyclopedia. Hard disk drive, May 2012.

[21] N. Goldenfeld. *Lectures on Phase Transitions and the Renormalization Group*. Addison-Wesley Publishing Company, Reading, MA, 1992.

[22] O. Gutfleisch, M. A. Willard, E. Bruck, C. H. Chen, S. G. Sankar, and J. P. Liu. Magnetic materials and devices for the 21st century: stronger, lighter and more energy efficient. *Adv. Mater.*, 23:821–842, 2011.

[23] C. Harrison, H. Adamson, Z. Cheng, J. M. Sebastian, S. Sethuraman, D. A. Huse, R. A. Register, and P. M. Chaikin. Mechanisms of ordering in striped patterns. *Science*, 290:1558–1560, 2000.

[24] D. Herlach, C. Buhrer, D. M. Herlach, K. Maier, C. Notthoff, D. Platzek, and J. Reske. Magnetic ordering in a suprecooled po-pd melt studied by muon-spin rotation. *Europhys. Lett.*, 44:98–102, 1998.

[25] D. M. Herlach. Metastable materials solidified from undercooled melts. *J. Phys.: Condens. Matter*, 13:7737–7751, 2001.

[26] D. M. Herlach, D. Holland-Moritz, R. Willnecker, D. Herlach, and K. Maier. Magnetic ordering and crystal nucleation in undercooled co-based melts. *Phil. Trans. R. Soc. Lond. A*, 361:497–515, 2007.

[27] G. Herzer. Grain six dependence and permeability in nanocrystalline ferromagnetis. *IEEE Trans. Magn.*, 26:1397–1402, 1990.

[28] G. Herzer. Nanocrystalline soft magnetic materials. *Phys. Scr.*, T49A:307–314, 1993.

[29] G. Herzer. Nanocrystalline soft magnetic alloys. In K. H. J. Buschow, editor, *Handbook of Magnetic Materials*, volume 10, chapter 3. Elsevier Science B.V., 1997.

[30] P. C. Hohenberg and B. I. Halperin. Theory of dynamic critical phenomena. *Rev. Mod. Phys.*, 49:435–479, 1977.

[31] D. Holland-Moritz, D. M. Herlach, and F. Spaepen. Crystal nucleation induced by magnetic ordering in undercooled melts. *Superlattice Microst.*, 41:196–203, 2003.

[32] A. Jaatinen, C.V. Achim, K. R. Elder, and T. Ala-Nissila. Thermodynamics of bcc metals in phase-fied-crystal models. *Phys. Rev. E*, 80:031602, 2009.

[33] J. D. Jackson. *Classical Electrodynamics*. John Wiley and Sons Inc., New York, 1998.

[34] R. A. L. Jones. *Soft Condensed Matter*. Oxford University Press, New York, 2002.

[35] M. Kardar. *Statistical Physics of Fields*. Cambridge University Press, New York, 2007.

[36] C. Kittle. Physical theory of ferromagnetic domains. *Rev. Mod. Phys.*, 21:541–583, 1949.

[37] C. Kittle. *Introduction to Solid State Physics*. John Wiley Sons Inc., New York, 1986.

[38] T. Koyama. Phase-field modeling of microstructure evolutions in magnetic materials. *Sci. Technol. Adv. Mater.*, 9:013006, 2008.

[39] T. Koyama and H. Onodera. Modeling of microstructure changes in fe-cr-co magnetic alloy using the phase-field method. *J. Phase Equilib. Diff.*, 27:22–29, 2006.

[40] R. Kubo. The fluctuation-dissipation theorem. *Rep. Prog. Phys*, 29:255–284, 1966.

[41] L. D. Landau and E. M. Lifshitz. *Statistical Physics, Part 1*. Pergamon Press Ltd., Oxford, 1980.

[42] L. D. Landau, E. M. Lifshitz, and L. P. Pitaevskii. *Electrodynamics of Continuous Media*, volume 8. Elsevier Pte Ltd., Singapore, 2007.

[43] J. S. Langer. Instabilities and pattern formation in crystal growth. *Rev. Mod. Phys.*, 52:1–28, 1980.

[44] J. S. Langer. Viscous fingers and theory of pattern formation. *science*, 243:1150–1156, 1989.

[45] M. Laradij, H. Guo, M. Grant, and M. J. Zuckermann. Phase diagram of a lattice model for ternary mixtures of water, oil, and surfactants. *Phys. Rev. A*, 44:8184–8188, 1991.

[46] M. E. McHenry and D. E. Laughlin. Nano-scale materials development for future magnetic applications. *Acta Mater.*, 48:223–238, 2000.

[47] J. Muller. *Study of Stress-Induced Morphological Instabilities*. PhD thesis, McGill University, 1998.

[48] J. Muller and M. Grant. Model of surface instabilities induced by stress. *Phys. Rev. Lett*, 82:1736–1739, 1999.

[49] W. W. Mullins and R. F. Sekerka. Morphological instability of a particle growing by diffusion or heat flow. *J. Appl. Phys.*, 34:323–329, 1963.

[50] T. Murtola, A. Bunker, I. Vattulainen, M. Desemo, and M. Karttunen. Multiscale modelling of emergent materials: biological and soft matter. *Phys. Chem. Chem. Phys.*, 11:1869–1892, 2009.

[51] A. Onuki. *Phase Transition Dynamics*. Cambridge University Press, Cambridge, 2004.

[52] M. Patra and M. Karttunen. Stencils with isotropic discretization error for differential perators. *Num. Meth. Part. Diff. Eqs*, 22:936–953, 2005.

[53] W. H. Press, S. A. Teukolsky, W. T. Vetterling, and B. P. Flannery. *Numerical Recipes in Fortran 77: The Art of Scientific Computing*. Cambridge University Press, 2001.

[54] N. Provatas and K. Elder. *Phase Field Methods in Material Science and Engineering*. Wiley-VCH, 2010.

[55] T. V. Ramakrishan and M. Yussouff. First-principles order-parameter theory of freezing. *Phys. Rev. B*, 19:2775, 1979.

[56] S. Safran. *Statistical Thermodynamics Of Surfaces, Interfaces, And Membranes*. Westview Press, Boulder, CO, 2003.

[57] C. Sagui and R. C. Desai. Late-stage kinetics of systems with competing interactions quenched into the hexagonal phase. *Phys. Rev. E*, 52:2807–2821, 1995.

[58] J. J. Sakurai. *Modern Quantum Mechanics*. Addison-Wesley Publishing Company, Inc., USA, 1994.

[59] F. Seitz. *The Modern Theory of Solids*. McGraw-Hill Book Company, Inc., 1940.

[60] N. Spaldin. *Magnetic Materials, Fundamentals and Device Applications*. Cambridge University Press, Cambridge, UK, 2003.

[61] J. C. Strikwerda. *Finite Difference Schemes and Partial Differential Equations*. Society for Industrial and Applied Mathematics, USA, 2004.

[62] S. Timoshenko and J. N. Goodier. *Theory of Elasticity*. McGraw-Hill Book Company, 1951.

[63] P. F. Tupper and M. Grant. Phase field crystals as a coarse-graining in time of molecular dynamics. *Europhys. Lett.*, 81:40007, 2008.

Appendix A

Derivation of the vector potential equation and the equations of motion

In this appendix we discuss the details of calculations that we skipped in Chapter 7. These details include the derivation of the free energy of the magnetic field inside a ferromagnetic material, and the derivation of the equations of motion.

A.1 Poisson equation derivation for the vector potential

To derive the Poisson equation (in the *SI* system) for the vector potential, $\mathbf{A}$, we note that all magnetic effects due to the matter can be described in terms of the magnetization, $\mathbf{m}$, defined by Eq. 2.1. From the differential form of the *Ampere's law* [33], we can calculate the magnetic field due to the *free current density*, $\mathbf{J}_f$, arising from the actual moving charges. Ampere's law states that

$$\nabla \times \mathbf{H} = \mathbf{J}_f. \tag{A.1}$$

Using Eq. 2.2, we can calculate the magnetic induction, $\mathbf{B}$, inside the material in terms of the free current density, $\mathbf{J}_f$, and the magnetization, $\mathbf{m}$

$$\nabla \times (\frac{1}{\mu_0}\mathbf{B} - \mathbf{m}) = \mathbf{J}_f, \tag{A.2}$$

or

$$\nabla \times \mathbf{B} = \mu_0(\mathbf{J}_f + \nabla \times \mathbf{m}). \tag{A.3}$$

The last term in this equation is associated with the magnetic field due to the non-zero magnetization in a ferromagnetic material. The term $\mathbf{J}_M = \nabla \times \mathbf{m}$ is called the *magnetization current density*. The magnetic induction $\mathbf{B}$ in this equation is the total magnetic induction caused by free current density, $\mathbf{J}_f$, and induced by the magnetization current density, $\mathbf{J}_M$. We can write

$$\nabla \times (\mathbf{B}_{ext} + \mathbf{B}_{ind}) = \mu_0\mathbf{J}_f + \mu_0\nabla \times \mathbf{m}. \tag{A.4}$$

Assuming that $\mathbf{B}_{ext}$ is a known quantity, *i.e.*, assuming that we know the value of the external magnetic field applied to the material, we need to solve

$$\nabla \times \mathbf{B}_{ind} = \mu_0 \nabla \times \mathbf{m}, \tag{A.5}$$

to calculate $\mathbf{B}_{ind}$. Inserting $\mathbf{B}_{ind}$ from Eq. 7.4 into Eq. A.5 we get

$$\nabla \times \nabla \times \mathbf{A} = \mu_0 \nabla \times \mathbf{m}. \tag{A.6}$$

Using the formula [33]

$$\nabla \times \nabla \times F = \nabla \nabla \cdot F - \nabla^2 F, \tag{A.7}$$

we can rewrite Eq. A.6 as

$$\nabla \nabla \cdot \mathbf{A} - \nabla^2 \mathbf{A} = \mu_0 \nabla \times \mathbf{m}. \tag{A.8}$$

In the *Coulomb gauge* it is assumed that $\nabla \cdot \mathbf{A} = 0$. Thus we obtain the Poisson equation, 7.5

$$\nabla^2 \mathbf{A} = -\mu_0 \nabla \times \mathbf{m}. \tag{A.9}$$

It should be mentioned that assuming that $\nabla \cdot \mathbf{A} = 0$ allows us to simplify the equation for the vector potential without a loss of the generality of the problem. This means that by restricting the vector potential to satisfy this equation, the Maxwell equations will still be satisfied. With this choice we eliminate the arbitrariness involved in the definition of the vector potential. Since $\mathbf{B}$ is defined through Eq. 7.4, the vector potential is arbitrary to the extent that the gradient of some scalar function Λ can be added [33], that is, the magnetic field is unchanged if $\mathbf{A} \rightarrow \mathbf{A} + \nabla\Lambda$. The choice for the divergence of the vector potential specifies $\mathbf{A}$ completely. The particular choice, $\nabla \cdot \mathbf{A} = 0$ has the advantage that it simplifies the equation for calculating $\mathbf{A}$ and reduces it to the well-known Poisson equation.

A.2 Derivation of the equations of motion

To derive the equations of motion we use the functional derivative formulas [6]

$$\begin{aligned} \frac{\delta F[\rho]}{\delta \rho} &= \frac{\partial f}{\partial \rho} - \nabla \cdot \frac{\partial f}{\partial (\nabla \rho)} + \nabla^2 \cdot \frac{\partial f}{\partial (\nabla^2 \rho)} + ... + (-1)^n \nabla^n \cdot \frac{\partial f}{\partial (\nabla^N \rho)} \\ &= \sum_{i=0}^{N} (-1)^i \nabla^i \cdot \frac{\partial f}{\partial (\nabla^i \rho)}. \end{aligned} \tag{A.10}$$

For example using this formula, the equation of motion for the terms

$$F_1 = \frac{n}{2}(\Delta B + B_s\Big(1 + \nabla^2)^2\Big)n - t\frac{n^3}{3} + v\frac{n^4}{4}, \tag{A.11}$$

will be

$$\begin{aligned} \frac{\delta F_1}{\delta n} &= \frac{\delta}{\delta n}(\Delta B \frac{n^2}{2} + \frac{n}{2}\Big(B_s(1 + 2\nabla^2 + \nabla^4)n\Big) - t\frac{n^3}{3} + v\frac{n^4}{4}) \\ &= (\Delta B + B_s)n + 2B_s\nabla^2 n + B_s\nabla^4 n - tn^2 + vn^3 \\ &= \Big(\Delta B + B_s(1 + \nabla^2)^2\Big)n - tn^2 + vn^3. \end{aligned} \tag{A.12}$$

Calculations of the functional derivatives for the rest of the terms can be done similarly.

The last term in each of Eqs. 7.7, and Eq.7.8, ($\mathbf{B}_x$, $\mathbf{B}_y$), can be obtained starting from the free energy, $F_{\mathbf{B}}$

$$W_m = W_1 + W_2 = \frac{1}{2\mu_0}\int \mathbf{B}^2 d\mathbf{r} - \frac{1}{2\mu_0}\int \mathbf{m}\cdot\mathbf{B} d\mathbf{r}. \tag{A.13}$$

To calculate $\delta W_m/\delta\mathbf{m}$, we consider W_1 and W_2 separately.

To calculate $\delta W_1/\delta\mathbf{m}$ we note that a change in the magnetization, as $\mathbf{m} \to \mathbf{m} + \delta\mathbf{m}$ results in a change in the magnetic field as $\mathbf{B} \to \mathbf{B} + \delta\mathbf{B}$. As a result $\mathbf{B}^2 \to \mathbf{B}^2 + 2\mathbf{B}\cdot\delta\mathbf{B}$. Inserting $\mathbf{B}$ from Eq. 7.4 gives

$$\begin{aligned} W_1[\mathbf{m}+\delta\mathbf{m}] &= W_1[\mathbf{m}] + \frac{1}{\mu_0}\int (\nabla\times\mathbf{A})\cdot\delta\mathbf{B} d\mathbf{r} \\ &= W_1[\mathbf{m}] + \frac{1}{\mu_0}\int \nabla\cdot(\mathbf{A}\times\delta\mathbf{B}) d\mathbf{r} + \frac{1}{\mu_0}\int \mathbf{A}\cdot(\nabla\times\delta\mathbf{B}) d\mathbf{r}. \end{aligned} \tag{A.14}$$

The second term in the right hand side of Eq. A.14 is zero since it is a surface term (using the divergence theorem) and assuming periodic boundary condition for the density field also gives rise in periodic structure for the magnetic field and this term becomes zero. Using Eq. A.5 we get $\nabla\times\delta\mathbf{B} = \mu_0\nabla\times\delta\mathbf{m}$, and we can write Eq. A.14 as

$$\begin{aligned} \delta W_1 &= \int \mathbf{A}\cdot(\nabla\times\delta\mathbf{m}) d\mathbf{r} \\ &\int (\nabla\times\mathbf{A})\cdot\delta\mathbf{m} d\mathbf{r} + \int \nabla\cdot(\mathbf{A}\times\delta\mathbf{m}) d\mathbf{r} \\ &= \int \mathbf{B}\cdot\delta\mathbf{m} d\mathbf{r}. \end{aligned} \tag{A.15}$$

This gives

$$\frac{\delta W_1[\mathbf{m}]}{\delta\mathbf{m}} = \mathbf{B}. \tag{A.16}$$

Under a change in the magnetization, $\mathbf{m} \to \mathbf{m} + \delta\mathbf{m}$, the integrand in the second term, W_2, changes to $\mathbf{m}\cdot\mathbf{B} \to \mathbf{m}\cdot\mathbf{B} + \mathbf{m}\cdot\delta\mathbf{B} + \mathbf{B}\cdot\delta\mathbf{m}$. Inserting it into W_2, we get

$$W_2[\mathbf{m}+\delta\mathbf{m}] = W_2[\mathbf{m}] + \int \mathbf{m}\cdot\delta\mathbf{B} d\mathbf{r} + \int \mathbf{B}\cdot\delta\mathbf{m} d\mathbf{r}. \tag{A.17}$$

Using Eq. 7.4, we can write

$$\begin{aligned} \int \mathbf{m}\cdot\delta\mathbf{B} &= \int \mathbf{m}\cdot(\nabla\times\delta\mathbf{A}) d\mathbf{r} \\ &\int (\nabla\times\mathbf{m})\cdot\delta\mathbf{A} d\mathbf{r} + \int \nabla\cdot(\mathbf{m}\times\delta\mathbf{A}) d\mathbf{r}. \end{aligned} \tag{A.18}$$

The second term on the right hand side of this equation is a surface term and vanishes. Using Eq. 7.5, the first term on the right hand side becomes

$$\begin{aligned}\int (\nabla \times \mathbf{m}) \cdot \delta\mathbf{A} d\mathbf{r} &= -\frac{1}{\mu_0} \int \nabla^2 \mathbf{A} \cdot \delta\mathbf{A} d\mathbf{r} \\ &= -\frac{1}{\mu_0} \int \mathbf{A} \cdot \nabla^2(\delta\mathbf{A}) d\mathbf{r}.\end{aligned} \tag{A.19}$$

The last line in this equation is obtained by integrating by parts and vanishing the surface term. Using Eq. 7.5 we can write $\nabla^2(\delta\mathbf{A}) = -\mu_0(\nabla \times \delta\mathbf{m})$. Inserting this into Eq. A.18 we obtain

$$\begin{aligned}\int (\nabla \times \mathbf{m} \cdot \delta\mathbf{A} d\mathbf{r}) &= \int \mathbf{A} \cdot (\nabla \times \delta\mathbf{m}) d\mathbf{r} \\ &= \int \mathbf{B} \cdot \delta\mathbf{m} d\mathbf{r},\end{aligned} \tag{A.20}$$

where in the last line, we again set the surface term equal to zero. Substituting this equation into Eq. A.17 we obtain

$$W_2[\mathbf{m} + \delta\mathbf{m}] = W_2[\mathbf{m}] + 2 \int \mathbf{B} \cdot \delta\mathbf{m} d\mathbf{r}. \tag{A.21}$$

It is easily seen that

$$\frac{\delta W_2[\mathbf{m}]}{\delta\mathbf{m}} = 2\mathbf{B}. \tag{A.22}$$

Using this equation together with Eq. A.16 we obtain

$$-\frac{\delta W_m[\mathbf{m}]}{\delta\mathbf{m}} = -(\mathbf{B} - 2\mathbf{B}) = \mathbf{B}. \tag{A.23}$$

Appendix B

Amplitude expansion and elastic deformation calculations

In this appendix we explain how to obtain Eq. 8.3 from the Magnetic PFC free energy, Eq. 7.1, exploiting the amplitude expansion method and evaluating the integrals. Then we calculate the free energy when the system is elastically deformed, to obtain Eq. 8.4.

B.1 Amplitude expansion

We consider the different terms of the free energy, separately. By substituting the amplitude expansion of the density, Eq. 8.2, into the free energy Eq. 7.1, and integrating over the space, we obtain the free energy in terms of the amplitudes, η_j.

B.1.1 The PFC part of the free energy - F_{pfc}

Let us start with f_{pfc}

$$f_{pfc} = n\Big(\Delta B + B_s(1+\nabla^2)^2\Big)\frac{n}{2} - t\frac{n^3}{3} + v\frac{n^4}{4}, \tag{B.1}$$

and first perform the calculations for the first bracket in this equation

$$f^{(1)}_{pfc} = n\Big(\Delta B + B_s(1+\nabla^2)^2\Big)\frac{n}{2}, \tag{B.2}$$

We substitute $n = n_0 + \sum_j \eta_j e^{i\mathbf{q}_j\cdot\mathbf{r}} + C.C$ into Eq. B.2 and use the Einstein convention[1] to denote the derivatives. Considering the term

$$f^{(1)}_{pfc} = (n_0 + \eta_j e^{i\mathbf{q}_{ji}r_i} + C.C)\Big(\Delta B + B_s(1+\partial_k^2)^2\Big)(n_0 + \eta_j e^{iq_{ji}r_i} + C.C.), \tag{B.3}$$

[1] According to this convention, when an index variable appears twice in one term it implies a summation of that term over all the possible values of the index.

we can calculate the derivatives using the fact that $\partial_k r_j = \delta_{kj}$, where δ_{kj} is the Kronecker delta. Let us calculate the terms that appear in $f^{(1)}_{pfc}$. First we consider the term

$$\begin{aligned}
\partial_k^2(n_0 + \eta_j e^{iq_{ji}r_i}) &= \partial_k^2(\eta_j e^{iq_{ji}r_i}) \\
&= \partial_k\Big[(\partial_k\eta_j)e^{iq_{ji}r_i} + \eta_j(\partial_k e^{iq_{ji}r_i})\Big] \\
&= \partial_k\Big[(\partial_k\eta_j)e^{iq_{ji}r_i} + iq_{ji}\eta_j(\partial_k r_i)e^{iq_{ji}r_i}\Big] \\
&= \Big[(\partial_k^2\eta_j)e^{iq_{ji}r_i} + iq_{ji}\partial_k(\eta_j\delta_{ki}e^{iq_{ji}r_i})\Big] \\
&= (\partial_k^2\eta_j)e^{iq_{ji}r_i} + iq_{ji}\partial_k\eta_j\delta_{ki}e^{iq_{ji}r_i} \\
&+ iq_{ji}(\partial_k\eta_j)\delta_{ki}e^{iq_{ji}r_i} + iq_{ji}\eta_j(\delta_{ki})^2e^{iq_{ji}r_i},
\end{aligned} \tag{B.4}$$

noting that $\delta_{ki}^2 = 1$ and re-writing in the ∇ notation, we obtain

$$\partial_k^2(n_0 + \eta_j e^{iq_{ji}r_i}) = \Big[(\nabla^2\eta_j) + 2i(\nabla\eta_j)\cdot\mathbf{q}_j - \eta_j\Big]e^{i\mathbf{q}_j\cdot\mathbf{r}}, \tag{B.5}$$

where we have used the fact that the reciprocal lattice vectors $\mathbf{q}_j$ satisfy the relation $|\mathbf{q}_j|^2 = 1$. using the notation $\mathcal{G}_j \equiv \nabla^2 + 2i\mathbf{q}_j\cdot\nabla$, yields

$$\partial_k^2(n_0 + \eta_j e^{iq_{ji}r_i}) = (\mathcal{G}_j - 1)\eta_j e^{i\mathbf{q}_j\cdot\mathbf{r}}. \tag{B.6}$$

Similarly for the complex conjugate term in Eq. B.3, we can show that

$$\partial_k^2(n_0 + \eta_j^* e^{-iq_{ji}r_i}) = (\mathcal{G}_j^* - 1)\eta_j^* e^{-i\mathbf{q}_j\cdot\mathbf{r}}, \tag{B.7}$$

where $\mathcal{G}_j^*$ is the complex conjugate of $\mathcal{G}_j$. Thus

$$\nabla^2 n = \sum_j\Big[(\mathcal{G}_j - |\mathbf{q}_j|^2)\eta_j e^{i\mathbf{q}_j\cdot\mathbf{r}} + (\mathcal{G}_j^* - 1)\eta_j^* e^{-i\mathbf{q}_j\cdot\mathbf{r}}\Big]. \tag{B.8}$$

Here we make an approximation [54], by assuming that the amplitudes are constant over one unit cell. Using this approximation we can integrate the free energy density f_{pfc}, over one unit cell, ignoring the spatial dependence of η_j. To calculate the final expression of the free energy we need to integrate the the terms that already averaged on the unit cell, over the whole space.

Multiplying Eq. B.8 by n and integrate over the unit cell to obtain

$$\begin{aligned}
\int n\nabla^2 n d\mathbf{r} &= \int\Big\{\Big[n_0 + \sum_j\Big(\eta_j e^{i\mathbf{q}_j\cdot\mathbf{r}} + \eta_j^* e^{-i\mathbf{q}_j\cdot\mathbf{r}}\Big)\Big]\Big[\sum_k\Big((\mathcal{G}_k - 1)\eta_k e^{i\mathbf{q}_k\cdot\mathbf{r}} + (\mathcal{G}_k^* - 1)\eta_k^* e^{-i\mathbf{q}_k\cdot\mathbf{r}}\Big)\Big]\Big\}d\mathbf{r} \\
&= \int\Big\{n_0\sum_k\Big[(\mathcal{G}_j - 1)\eta_j e^{i\mathbf{q}_j\cdot\mathbf{r}} + (\mathcal{G}_k^* - 1)\eta_k^* e^{-i\mathbf{q}_k\cdot\mathbf{r}}\Big] \\
&+ \Big[\sum_{j\neq k}\Big(\eta_j e^{i\mathbf{q}_j\cdot\mathbf{r}} + \eta_j^* e^{-i\mathbf{q}_j\cdot\mathbf{r}}\Big)\Big]\Big[\sum_k\Big((\mathcal{G}_k - 1)\eta_k e^{i\mathbf{q}_k\cdot\mathbf{r}} + (\mathcal{G}_k^* - 1)\eta_k^* e^{-i\mathbf{q}_k\cdot\mathbf{r}}\Big)\Big] \\
&+ \Big[\sum_{j=k}\Big(\eta_j e^{i\mathbf{q}_j\cdot\mathbf{r}} + \eta_j^* e^{-i\mathbf{q}_j\cdot\mathbf{r}}\Big)\Big]\Big[\sum_k\Big((\mathcal{G}_k - 1)\eta_k^* e^{i\mathbf{q}_k\cdot\mathbf{r}} + (\mathcal{G}_k^* - 1)\eta_k^* e^{-i\mathbf{q}_k\cdot\mathbf{r}}\Big)\Big]\Big\}d\mathbf{r} \\
&= \sum_j|\eta_j|^2\Big(\mathcal{G}_j^* + \mathcal{G}_j - 2\Big),
\end{aligned} \tag{B.9}$$

where the last line is obtained using the fact that the terms containing the periodic functions $\sin(\mathbf{q}_k \cdot \mathbf{r})$ and $\cos(\mathbf{q}_k \cdot \mathbf{r})$ become zero when integrated over one period. The only nonzero terms are obtained when $j = k$ since the exponential term $\exp[i(\mathbf{q}_j - \mathbf{q}_k) \cdot \mathbf{r}]$ is zero and the integral does not vanish.

Calculation of the integral of the term $n\nabla^4 n$ is straightforward. To evaluate this integral we use

$$\int n\nabla^4 n d\mathbf{r} = \int \left(\nabla^2 n\right)^2 d\mathbf{r}. \tag{B.10}$$

To justify it, we use the Green's second identity[2]. Substituting $\phi \equiv n$ and $\psi \equiv \nabla^2 n$ into the Green's second identity we get

$$\int_V \left[n\nabla^2\left(\nabla^2 n\right) - \left(\nabla^2 n\right)\left(\nabla^2 n\right)\right] d\mathbf{r} = \oint_S \left[n\frac{\partial \nabla^2 n}{\partial \nu} - \nabla^2 n \frac{\partial n}{\partial \nu}\right] da \tag{B.11}$$

The right hand side of this equation is a surface term and assuming the periodic boundary conditions this term is zero (since eventually we need to integrate the free energy over the whole space). Thus we get

$$\int_V n\nabla^4 n d\mathbf{r} = \int_V \left(\nabla^2 n\right)^2 d\mathbf{r}. \tag{B.12}$$

We can now calculate the integral of the term $n\nabla^4 n$ by integrating $(\nabla^2 n)(\nabla^2 n)^*$. We use Eq. B.8 to calculate this term

$$\begin{aligned} \int n\nabla^4 n d\mathbf{r} = \int \Big\{ \sum_j \left[(\mathcal{G}_j - 1)\eta_j e^{i\mathbf{q}_j \cdot \mathbf{r}} + (\mathcal{G}_j^* - 1)\eta_j^* e^{-i\mathbf{q}_j \cdot \mathbf{r}}\right] \\ \times \sum_k \left[(\mathcal{G}_k - 1)\eta_k e^{i\mathbf{q}_k \cdot \mathbf{r}} + (\mathcal{G}_k^* - 1)\eta_k^* e^{-i\mathbf{q}_k \cdot \mathbf{r}}\right]\Big\} d\mathbf{r}, \end{aligned} \tag{B.13}$$

From multiplication of the two terms in the integrand above, a few terms appear that contain $\exp(i\mathbf{q}_i \cdot \mathbf{r})$ and therefore they vanish when integrated over the unit cell. Simplifying this expression, we obtain

$$\begin{aligned} \int n\nabla^4 n d\mathbf{r} &= 2\sum_j \left[(\mathcal{G}_j - 1)(\mathcal{G}_j^* - 1)|\eta_j|^2\right] \\ &= 2\sum_j \left(|\mathcal{G}_j|^2 - (\mathcal{G}_j + \mathcal{G}_j^*) + 1\right)|\eta_j|^2. \end{aligned} \tag{B.14}$$

To complete the amplitude expansion of the *PFC* part of the free energy, we need to calculate the integral of n^2 over the unit cell. Using the amplitude expansion of n we obtain

[2] Green's second identity states that if twice continuously differentiable scalar functions ϕ and ψ, then

$$\int_V \left(\phi\nabla^2\psi - \psi\nabla^2\phi\right) d\mathbf{r} = \oint_S \left[\phi\frac{\partial\psi}{\partial\nu} - \psi\frac{\partial\phi}{\partial\nu}\right] da$$

where S is a closed two dimensional surface bounding V, with area element da and outward unit normal vector ν at da. The derivative $\partial/\partial\nu$ is the normal derivative at the surface [33].

$$\begin{aligned}\int n^2 d\mathbf{r} &= \int \Big[n_0 + \sum_j \left(\eta_j e^{i\mathbf{q}_j\cdot\mathbf{r}} + \eta_j^* e^{-i\mathbf{q}_j\cdot\mathbf{r}}\right)\Big]\Big[n_0 + \sum_k \left(\eta_k e^{i\mathbf{q}_k\cdot\mathbf{r}} + \eta_k^* e^{-i\mathbf{q}_k\cdot\mathbf{r}}\right)\Big] \\ &= n_0^2 + 2\sum_j |\eta_j|^2,\end{aligned} \tag{B.15}$$

in which we have set the terms containing integrals of $\exp(i\mathbf{q}_i\cdot\mathbf{r})$ equal to zero. Finally, we can calculate $f_{pfc}^{(1)}$ by adding the terms calculated above to obtain

$$\begin{aligned}n\Big(\Delta B + B_s(1+\nabla^2)^2\Big)\frac{n^2}{2} &= \frac{1}{2}(\Delta B + B_s)n^2 + B_s\Big(n\nabla^2 n + \frac{1}{2}n\nabla^4 n\Big) \\ &= (\Delta B + B_s)(\frac{1}{2}n_0^2 + \sum_j |\eta_j|^2) \\ &+ B_s\Big[\sum_j |\eta_j|^2\Big(\mathcal{G}_j^* + \mathcal{G}_j - 2 + |\mathcal{G}_j|^2 - \mathcal{G}_j - \mathcal{G}_j^* + 1\Big)\Big] \\ &= -\sum_j |\eta_j|^2 + \sum_j |\mathcal{G}_j\eta_j|^2.\end{aligned} \tag{B.16}$$

Let us consider the last two terms of f_{pfc}

$$f_{pfc}^{(2)} = -t\frac{n^3}{3} + v\frac{n^4}{4}. \tag{B.17}$$

We need to substitute the hexagonal reciprocal lattice vectors, $\mathbf{q}_1 = -\frac{\sqrt{3}}{2}\mathbf{i} - \frac{1}{2}\mathbf{j}$ and $\mathbf{q}_2 = \mathbf{j}$, into the density expansion, Eq. 8.2 and integrate $f_{pfc}^{(2)}$ over the unit cell. Evaluating the integral we obtain

$$\begin{aligned}\int(-t\frac{n^3}{3} + v\frac{n^4}{4})d\mathbf{r} = -t&\left(\frac{1}{3}n_0^3 + 2n_0\sum_j |\eta_j|^2 + 2\left(\prod_j \eta_j + \prod_j \eta_j^*\right)\right) \\ &+ v\left(\frac{1}{4}n_0^4 + 3n_0^2\sum_j |\eta_j|^2 + \frac{3}{2}\sum_j |\eta_j|^4 + 6\left(|\eta_1|^2|\eta_3|^2 + |\eta_1|^2|\eta_2|^2 + |\eta_2|^2|\eta_3|^2\right)\right) \\ &+ v\left(6n_0\left(\prod_j \eta_j + \prod_j \eta_j^*\right)\right).\end{aligned} \tag{B.18}$$

B.1.2 The magneto-elastic part of the free energy - F_{m-e}

The magneto-elastic free energy density term is

$$f_{m-e} = (\frac{\alpha}{2}\mathbf{m}\cdot\nabla n)^2 \tag{B.19}$$

substituting the density expansion into the term $\mathbf{m}\cdot\nabla n$ and using the Einstein convention yields

$$\begin{aligned}
\mathbf{m}\cdot\nabla n &= m_i(\nabla n)_i \\
&= m_i(\partial_i n) = m_i\partial_i(n_0 + \eta_j e^{i\mathbf{q}_j\cdot\mathbf{r}} + C.C.) \\
&= m_i\Big[(\partial_i\eta_j)e^{i\mathbf{q}_j\cdot\mathbf{r}} + iq_{jk}\eta_j(\partial_i r_k)e^{iq_{jk}r_k}\Big] + C.C. \\
&= m_i\Big[(\partial_i\eta_j) + iq_{jk}\eta_j\delta_{ik}\Big]e^{i\mathbf{q}_j\cdot\mathbf{r}} + C.C. \\
&= m_i\Big[(\nabla\eta_j)_i + i\eta_j q_{ji}\Big]e^{i\mathbf{q}_j\cdot\mathbf{r}} + C.C. \\
&= \Big[\mathbf{m}\cdot(\nabla + i\mathbf{q}_j)\eta_j\Big]e^{i\mathbf{q}_j\cdot\mathbf{r}} + \Big[\mathbf{m}\cdot(\nabla - i\mathbf{q}_j)\eta_j^*\Big]e^{-i\mathbf{q}_j\cdot\mathbf{r}}.
\end{aligned} \tag{B.20}$$

To calculate the integral of f_{m-e} we multiply $\mathbf{m}\cdot\nabla n$ by its complex conjugate and integrate

$$\begin{aligned}
\int(\mathbf{m}\cdot\nabla n)^2 d\mathbf{r} = \int\Big\{&\Big[\mathbf{m}\cdot(\nabla + i\mathbf{q}_j)\eta_j e^{i\mathbf{q}_j\cdot\mathbf{r}} + \mathbf{m}\cdot(\nabla - i\mathbf{q}_j)\eta_j^* e^{-i\mathbf{q}_j\cdot\mathbf{r}}\Big] \\
&\times\Big[\mathbf{m}\cdot(\nabla - i\mathbf{q}_k)\eta_k^* e^{i\mathbf{q}_k\cdot\mathbf{r}} + \mathbf{m}\cdot(\nabla + i\mathbf{q}_k)\eta_k e^{-i\mathbf{q}_k\cdot\mathbf{r}}\Big]\Big\}d\mathbf{r}
\end{aligned} \tag{B.21}$$

Multiplying the terms and setting the terms that contain $\exp[i(\mathbf{q}_j - \mathbf{q}_k)\cdot\mathbf{r}]$ equal to zero for $j \neq k$, we obtain

$$\int(\mathbf{m}\cdot\nabla n)^2 d\mathbf{r} = 2\int\Big\{\Big(\mathbf{m}\cdot\nabla\eta_j + i\mathbf{m}\cdot\mathbf{q}_j\eta_j\Big)\Big(\mathbf{m}\cdot\nabla\eta_j^* - i\mathbf{m}\cdot\mathbf{q}_j\eta_j^*\Big)\Big\}d\mathbf{r} \tag{B.22}$$

Using the notation $\mathcal{A}_j \equiv \mathbf{m}\cdot(\nabla + i\mathbf{q}_j)$, for the amplitude expansion of the magneto-elastic term we obtain

$$\frac{\alpha}{2}\int(\mathbf{m}\cdot\nabla n)^2 d\mathbf{r} = \alpha\int\sum_j|\mathcal{A}_j\eta_j|^2 d\mathbf{r}. \tag{B.23}$$

B.1.3 The Landau-Ginzburg magnetic term - $F_{\mathbf{m}}$

We need to insert the amplitude expansion of density into

$$F_{\mathbf{m}} = \int\Big[\frac{W_0^2}{2}|\nabla\mathbf{m}|^2 + (r_c - \beta n^2)\frac{|\mathbf{m}|^2}{2} + \gamma\frac{|\mathbf{m}|^4}{4}\Big]. \tag{B.24}$$

The only density term appears in this free energy is n^2. We have already calculated the amplitude expansion of this term and obtained Eq. B.15. Inserting it into this equation we obtain

$$\int\Big[\frac{W_0^2}{2}|\nabla\mathbf{m}|^2 + \left[r_c - \beta\left(n_0^2 + 2\sum_j|\eta_j|^2\right)\right]\frac{|\mathbf{m}|^2}{2} + \gamma\frac{|\mathbf{m}|^4}{4}\Big]d\mathbf{r}. \tag{B.25}$$

Finally adding Eqs.B.16, B.18, B.23 and B.25, we obtain Eq. 8.3 for the free energy in terms of the amplitudes of the density.

B.2 Elastic deformations

To incorporate the elastic deformations into the free energy we substitute

$$\eta_j = \phi \exp(i\mathbf{q}_j \cdot \mathbf{u}), \tag{B.26}$$

into Eq. 8.3. The field $\mathbf{u}(\mathbf{r}) = (u_x(\mathbf{r}), u_y(\mathbf{r}))$ denotes the displacement of the atoms from their equilibrium position.

The calculations is done by inserting the reciprocal lattice vectors, $\mathbf{q}_1 = -\frac{\sqrt{3}}{2}\mathbf{i} - \frac{1}{2}\mathbf{j}$ and $\mathbf{q}_2 = \mathbf{j}$, into Eq. B.26 to obtain η_1 and η_2

$$\eta_1 = \phi e^{-\frac{\sqrt{(3)}}{2} i u_x(\mathbf{r}) - \frac{1}{2} i u_y(\mathbf{r})}, \tag{B.27}$$

$$\eta_2 = \phi e^{i u_y(\mathbf{r})} \tag{B.28}$$

The term $|\eta_j|^2$ is obtained by multiplying η_j by its complex conjugate which yields ϕ^2. The term $|\mathcal{G}_j \eta_j|^2$ contains the Laplacian operator and the terms such as $\partial_j^2 u_k$ and $(\partial_j u_k)^2$ appear in the expressions. As an example

$$\mathcal{G}_2 = \phi e^{i u_y(\mathbf{r})} \Big(i(\partial_x^2 u_y(\mathbf{r})) - (\partial_x u_y(\mathbf{r}))^2 + i(\partial_y^2 u_y(\mathbf{r})) - (\partial_y u_y(\mathbf{r}))^2 - 2(\partial_y u_y(\mathbf{r})) \Big). \tag{B.29}$$

Again we need to multiply $\mathcal{G}_j$ by its complex conjugate and add for $j = 1, 2$ to obtain $\sum_j |\mathcal{G}_j \eta_j|^2$. The process is similar for the rest of the terms in Eq. 8.3. It gives a complicated expression in terms of ϕ, $\partial_j^2 u_k$ and $(\partial_j u_k)^2$. To simplify the expression we notice that the derivatives can be written in terms of the strain tensor elements defined as

$$U_{xx} = u_{xx} + \frac{1}{2}(u_{xx}^2 + u_{yx}^2) \tag{B.30}$$

$$U_{yy} = u_{yy} + \frac{1}{2}(u_{yy}^2 + u_{xy}^2) \tag{B.31}$$

$$U_{xy} = \frac{1}{2}(u_{xy} + u_{yx} + u_{xx}u_{xy} + u_{yx}u_{yy}) \tag{B.32}$$

where $u_{ij} \equiv \partial_j u_i$. For example $u_{xx} = \partial_x u_x$. Replacing the relevant derivatives of u_i with the strain tensor elements U_{xx}, U_{yy} and U_{xy}, we can show the free energy incorporating the elastic deformations is given by

$$
\begin{aligned}
F_{\phi,U_{ij}} = \int \Bigg\{ & (\Delta B + B_s)\left(\frac{1}{2}n_0^2 + 3\phi^2\right) \\
& + B_s\left[-3\phi^2 + \phi^2\left(\frac{9}{2}\left(U_{xx}^2 + U_{yy}^2\right) + 3U_{xx}U_{yy} + 6U_{xy}^2\right)\right] \\
& - t\left(\frac{1}{3}n_0^2 + 6n_0\phi^2 + 4\phi^3\right) \\
& + v\left(\frac{1}{4}n_0^4 + 9n_0^2\phi^2 + 12n_0\phi^3 + \frac{45}{2}\phi^4\right) \\
& - 3\alpha\phi^2\left(\frac{|\mathbf{m}|^2}{2} + U_{xx}|m_x|^2 + U_{yy}|m_y|^2 + 2U_{xy}m_x m_y\right) \\
& + \left(\frac{W_0^2}{2}|\nabla\mathbf{m}|^2 + \left[r_c - \beta\left(n_0^2 + 6\phi^2\right)\right]\frac{|\mathbf{m}|^2}{2} + \gamma\frac{|\mathbf{m}|^4}{4}\right)\Bigg\}.
\end{aligned}
\tag{B.33}
$$

which is Eq. 8.4.

Appendix C

Numerical Methods

The intent of this chapter is to briefly describe the numerical schemes used in the Magnetic PFC simulations to solve the partial differential equations discussed in Section 7.2 and derived in Appendix A. The results obtained from these simulations are presented in Chapter 9. We used Finite Difference and Fast Fourier Transform methods to solve the dynamical equations of motion and the Poisson Equation.

C.1 Finite-difference method

We need to solve three partial differential equations, given by Eqs. 7.6-7.8, *i.e.*,

$$\begin{aligned}\frac{\partial n(\mathbf{r},t)}{\partial t} = &\left(\Delta B + B_s\left(1+\nabla^2\right)^2\right)n - tn^2 + vn^3 - \beta n|\mathbf{m}|^2 \\ &- \alpha\left[(\mathbf{m}\cdot\nabla n)(\nabla\cdot\mathbf{m}) + \mathbf{m}\cdot\nabla(\mathbf{m}\cdot\nabla n)\right],\end{aligned} \tag{C.1}$$

where n is the density field and

$$\frac{\partial m_x(\mathbf{r},t)}{\partial t} = W_0^2\nabla^2 m_x - \left(r_c - \beta n^2\right)m_x - \gamma m_x|\mathbf{m}|^2 - \alpha(\mathbf{m}\cdot\nabla n)\,\partial_x n + B_x(\mathbf{r},t), \tag{C.2}$$

$$\frac{\partial m_y(\mathbf{r},t)}{\partial t} = W_0^2\nabla^2 m_y - \left(r_c - \beta n^2\right)m_y - \gamma m_y|\mathbf{m}|^2 - \alpha(\mathbf{m}\cdot\nabla n)\,\partial_y n + B_y(\mathbf{r},t) \tag{C.3}$$

for $\mathbf{m} = (m_x, m_y)$, the magnetization fields. In Eqs.C.1-C.3, ΔB, B_s, t, v, β, α, r_c, and γ are constant real-valued parameters which can be expressed in terms of a few measurable physical quantities such as Curie temperature and magnetic susceptibility. The values of these parameters and how to calculate them are explained in Chapter 7.

The magnetic field, $\mathbf{B} = (B_x, B_y)$, is expressed through a vector potential $\mathbf{A}$ as

$$\mathbf{B} = \nabla\times\mathbf{A}, \tag{C.4}$$

and $\mathbf{A}$ can be calculated from the Poisson equation below

$$\nabla^2\mathbf{A} = -\mu_o\nabla\times\mathbf{m}. \tag{C.5}$$

where μ_0 is the permeability and has a constant value (Chapter 7). It should be mentioned that our model is a two dimensional model and we assume that $\mathbf{m} = (m_x, m_y)$. Therefore if we insert $\mathbf{m} = (m_x, m_y)$ into the equation C.5, we see that the magnetization current density, $\mathbf{J}_M \equiv \nabla \times \mathbf{m}$, will have only one non-zero component in the z direction. Therefore the vector potential $\mathbf{A}$ also have only one non-zero component, i.e., $\mathbf{A} = (0, 0, A_z)$ and technically we should only solve the Poisson equation in z direction. The goal of our numerical code is to track the time evolution of n, m_x and m_y.

The three partial differential equations for n, m_x and m_y given by Eqs.C.1-C.3 are *initial value problems*. In an initial value problem [53], the information on the function is given at some initial time t_0 for all $\mathbf{r}$ and the equation describes how it evolves with time. Starting with an initial value for $n(\mathbf{r})$ and $\mathbf{m}(\mathbf{r})$ at t_0, we solve Eqs.C.4 and C.5 and calculate $\mathbf{B}$. Then we insert the value of $\mathbf{B}$ back into Eqs.C.1-C.3 to calculate $n(\mathbf{r})$ and $\mathbf{m}(\mathbf{r})$ at the next time-step.

A *Finite difference method* is used to estimate the vector differential operators and to solve the initial value problems. In this method a grid is generated where the functions n, m_x and m_y are approximated only at the grid points, i.e., $n_{i,j}$, $m_x(i, j)$ and $m_y(i, j)$. An example of a two dimensional grid is represented in Fig. C.1. By discretizing the derivatives on the grid points, we can reduce them to algebraic equations. We use *periodic boundary conditions* to solve the equations, meaning that we assume $n_{L_x+1,j} = n_{1,j}$ and $n_{i,L_y+1} = n_{i,1}$, in which L_x and L_y are the dimensions of the grid in the x and y directions, respectively. The same realetions are applied for m_x and m_y.

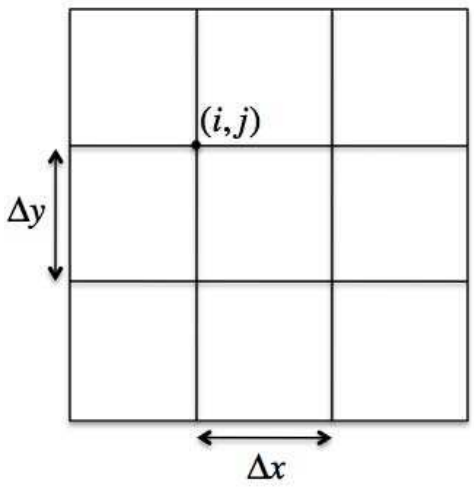

Figure C.1: To discretize the partial differential equations we generate a grid and the value of the function is approximated only on the grid points. Δx and Δy are the grid spacings in x and y directions, respectively.

C.1.1 Spatial derivatives

Consider the Taylor expansion of a function u in one dimension

$$u(x_0 + \Delta x) = u(x_0) + \left.\frac{du}{dx}\right|_{x_0} \Delta x + O(\Delta x^2). \tag{C.6}$$

Rephrasing this equation for $u' = (du/dx)|_{x_0}$ gives an approximate expression to calculate the derivative

$$u' \approx (u(x_0 + \Delta x) - u(x_0))/\Delta x. \tag{C.7}$$

It is clear that this approximation is correct up to the first order in Δx. This is called the *forward* difference formula [53]. We can also calculate the derivative using the backward differencing scheme [53], i.e., $u' = (u(x_0) - u(x_0 - \Delta x))/\Delta x$ which has a similar order of accuracy. It is possible to increase the order of accuracy either by including more terms in the Taylor expansion or by using the *central* difference formula [53]

$$u'(x_0) \approx (u(x_0 + \Delta x) - u(x_0 - \Delta x))/2\Delta x. \tag{C.8}$$

It can easily be shown that this scheme is accurate up to the second order in Δx. By Taylor expanding $u(x_0 + \Delta x)$ and $u(x_0 - \Delta x)$

$$u(x_0 + \Delta x) = u(x_0) + u'(x_0)\Delta x + u''(x_0)(\Delta x)^2 + O(\Delta x)^3 \tag{C.9}$$
$$u(x_0 - \Delta x) = u(x_0) - u'(x_0)\Delta x + u''(x_0)(\Delta x)^2 - O(\Delta x)^3, \tag{C.10}$$

where $u''(x_0) = \left.\frac{d^2u}{dx^2}\right|_{x_0}$. Subtracting Eqs.C.9 from C.10 gives

$$u(x_0 + \Delta x) - u(x_0 - \Delta x) = 2u'(x_0)\Delta x + O(\Delta x)^3, \tag{C.11}$$

which gives rise to the central difference scheme, Eq. C.8. It is clear from Eq. C.11 that the derivative $u'(x_0)$ calculated from this scheme is correct to $(\Delta x)^2$ order.

Based on the above discussions, the simplest finite difference scheme to calculate the derivative of a function u is therefore given by

$$\partial_x u(i, j) = (u_{i+1,j} - u_{i,j})/\Delta x \tag{C.12}$$
$$\partial_y u(i, i) = (u_{i,j+1} - u_{i,j})/\Delta y. \tag{C.13}$$

These are the main differentiating schemes we applied to calculate the first order derivatives.

To calculate the Laplacian operator, we need to calculate the second derivatives. By Taylor expanding $u(x_0 + h, y_0)$ and $u(x_0 - h, y_0)$ we get

$$u(x_0 + h, y_0) = u(x_0, y_0) + h\partial_x u(x, y)|_{(x_0,y_0)} + h^2\partial_x^2 u(x, y)|_{(x_0,y_0)} + O(h^3) \tag{C.14}$$
$$u(x_0 - h, y_0) = u(x_0, y_0) - h\partial_x u(x, y)|_{(x_0,y_0)} + h^2\partial_x^2 u(x, y)|_{(x_0,y_0)} - O(h^3), \tag{C.15}$$

where we assumed $\Delta x = \Delta y = h$. Adding these two equations gives

$$u(x_0 + h, y_0) + u(x_0 - h, y_0) = 2u(x_0, y_0) + 2h^2\partial_x^2 u(x, y)|_{(x_0,y_0)} + O(h^4). \tag{C.16}$$

From this equation

$$\partial_x^2 u(x,y)|_{(x_0,y_0)} = (u(x_0+h,y_0) + u(x_0-h,y_0) - 2u(x_0,y_0))/h^2 + O(h^2). \quad \text{(C.17)}$$

In a similar manner we can calculate $\partial_y^2 u(x,y)|_{(x_0,y_0)}$. Therefore

$$\nabla^2 u(x_0,y_0) \approx \frac{u(x_0-h,y_0) + u(x_0+h,y_0) + u(x_0,y_0+h) + u(x_0,y_0-h) - 4u(x_0,y_0)}{h^2} \quad \text{(C.18)}$$

which as we saw, is accurate to the second order in h. This scheme is called the *five-point stencil* for Laplacian, with five points contributing to calculate the Laplacian as shown in Fig. C.2.

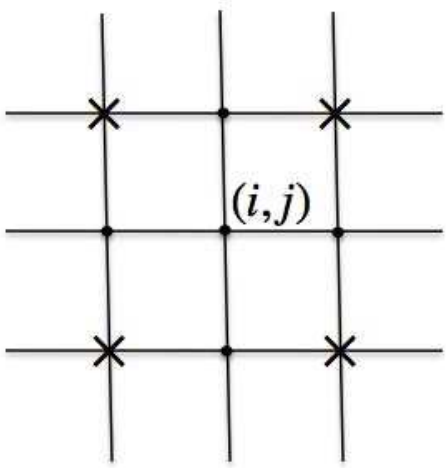

Figure C.2: Five-point and nine-point stencils for finite difference Laplacian calculation. The dots show the five points used to calculate the Laplacian in the five-point scheme. The stars show the additional four points used together with the dots to calculate the Laplacian in the nine-point scheme.

Another possible approximation to calculate the Laplacian operator is the *nine-point* differencing scheme [5]. In this scheme four additional points, i.e., $u_{i\pm1,j\pm1}$ are used to calculate the Laplacian. In the general nine-point scheme, the Laplacian is calculated using [5]

$$\nabla^2 u_{i,j} \approx \frac{1}{6h^2}(4S_1 + S_2 - 20u_{i,j}) \quad \text{(C.19)}$$

with

$$S_1 = u_{i+1,j} + u_{i-1,j} + u_{i,j+1} + u_{i,j-1} \quad \text{(C.20)}$$

$$S_2 = u_{i+1,j+1} + u_{i-1,j+1} + u_{i+1,j-1} + u_{i-1,j-1}. \quad \text{(C.21)}$$

From the point of view of the accuracy, this scheme is not better than the five-point scheme since it is also correct to $O(h^2)$. However the additional four terms lead to a very nice form for the leading terms of the error [5]

$$-\frac{1}{12}h^2\nabla^4 u_{i,j} + h^4\mathcal{F}(\nabla^2 u_{i,j}, \nabla^6 u_{i,j}) + \mathcal{O}(h^6). \tag{C.22}$$

Both of these terms become zero for the Laplace equation and we get an accuracy of $\mathcal{O}(h^6)$. The matrix representation for the nine-point stencil we applied is [52]

$$M = \begin{bmatrix} \frac{1}{4} & \frac{1}{2} & \frac{1}{4} \\ \frac{1}{2} & -3 & \frac{1}{2} \\ \frac{1}{4} & \frac{1}{2} & \frac{1}{4} \end{bmatrix}. \tag{C.23}$$

In the next section the numerical method to calculate the initial value problems is explained.

C.1.2 The initial value problem

To solve an initial value problem, we discretize the time derivative on the left hand side of Eqs.C.1-C.3

$$\left.\frac{\partial u}{\partial t}\right|_{j,n} = \frac{u_j^{n+1} - u_j^n}{\Delta t} + \mathcal{O}(\Delta t). \tag{C.24}$$

Rephrasing this equation we can calculate u_j^{n+1}. This is called *forward Euler* differencing. It is accurate to the first order in Δt and we can calculate the value of the function at time-step $n+1$ in terms of the value of function only at time-step n. It is an *explicit* method, which means that u_j^{n+1} can be calculated explicitly from the quantities that are already know, i.e., one should solve an equation $u_j^{n+1} = \mathcal{F}(u^n)$ to find u^{n+1}. An *implicit* method however finds the solution by solving an equation which involves quantities both in the current time-step and next time-step(s), i.e., one should solve an equation simular to $\mathcal{F}(u^n, u^{n+1}) = 0$ to find u^{n+1}. While the explicit method might not be *stable* to solve certain differential equations, an implicit method is stable for them [53].

To solve the initial value problems, Eqs.C.1-C.3, we discretize the right hand side of the equations using the finite difference methods described in the previous section and use the *forward Euler* differencing method to calculate $n_{i,j}^{n+1}$, $m_x^{n+1}(i, j)$ and $m_y^{n+1}(i, j)$ in terms of their known values at time-step n. To calculate $\mathbf{B}$ at time-step n, we calculate $\mathbf{A}$, knowing the magnetization $\mathbf{m}$ at time-step n.

To investigate whether the methods we used are stable or not, we use the *Von Neumann stability analysis* [53] explained in the next section.

C.1.3 Von Neumann stability analysis

The stability of a numerical method is related to its accuracy. A finite difference scheme is stable if the errors made at each time-step do not grow as the computations are continued. The Von Neumann method (also know as Fourier stability analysis) is based on the decomposition of the errors into Fourier series. Considering the differential equation

$$\frac{\partial u}{\partial t} = -v\frac{\partial u}{\partial x}, \tag{C.25}$$

we discretize it using the Euler forward time centred space scheme

$$\frac{u_j^{n+1} - u_j^n}{\Delta t} = -v\frac{u_{j+1}^n - u_{j-1}^n}{2\Delta x} \tag{C.26}$$

which can be rearranged to give a formula for u_j^{n+1}.

We define the round-off error at each time-step as

$$\epsilon_j^n = N_j^n - u_j^n \tag{C.27}$$

where u_j^n is the solution of the discretized equation and N_j^n is the numerical solution which is free from any round-off error. Rephrasing for u_j^n and inserting it into the discretized equation C.26, we see that the error must also satisfy the equation, since the exact solution N_j^n must satisfy the equation exactly.

It is helpful to expand the error in a finite Fourier series. Considering a single Fourier mode of wave-number k

$$\epsilon_j^n = \xi e^{ikj\Delta x}, \tag{C.28}$$

where $\xi(k)$ is a complex number that depends on k and includes the time-dependence of the error. To see whether the algorithm is stable or not, we need to consider the *amplification factor* defined to be

$$G \equiv \epsilon_j^{n+1}/\epsilon_j^n. \tag{C.29}$$

The necessary and sufficient condition for the error to remain bounded is that $|G| \leq 1$ [61]. Calculating the amplification factor using Eq. C.28 we get

$$G = \xi(k). \tag{C.30}$$

To calculate $\xi(k)$ we substitute Eq. C.28 into Eq. C.26. Dividing it by ξ^n we get

$$\xi(k) = 1 - i\frac{v\Delta t}{\Delta x}\sin(k\Delta x) \tag{C.31}$$

It is clear from this relation that the Euler forward time centred space scheme is unconditionally unstable, since $|G| > 1$ for all k in this case. It is possible to make this scheme stable by replacing the term u_j^n by its average in space, i.e., $u_j^n \rightarrow (u_{j+1}^n + u_{j-1}^n)/2$. This scheme was introduced by Lax [53]. Performing the Von Neumann stability analysis for Lax's scheme, it can easily be shown that

$$\xi = \cos(k\Delta x) - i\frac{v\Delta t}{\Delta x}\sin(k\Delta x) \tag{C.32}$$

The stability condition leads to the condition

$$\frac{|v|\Delta t}{\Delta x} \leq 1 \tag{C.33}$$

which is called Courant-Friedrichs-Lewy stability condition [53]. This means that in order for the Lax algorithm to be stable, Δx and Δt need to be chosen to satisfy this condition.

We now consider the stability condition for the diffusive equations we encounter in our problem. The diffusion equation

$$\frac{\partial u}{\partial t} = D\frac{\partial^2 u}{\partial x^2} \tag{C.34}$$

can be discretize in the obvious way of forward time centred space scheme

$$\frac{u^{n+1}{}_j - u_j^n}{\Delta t} = D\frac{u_{j+1}^n - 2u_j^n + u_{j-1}^n}{\Delta x^2}. \tag{C.35}$$

A quick stability calculation shows that the amplification factor for this equation is

$$\xi = 1 - \frac{4D\Delta t}{(\Delta x)^2}\sin^2\Big(\frac{k\Delta x}{2}\Big). \tag{C.36}$$

The stability requirement $|\xi| \leq 1$ leads to the condition

$$\frac{2D\Delta t}{(\Delta x)^2} \leq 1. \tag{C.37}$$

This means that the maximum allowed time-step is up to a numerical factor equal to the diffusion time across a grid cell of width Δx.

C.2 Fourier transform method

A physical process can be described either in the *space domain*, $f(x)$, or in the *frequency domain*, $\hat{f}(\xi)$. It is useful to think of $f(x)$ and $\hat{f}(\xi)$ to be two different representations of the same function. The transformation between these two representations is possible by means of the *Fourier transform* equations.

$$\hat{f}(\xi) = \frac{1}{\sqrt{2\pi}}\int_{-\infty}^{-\infty} f(x)e^{-2\pi i x\xi}dx \tag{C.38}$$

$$f(x) = \frac{1}{\sqrt{2\pi}}\int_{-\infty}^{-\infty} \hat{f}(\xi)e^{2\pi i\xi x}d\xi \tag{C.39}$$

where x represents the independent spatial variable and the transform variable ξ represents frequency. Similarly, one can transform an equation from one representation to the other. Sometimes it is much easier to solve an equation in one representation in comparison to another.

In the magnetic-PFC problem, to calculate $\mathbf{B}$, the Poisson equation C.5 should be solved to calculate the vector potential $\mathbf{A}$. In this section we show that it is much easier to solve the Poisson equation in the Fourier space. As explained before, since we assume $\mathbf{m} = (m_x, m_y)$ we only need to solve the Poisson equation for A_z. Multiplying both sides of the Poisson equation by $\exp(-2\pi i\mathbf{x}\cdot\xi)$ and integrating over $d\mathbf{x}$ we get

$$\int_{-\infty}^{-\infty} \nabla^2 A_z(\mathbf{x})e^{-2\pi i\mathbf{x}\cdot\xi}d\mathbf{x} = -\mu_0\int_{-\infty}^{-\infty} \mathbf{J}_M(\mathbf{x})e^{-2\pi i\mathbf{x}\cdot\xi}d\mathbf{x}, \tag{C.40}$$

where $\mathbf{J}_M(\mathbf{x}) \equiv (\nabla \times \mathbf{m})_z$ is called the magnetization current density. The right hand side of this equation is simply the Fourier transform of $\mathbf{J}_M$ which will be denoted by $\hat{\mathbf{J}}_M(\xi)$. To calculate the left hand side of integral, we use the notation ∂_j with $j = 1, 2, 3$ to show ∂_x, ∂_y and ∂_z, respectively. We also use the Einstein summation convention[1]. In this notation the left hand side of Eq. C.40 can be written as

$$LHS = \int_{-\infty}^{-\infty} \partial_j^2 A_z(\mathbf{x}) e^{-2\pi i x_j \xi_j} d\mathbf{x} \tag{C.41}$$

Integrating by parts we get

$$LHS = \partial_j^2 (A_z e^{-2\pi i x_j \xi_j}) - \int_{-\infty}^{-\infty} \partial_j^2 (e^{-2\pi i x_j \xi_j}) A_z d\mathbf{x} \tag{C.42}$$

The first term is a surface term. Since we assume periodic boundary condition for the density field, the magnetic field and the vector potential also have periodic structures and thus the surface term becomes zero.

$$LHS = (2\pi\xi)^2 \int_{-\infty}^{-\infty} A_z e^{-2\pi i \mathbf{x}\cdot\xi} d\mathbf{x} = (2\pi\xi)^2 \hat{A}_z(\xi). \tag{C.43}$$

Therefore the Poisson equation in the Fourier space is written as

$$(2\pi\xi)^2 \hat{A}_z(\xi) = -\mu_0 \hat{\mathbf{J}}_M(\xi). \tag{C.44}$$

This is an algebraic equation. To find $\hat{A}_z(\xi)$, all we need is to divide $\hat{\mathbf{J}}_M(\xi)$ by $(2\pi\xi)^2$. Clearly, comparing to solving the Poisson's equation in real space, it is significantly simpler to transform it to the Fourier space, solve this algebraic equation and then transform $\hat{A}_z(\xi)$ back to the real space by doing an inverse Fourier transform, Eq. C.39 to find $A_z(\mathbf{x})$.

C.2.1 Fast Fourier transform

Since we have discretize our equations, we need to use the *discrete Fourier transform* (DFT) to transform the equations to the Fourier space and back. It can be shown [53] that Fourier transform of a series of discrete data x_n could be calculated by

$$X_k = \sum_{n=0}^{N-1} x_n e^{-i2\pi kn/N} \tag{C.45}$$

$$x_n = \frac{1}{N} \sum_{n=0}^{N-1} X_k e^{i2\pi kn/N} \tag{C.46}$$

These summations appear to be $O(N^2)$ processes; however, in fact they can be computed with $O(N \log_2(N))$ operations with an algorithm called the *fast Fourier transform* method or FFT. A clear description of the method was given by Danielson and Lanczos. They showed

[1] According to this convention, when an index variable appears twice in one term it implies a summation of that term over all the possible values of the index.

that a discrete Fourier transform of length N can be rewritten as a sum of two discrete Fourier transforms, each of length $N/2$:, i.e., the even-indexed points of the data and the odd-indexed points.

To see how the order of computations is reduced using this method, we write $M \equiv N/2$ and denote the DFT of the even-numbered terms, x_{2m}, by E_j and the DFT of the odd-numbered terms, x_{2m+1} by O_j ($m = 0, .., M-1$ and $j = 0, .., M-1$), i.e.,

$$\begin{aligned} X_k &= \sum_{m=0}^{N/2-1} x_{2m} e^{-2\pi i(2m)k/N} + \sum_{m=0}^{N/2-1} x_{2m+1} e^{-2\pi i(2m+1)k/N} \\ &= \sum_{m=0}^{M-1} x_{2m} e^{-2\pi imk/M} + e^{-2\pi ik/N} \sum_{m=0}^{M-1} x_{2m+1} e^{-2\pi imk/M.} \end{aligned} \tag{C.47}$$

Using the fact that $E_{k+M} = E_k$ and $O_{k-M} = O_{-k}$, we can evaluate X_k

$$X_k = \begin{cases} E_k + e^{-2\pi ik/N} O_k & \text{if } k < M \\ E_{k-M} - e^{-2\pi i(k-M)/N} O_{k-M} & \text{if } k \geq M. \end{cases} \tag{C.48}$$

These two DFTs have two advantages: 1) they only have M sample points in the DFT and 2) they only need to be evaluated for M values of k. Dividing the initial DFT to odd-indexed and even-indexed terms, enabled us to use the periodic properties of the DFT, i.e., the terms for $N/2 \leq k < N$ of length $N/2$ are identical to the terms for $0 \leq k < N/2$. It is important to note that the Danielson-Lanczos method [53] assumes that the number of data points,N, is a power of two.

In our code, we used the Numerical Recipes in Fortran 90 code [53] which uses the Danielson-Lanczos method, to transform the Poisson equation to the Fourier space and back to the real space. The algorithms described in this chapter were the main methods we used to solve the differential equations C.1-C.3 and Eqs.C.4 and C.5.

Curriculum Vitae

Name: Niloufar Faghihi

Education Degrees:

2008 - 2012 Ph.D.
University of Western Ontario
London, ON

2005 - 2007 M.Sc.
Sharif University of Technology
Tehran, Iran

Related Work Experience:

Teaching Assistant
The University of Western Ontario
2008 - 2012

Sharif University of Technology
2006-2007